Computational Discovery of Metal-Organic Frameworks for Carbon Capture and Natural Gas Storage

by

Hyun Seung Koh

A dissertation submitted in partial fulfillment
of the requirements for the degree of
Doctor of Philosophy
(Mechanical Engineering)
in the University of Michigan
2014

Doctoral Committee:

Assistant Professor Donald J. Siegel, Chair
Professor André L. Boehman
Professor Wei Lu
Professor Adam J. Matzger

Acknowledgments

First of all, I would like to thank God for granting me the perseverance to successfully complete this thesis.

My greatest debt is to my advisor, Prof. Don Siegel. His insight and enthusiasm were a guiding force in my studies. I am especially grateful for his patience and encouragement during the challenging phases of this research associated with generating new interatomic potentials.

For serving on my Ph.D. committee, I thank Professors Adam Matzger, Andre L. Boehman, and Wei Lu.

I thank my collaborator and teammate in this research, Dr. Malay Kumar Rana. The support of the other group members of the Siegel group (Maxwell Radin, Yang Ming, Sheng Yang, Jeffrey Smith, Gulin Vardar, Seoungho Yu, Mallory Fuhst, Nitin Kumar, Janakiraman Balachandran, Junichi Naruse, Haesun Park, Kyle Nagy, and Jinhyung Hwnag) is also greatly appreciated.

I thank members of the Campus Town Church for their prayer and friendship.

Finally, special thanks are due to my fiancée, Kyongjin Song, whose love and support have inspired me, and to my parents and sister.

Table of Contents

List of Figures

List of Tables

List of Appendices

Abstract

Metal-organic frameworks (MOFs) have recently emerged as promising materials for the capture of carbon dioxide (CO_2) and the storage of gaseous fuels such as hydrogen (H_2) and methane (CH_4, the primary component of natural gas). Amongst the many possible MOFs, metal-substituted compounds based on Ni-DOBDC [Ni_2(DOBDC), $DOBDC^{4-}$ = 2,5-dioxido-1,4-benzenedicarboxtlate]$_n$ and HKUST-1 [$Cu_3(BTC)_2$, BTC = 1,3,5-benzenetricarboxylate]$_n$ have demonstrated the highest capacities for CO_2 and CH_4 at moderate pressures and temperatures. Here we explore the possibility for additional performance tuning within this series of compounds by computationally screening several metal-substituted variants with respect to their CO_2 adsorption enthalpies and CH_4 capacities. These compounds are denoted M-DOBDC and M-HKUST-1, where M refers to a coordinatively unsaturated metal site having the composition Be, Mg, Ca, Sr, Sc, Ti, V, Cr, Mn, Fe, Co, Ni, Cu, Zn, Mo, W, Sn, or Pb. These analyses are performed using a variety of computational techniques, ranging from dispersion-corrected Density Functional Theory to classical Monte Carlo, with the latter simulations employing customized interatomic potentials tuned by first-principles calculations.

Regarding CO_2 capture, our calculations find that substitutions involving alkaline earth metals (Mg, Ca, and Sr) in both M-DOBDC and M-HKUST-1, and early transition

metals (Sc, Ti, and V) in M-DOBDC yield relatively strong affinities for CO_2. Our screening identifies 13 MOFs having adsorption enthalpies within the targeted thermodynamic window -40 to -75 kJ/mol: 8 are based on M-DODBC (M = Mg, Ca, Sr, Sc, Ti, V, Mo, and W), and 5 on M-HKUST-1 (M = Be, Mg, Ca, Sr and Sc). Variations in the electronic structure and the geometry of the MOF's structural building unit are examined and used to rationalize trends in CO_2 affinity. In particular, the partial charge on the coordinatively unsaturated metal sites is found to correlate with the adsorption enthalpy, suggesting that this property may be used as a simple performance descriptor for carbon capture efficiency.

For methane storage, calculated adsorption enthalpies across a range of MOFs are generally found to be 10-20 kJ/mol less exothermic than for CO_2, consistent with a weaker, dispersion-based CH_4—MOF interaction. In parallel with these thermodynamic analyses, methane adsorption isotherms were predicted using Grand Canonical Monte Carlo (GCMC) simulations across the M-DOBDC and M-HKUST-1 series, with additional comparisons to prominent MOFs such as MOF-5, PCN-11, and PCN-14. A distinguishing feature of this work is the development of customized interatomic potentials that properly capture the interaction between CH_4 and coordinatively unsaturated metal sites. General interatomic potentials typically under-estimate these interactions, leading to poor agreement between simulated and measured isotherms. In contrast, the potentials developed here reproduce experimental uptake values in the benchmark Cu-HKUST-1 system very well; consequently, this approach was extended to predict CH_4 uptake in the remainder of the M-HKUST-1 series. In addition to predicting total capacities, the amount of *usable* stored methane was examined for two operating

scenarios: isothermal pressure swing (PS) and a combined temperature/pressure swing. Under these conditions, our calculations suggest that Ca-HKUST-1 and Fe-HKUST-1 should exceed the performance of Cu-HKUST-1, which currently holds the record for highest measured methane storage capacity. The proposed compositions are suggested as promising targets for experimental synthesis and characterization. A natural extension of this work could involve screening other metal-substituted MOF variants that contain the same Cu-paddlewheel structural building unit present in HKUST-1.

Chapter 1

Introduction

1.1 Motivation

1.1.1 Carbon Capture

The carbon dioxide (CO_2) concentration in the atmosphere has been increasing, resulting in global and regional climate changes via the so-called "green house" effect (i.e, reflection of radiations from the earth by the atmosphere).[1] Since the concentration of atmosphere CO_2 concentration was observed in the 1950s, it has continuously increased from a baseline of 320 ppm.[2] In May 2014 the National Oceanic & Atmospheric Administration's (NOAA) Mauna Loa Observatory announced that the concentration of CO_2 had reached 400 ppm, which is the highest level ever recorded.[2]

The high concentration of atmospheric CO_2 has been identified as a key contributor to climate change.[1] CO_2 and other green house gases (GHGs) adsorb radiation emitted from the earth and re-radiate (or reflect it) back

to the surface, resulting in an increase to the surface temperature. Although some amount of GHGs are necessary to maintain the earth's nominal temperature of approximately 15°C, excess GHGs intensify the re-radiation effect from the atmosphere.[1] The impact of climate change ranged from direct consequences, such as drought, flood, and extreme hot and cold temperature,[1] to secondary effects such as reduced public health, risk to the availability of fresh water, food insecurity, and destruction of infrastructures.[3]

Fossil fuel combustion is the primary source of GHG emissions,[4,5] accounting for approximately about 65% of all GHG emissions.[4] Annual global anthropogenic GHG emissions reached 49 $GtCO_2eq/yr$ in 2010 compared to 27 Gt/yr in 1970; approximately 76% of these emissions are attributed to carbon dioxide (Figure 1.1).[4] In the U. S., 94.2% of the CO_2 emissions can be trace to by fossil fuels.[5] Increasing energy use arising from population growth and economic development is the primary reason for projected increase in fossil fuel consumption (Figure 1.1).[4] The U. S. Energy Information Administration has estimated the domestic CO_2 emission will increase by 11% by 2040,[6] this despite the relatively mature state of the US economy and continuing investment in low-carbon power sources.

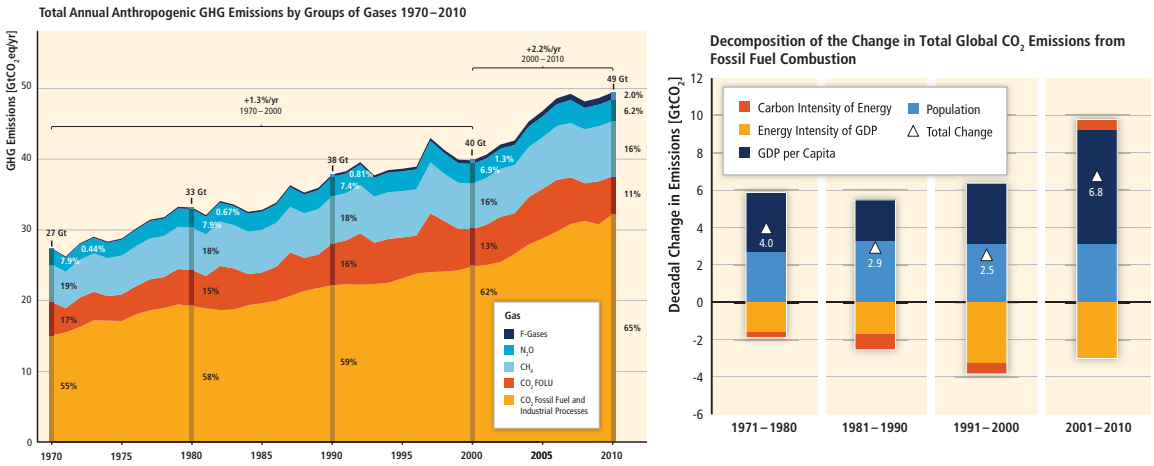

Figure 1.1(left) Total annual green house gas emissions by group of gases 1970-2010.[4] (right) Decomposition of the change in total global CO_2 emissions from fossil fuel combustion.[4]

Given its abundance and low cost, coal has become a cornerstone fuel for power generation.[4,6] Although use of natural gas has increased, coal's share of total energy generation in the U. S. stood 37% in 2012, and estimated to remain a significant player (32%) as far out as 2040.[6] Outside of the U. S., developing countries in Asia also make heavy use of coal for power generation.[4] Unfortunately, the high carbon intensity of coal makes it the largest source of CO_2 amongst common fuel.[5] Because coal combustion will likely remain a significant power source for the foreseeable future, technologies capable of reducing its carbon intensity are of immense value.

Carbon capture and sequestration (CCS) represents one approach for reducing the GHG emissions from coal-fired power plants.[7,8] CCS consists of three components: capture CO_2 from the flue gas, transport of CO_2 from the source to the storage sites, and storage of CO_2 within a suitable reservoir, such as underground geologic formations or in the ocean.[8] A portion of this thesis focuses on the first stage of CCS: efficient methods for adsorbing CO_2 from the flue gas stream of coal-fired power plant.

The state of the art approaches to CO_2 capture employs chemisorptive interactions with amine functional groups mono-ethanolamine (MEA).[7-11] Although this approach can capture a large fraction of the CO_2 effluent,[9] the CO_2 absorption process is characterized by a large (~80−110 kJ/mol) exothermic heat of absorption,[10,11] resulting in significant energy requirements for solvent regeneration.[12] These losses, and the associated problem of solvent degradation at high regeneration temperatures, consume up to ~30% of the power output,[12] with estimated cost of $72.2/tonne avoided of CO_2.[13] For comparison, the U. S. Department of Energy has established a cost target for the capture cost of CO_2 of less than $40/tonne in 2020-2025.[14] Moreover, a recent report by the American Physical Society reported that the optimal adsorption enthalpy for efficient carbon capture should fall within a range of -40 kJ/mol to -75 kJ/mol,[15] significantly lower than the MEA-based technologies.

Although the adsorption enthalpy is an important factor in minimizing regeneration energy, other properties must be considered when assessing the viability of a given MOF for carbon capture applications. The composition of flue gas from a coal-fired power plant is approximately 73-76% N_2, 15-16% CO_2, 5-7% H_2O, 3-4% O_2, 800 ppm SO_x, 500 ppm NO_x, and includes other trace gases such as HCl, CO, and hydrocarbons.[16] These properties include: selectivity for CO_2 over other components of the flue gas stream, hydrothermal stability, and robustness with respect to competitive adsorption of (i.e., poisoning from) SO_x and NO_x. Given the high concentration of N_2 in the flue gas, selectivity of CO_2 *vs.* N_2 is particularly important. Furthermore, reaction with water vapor can inhibit CO_2 adsorption, or in some cases decompose the MOF

itself.[17] Finally, even with the adoption of SO_x and NO_x reduction processes it is possible for trace quantities of these gases to effect the MOF's CO_2 adsorption properties.[18]

1.1.2 Natural Gas Storage

The production of natural gas in the U. S. has dramatically increased due to the development of hydraulic fracturing and horizontal drilling technologies.[6] In 2012, the U. S. produced 29,542 billion ft^3 of natural gas, compared to 19,182 ft^3 in 2000, making it the largest producer globally.[19] This abundance of natural gas is expected to have a major impact on U. S. energy policy and CO_2 emissions: natural gas power plant could be substituted for coal-fired power plants, and use of natural gas as a vehicular fuel (i.e., natural gas vehicles, (NGV)) could substantially reduce petroleum import, resulting in increased energy security.[6]

Methane is the primary component of natural gas.[20] With a ratio of one carbon atom to four hydrogen atoms, methane has the lowest carbon intensity of any common hydrocarbon fuel.[21] Also, lower concentration of impurities in natural gas compared to gasoline results in lower SO_x, and NO_x emissions.[22] Data from one field test showed that a natural gas engine emitted up to 76% less CO, 26% less CO_2, and 77% less NO_x, compare to a gasoline engine.[23] However, there exists some controversy regarding the overall GHG emissions from natural gas powered vehicles. Recent life cycle assessment of NGVs showed that NGVs have no or little benefit when the natural gas leakage from well to tank is accounted for.[24,25] More work is needed to quantify the role of fuel extraction and delivery on GHG emissions of NGV. Regardless, NGVs still present an advantage by reducing the dependence of the transportation sector on imported petroleum.

Perhaps the largest technical challenge impeding the widespread adoption of NGVs is the low volumetric energy density of natural gas. Refined natural gas is mostly composed of methane (CH_4),[20] except a small fraction of other light gases. Table 1.1 shows the general properties of methane gas. At standard temperature and pressure (STP), the volumetric energy density of CH_4 is 0.04 MJ/L. This is nearly 900 times less than the density of gasoline, 34.2 MJ/L.[26] Thus, liquefaction at -162 °C or compression at 250 bar are common strategies to increasing the energy density. However, these two processes require compromises in cost and efficiency. Liquefied natural gas (LNG) requires high-cost cryogenic cooling system for storage.[26] Also, to keep the methane temperature low during operating vehicles, a LNG tanks require additional insulations, and efficiency of the vehicle is dropped.[26] In the case of compressed natural gas (CNG), the primary concerns relate to the cost of compression and the on-board pressure vessel. Single stage compressors are not able to compress methane up to 250 bar; therefore expensive multi-stage compressors are required.[27] Moreover, to endure such a high pressure, tanks must be heavy and composed of thick walls; thus the usable space of vehicles is significantly reduced.[28] Finally, both two systems do not have enough infrastructures for re-fueling for wide market adaption.[29] The current cost to construct a natural gas re-fueling station is about $1.6M,[30] compared to about $100k for gasoline.[31]

Strong natural gas on-board in adsorbed form (i.e., adsorbed natural gas (ANG)) has the potential to overcome these challenges.[26,28] An ANG approach using a suitable solid adsorbent could reach higher volumetric densities than CNG at a specific pressure, or achieve a comparable density to high-pressure CNG (250 bar) but a much lower operating pressure (35 bar). Use of a lower pressure can the reduce the cost of the

compressor because a single stage system could be used.[34] Also, a low-pressure tank will exhibit weight and cost saving due to its thinner wall structure. In addition, at low pressures conformable (non-cylindrical) tank shapes become possible, allowing for use of "dead space" and an increase to total storage capacity.[35]

Table 1.1 General properties of pure CH_4

Critical temperature[32]	190.6 K
Boiling point[32]	111.7 K
Lower heating value[32]	50.0 MJ/kg
Kinetic diameter[33]	3.8 Å
Volumetric density (1 bar, 25 °C)[32]	0.9 v/v
Volumetric density (250 bar, 25 °C)[32]	263 v/v
Volumetric density (1 bar, -162 °C)[32]	591 v/v

In an ANG system, the storage capacity of the tank is critically dependent upon the adsorbent materials; thus identifying high-performing adsorbent is a rapidly growing area of materials research.[28] In 2012, the U.S. Department of Energy established new targets for CH_4 storage: 349 cm^3 (STP)/cm^3 and 0.5 g/g at room temperature.[36] To place these targets in context, well-known adsorbents such as activated carbons exhibit densities of 100 to 170 cm^3/cm^3,[37] and their predicted theoretical maximum is 194 cm^3/cm^3 at 34 bar, 298K.[38] Consequently, there is a clear need for new adsorbents with much higher CH_4 storage densities.

1.2 Metal Organic Frameworks

Metal Organic Frameworks (MOFs)[39-43] are promising materials for CO_2 capture,[44,45] and natural gas storage.[28,46,47] As previously described, MEA process for carbon capture is costly primarily due to the large (exothermic) enthalpy for CO_2 absorption. Also, conventional approaches to natural gas storage require high pressure to achieve moderate volumetric and gravimetric densities. In principle, use of a adsorbent material such as activated carbons, zeolites, and MOFs could overcome these limitation.[48,49] Many adsorbents exhibit moderated adsorption enthalpies and extremely, and a few have demonstrated large adsorption capacities. Among them, these MOFs are perhaps the most promising class of adsorbent materials due to their tunable properties, and crystalline structure.

1.2.1 Properties

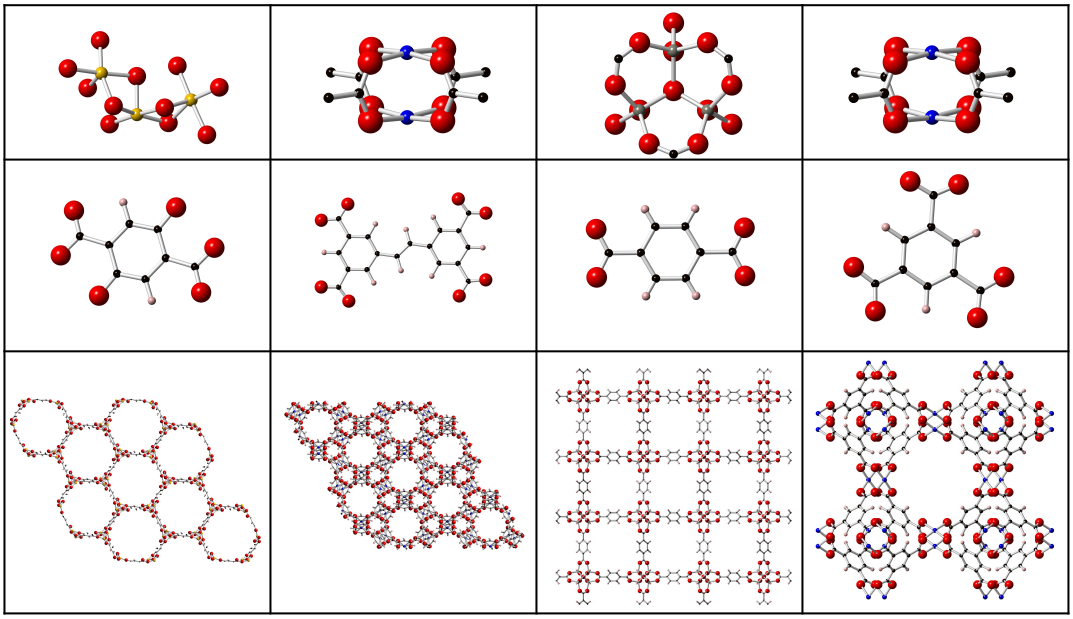

Figure 1.2 Example of (bottom) MOF structures, (top) Secondary Building Units, and (middle) organic linker: (a) Mg-DOBDC, (b) PCN-11, (c) MOF-5 and (d) Cu-HKUST-1

MOFs are nano-porous crystalline materials, which are constructed from metal ions or extended metal clusters, called secondary building units (SBU), assembled in a periodic fashion through coordination to organic linkers. Figure 1.2 shows four representative MOF structures: HKUST-1, Mg-DOBDC, PCN-11, and MOF-5. The large number of possible clusters and linkers allow for a tunable "building-block" approach to their synthesis, resulting in a wide variety of MOF structures and compositions.[50-53] For example, Tranchemontagne *et al.*[50] showed a large variety of SBUs. They discussed 131 possible geometries of the SBUs, and demonstrated that metal ions in each topology could be substituted with other metals. Also, Wilmer *et al.*[51] used 102 organic ligands and 5 SBUs to construct 137,953 hypothetical MOFs. Regarding known MOFs, Figure 1.3 shows the total number of MOF structures reported in Cambridge Structural Database

(CSD) from 1972 to 2002.[54] The graph shows an exponential increase of MOF structures, with a doubling time of only 3.9 years. This doubling time should be compared to that of the entire database, 9.3 years. In a more recent study, Goldsmith *et al*.[55] found ~22,500 possible MOFs structures within the same database in 2012. These data clearly show that the number of known and hypothetical MOFs is very large, indeed.

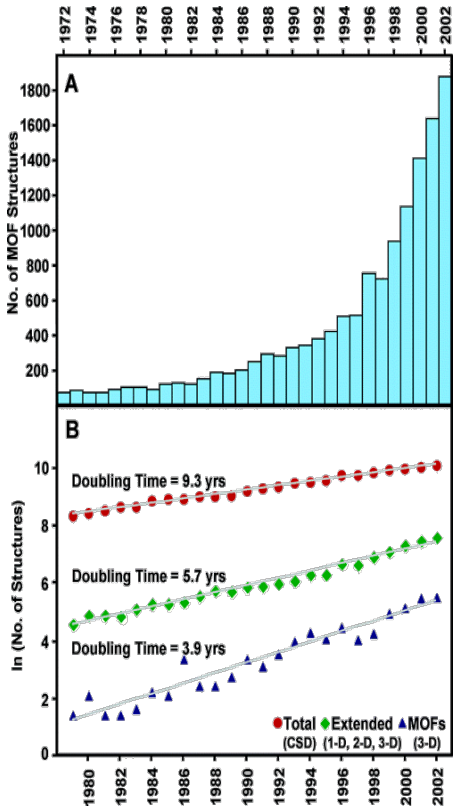

Figure 1.3 a) Total number of MOF in Cambridge Structural Database since 1972, b) Doubling time of MOFs, extended structures, and entire database. (Ref. 55)

Another unique property of MOFs is their extremely high surface areas.[56-58] In fact, MOFs hold the record for surface area, with some compounds exhibiting surface areas greater than 7000 m^2/g.[56] For example, the Brunauer-Emmett-Teller (BET) surface area of NU-109E, and NU-110E are 7010, and 7140 m^2/g, respectively.[56] Moreover,

these high surface areas directly correlate with the gravimetric adsorption capacity of gases.[59] Although MOFs are a relatively new class of materials, they have already surpassed the performance of ultrahigh surface area carbons, which had previously defined the limits of CO_2, and CH_4 capacity at high pressures. For example, Caskey *et al.*[60] have demonstrated that the MOF Mg-DOBDC [Mg_2(DOBDC), $DOBDC^{4-}$ = 2,5-dioxido-1,4-benzenedicarboxtlate]$_n$ exhibits the largest CO_2 uptake of any adsorbent at 1 bar. Also, Peng *et al*.[27] reported that HKUST-1 [$Cu_3(BTC)_2$, BTC = 1,3,5-benzenetricarboxylate]$_n$ has recorded the highest total volumetric CH_4 capacity at 35 bar, which is 227 cm^3/cm^3.

While many features have been suggested to impact CO_2 and CH_4 uptake in MOFs, we note that essentially all of the high-capacity MOFs contain coordinatively unsaturated metal sites, CUS.[60] In some SBU, metal ions form bonds with solvent molecules during synthesis. For example, Cu ions in the "paddle wheel" SBU of HKUST-1, [$Cu_2(O_2C)_4$] (See Figure 1.2 (d)), form four bonds with carboxyl oxygen atoms, with one additional bond with water molecules present in the synthesis solution. During the activation process, the water molecules are (in principle) evaporated, leaving behind Cu ions each having only 4 bonds. Although the water molecules are removed, there is no change to the geometry of the SBU. Therefore the Cu ions exist in a coordinatively unsaturated state. These CUS have been identified as important adsorption sites for many adsorbates, including CO_2 and CH_4.[61-63]

In addition to the possibility for high CO_2, and CH_4 capacities, recent studies have shown that metal substitution can be used to tune the performance of MOFs that contain CUS.[60,64] For example, Caskey *et al*.[60] demonstrated that isostructural substitutions of Mg,

Ni, and Co for Zn in Zn-DOBDC (See Figure 1.2 (a)) could dramatically alter CO_2 affinity;[65] more recent work has reported the synthesis of Fe-[66] and Mn-substituted[67] variants. Also, Wu *et al*.[68] have measured CH_4 capacities of Mg, Ni, Mn, Co, and Zn-DOBDC, with high excess capacities ranging from 149 to 190 cm^3/cm^3. HKUST-1 is another noteworthy example of a CUS-containing MOF that has demonstrated both high CO_2 capacity and potential for metal substitution.[69] In this MOF the metal cluster adopts a paddle wheel geometry with a square-planar coordination of the CUS metal.[61] In this case Cr[70], Ni[71], Zn[72], Ru[73], and Mo-substituted[74] variants of the original Cu-based compound have been synthesized, and tested adsorption enthalpies of CO_2.[75] As the CUS are a primary binding site for CO_2, and CH_4, the ability to substitute different CUS metals implies the ability to tune the adsorption enthalpy and capacity.

1.2.2 High-throughput Screening

The large number of MOFs is both a blessing and a curse. With many thousands of MOFs yet to be tested, it is highly likely that MOFs having superior properties for CO_2 capture and CH_4 storage exist. However, experimental testing of all MOF structures is impractical because synthesizing and testing MOFs is a expensive and time-consuming procedure.[76] Consequently, there is growing interest in the use of computational screening to identify promising CO_2 and CH_4 adsorbents.[51,55,77-81] Such an approach would reduce the number of compounds that need to be synthesized and tested, thereby accelerating the discovery of optimal materials.

High-throughput screening (HT) is defined as the a combination of an efficient computational technique that can rapidly predict a quantity of interest (i.e., performance

with respect to a certain application) with a large database of compounds upon which this analysis is to be applied.[76] This approach has been applied to a growing number of technologies, such as: catalysts,[82,83] solar energy conversion,[84] carbon capture,[77-79] methane storage,[51,80] *etc*. Cutarolo *et al*.[76] pointed out that 'descriptors' have a key role in HT. The 'descriptor' is connection from the calculated microscopic value to the targeted macroscopic material properties. For example, formation enthalpy is a 'descriptor' for the thermodynamic stability of a given crystal structure. Lin *et al*.[77] used the parasitic energy consumed during CO_2 adsorption as a descriptor to find optimal Zeolitic Imidazolate Frameworks (ZIFs) for carbon capture. Watanabe and Sholl[79] screened 1163 MOFs for CO_2/N_2 adsorption from the Cambridge Structural Database (CSD), and performed additional screening of these MOFs using Grand Canonical Monte Carlo (GCMC) and Molecular Dynamics (MD) simulations. For CH_4 adsorption, Wilmer *et al*.[51] examined 10^5 hypothetical MOFs with respect to their volumetric CH_4 uptake. Martin *et al*.[80] designed 18,000 hypothetical porous polymer networks (PPNs) and tested their CH_4 capacities. Finally, Goldsmith *et al*.[55] screened over 22,500 MOFs mined from the CSD for their H_2 solubility using the empirical relationship known as the Chahine rule.

1.3 Goals

The purpose of this thesis is to accelerate the discovery of promising metal organic frameworks for applications in carbon capture and natural gas storage through computational simulations. This is accomplished by direct prediction of selected MOF properties that directly relate to their performance, and by revealing trends that can be exploited to narrow the space of promising compounds. To achieve these goals a multi-

scale simulation protocol is employed. This protocol includes linkages to several known and hypothetical MOFs taken either from the CSD or which have been generated using composition variation (i.e., metal substitution) involving compounds previously shown to be amenable to such substitutions. The gas adsorption properties of these MOFs are subsequently computed using a combination of quantum-mechanical (Density Functional Theory) and classical techniques (Grand Canonical Monte Carlo). These techniques are linked via the creation of customized force fields generated by fitting to DFT data. These potentials are used to minimize the errors typical of general, "off the shelf" force fields, resulting in more accurate predictions of gas uptake.

Before proceeding further, we give a brief outline of this thesis:

In chapter 2 we discuss the computational methodology. We start by introducing the computational framework for our approach to materials discovery. Next, we introduce the fundamentals of Density Functional Theory and its extension via van der Waals corrections (vdW-DFT). Finally, we introduce the basics of GCMC simulations.

Chapter 3 describes a benchmarking study of the van der Waals augmented DFT for carbon capture. More specifically, we compare two van der Waals-DFT methods: the semi-empirical DFT-D2 method and the *ab initio* vdW-DF scheme. The performance of these methods is evaluated by calculating the enthalpy of adsorption for CO_2 in Mg-, Ni-, Co-DOBDC, and HKUST-1, and comparing with experimental data. It is determined that the vdW-DF method is in very good agreement with experimental enthalpies, with the revPBE-based (vdW-DF1 method) functional yielding the smallest deviation from experiments.

In chapter 4 we analyze the energetics and electronic structure of CO_2 adsorption in 36 metal-substituted MOFs based on M-DOBDC and M-HKUST-1. We find that 13 of these MOFs exhibit enthalpies of CO_2 adsorption that fall within the optimal range. Electrostatic interactions are found to dominate the MOF-CO_2 interaction, with the atomic charge on the metal ion serving as a good descriptor of the magnitude of the adsorption enthalpy.

Chapter 5 begins the discussion of natural gas storage, with an emphasis on thermodynamics and capacity. Results from vdW-DF2 calculations across 18 metal-substituted variants of M-DOBDC reveal that CH_4 adsorption is generally weaker than for CO_2; the dominant interaction for CH_4 adsorption is not electrostatic forces, but rather weak van der Waals interactions. Total and usable capacities of CH_4 are simulated by GCMC simulations, and an analysis of the predictive accuracy of several different interatomic potentials is performed. Our analysis shows that Be-DOBDC achieves the highest total volumetric uptake at various pressures; however on a usable basis PCN-11 and MOF-5 emerge as the top-performers. This approach is then extended to explore the CH_4 capacities across several hundred MOFs extracted from the CSD.

In chapter 6 we discuss the fitting procedure for generating accurate interatomic potentials from vdW-DF calculations. These potentials are subsequently used in GCMC simulations to predict CH_4 uptake across the M-HKUST-1 series. We identify Ca-, and Fe-HKUST-1 as promising compounds that should exceed the performance of the current record holder for CH_4 uptake, Cu-HKUS-1.

Finally, chapter 7 concludes this thesis with summary of our findings and a brief discussion of possible extensions.

The main chapters of this dissertation (Chapter 3-6) include the results presented in the following publications:

1. Rana, M. K.; Koh, H. S.; Hwang, J. H.; Siegel, D. J., *Comparing van der Waals Density Functionals for CO_2 Adsorption in Metal Organic Frameworks*, Journal of Physical Chemistry C, 2012, 116 (32), 16957-16968.
2. Koh, H. S; Rana, M. K.; Hwnag, J. H.; Siegel, D. J. *Theromodynamic Screening of Metal-Substituted MOFs for Carbon Capture*, Physical Chemistry Chemical Physics, 2013, 15 (13), 4573-4581.
3. Rana, M. K.; Koh, H. S.; Zuberi, H.; Siegel, D. J., *Methane Storage in Metal Substituted MOFs: Thermodynamics, Usable Capacity, and the Role of Strong Binding Sites*, Journal of Physical Chemistry C, 2014, 118(6), 2929-2942.
4. Koh, H. S.; Rana, M. K; Sigel, D. J. *Increased Methane Storage in M-HKUST-1 via Metal Substitution*, Journal of the American Chemical Society, Submitted.

Chapter 2

Methodology

2.1 Computational Framework for MOF Discovery

We used a high-throughput methodology to discover promising MOFs for carbon capture and methane storage. This procedure includes high-throughput screening of MOFs from a customized database using first principles and classical simulations, followed by analysis of the results to reveal correlations and/or performance descriptors. A flow diagram summarizing this workflow is given in figure 2.1.

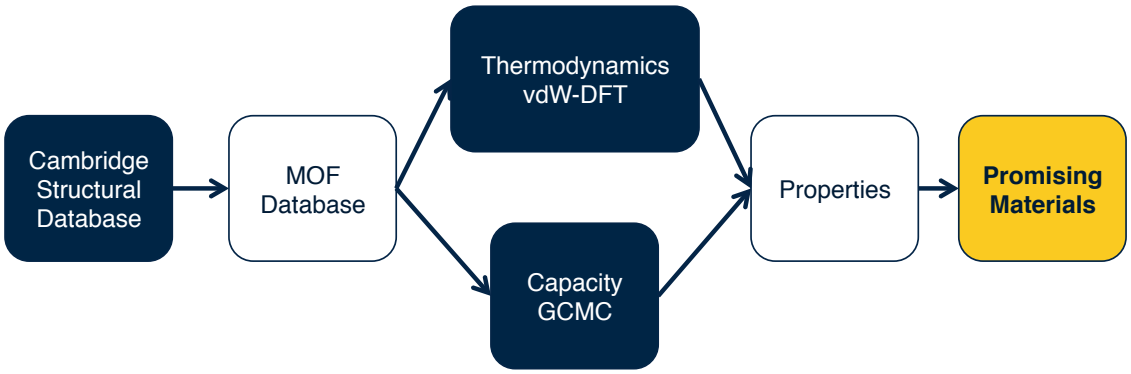

Figure 2.1 Computational Framework for MOF Discovery

First step of the discovery is data mining from the Cambridge Structural Database.[85] Cambridge Structural Database has structural data of more than 550,000 organic compounds. However, the database generally does not distinguish MOFs from the other molecular compounds. In prior work, Goldsmith *et al.*[55] identified possible MOF structures from the database using a data-mining approach. After collecting the MOFs, the structures were "cleaned up" for ready to simulations, and these cleaned MOF structures are components of new MOF database. More detail of this process is in Goldsmith *et al.*[55]

Next, hypothetical MOFs are constructed by altering the composition of a subset of the known MOFs in our database. Metal-substitution and functional group addition are examples of methods by which the performance of MOFs can be altered. Our focus has been to characterize the impact of metal substitution; these hypothetical structures are geometrically optimized using DFT. The mind and hypothetical MOFs are components of MOF database upon which screening is performed.

Next step in the procedure is calculating the adsorption properties of MOFs through van der Waals augmented Density Functional Theory (DFT) and Grand Canonical Monte Carlo (GCMC) simulations. The adsorption affinity and nature of bonding are analyzed using electronic structure calculations. In this dissertation, we analyze adsorbate-MOF interactions by calculating adsorption energies, adsorption enthalpies, and charge density differences. Moreover, calculated adsorption energies are used as reference energies for parameterizing force-fields for GCMC simulation. The GCMC is able to estimate the adsorption isotherm directly; nevertheless, the accuracy of the simulation depends sensitively upon the force-field.

Finally, the new hypothetical MOFs and their calculated properties are analyzed, and added to a database. If the predicted performance proves noteworthy (e.g., a particular MOF has high uptake or potential for efficient regeneration), that compound is suggested for further testing via experimental synthesize and characterization.

In this study we adopt a database of known MOFs generated by Goldsmith *et al*. Therefore, we focus on the steps associated with estimation of the adsorption properties of known MOFs and of hypothetical MOF variants generated by metal substitution. .

2.2 Van der Waals Augmented Density Functional Theory

2.2.1 Conventional Density Functional Theory

Quantum mechanical simulation is one approach to calculate adsorption enthalpies and to analyze the bonding nature of an adsorbed molecule. Adsorption at CUS is generally electrostatic in nature when it involves a polarizable molecule such as CO_2. Van der Waals interactions between the MOF structures and gas molecules can also contribute to adsorption. To include these interactions, advanced van der Waals augmented Density Functional Theory is required to improve quality of calculations.

Density Functional Theory (DFT)[86,87] is a widely-used approach to solve the Schrödinger equation in a many-body system. The Schrodinger equation for a many-body system consisting of N electrons and M ions is given by:

$$\mathcal{H}\Psi(r_1, r_2, \cdots, r_N; R_1, R_2, \cdots, R_M) = E\Psi(r_1, \cdots, r_N; R_1, \cdots R_N), \qquad (2.1)$$

where H, Ψ, and E are the Hamiltonian operator, the many-body wavefunction, and the total energy of system, respectively. The Hamiltonian operator includes all interactions between electrons and nuclei:

$$\mathcal{H} = \frac{-\hbar^2}{2m_e}\sum_i \nabla_i^2 - \frac{-\hbar^2}{2M_I}\sum_I \nabla_I^2 - \frac{1}{2}\sum_{i,I}\frac{Z_I e^2}{|r_i - R_I|} + \frac{1}{2}\sum_{i\neq j}\frac{e^2}{|r_i - r_j|} + \frac{1}{2}\sum_{I\neq J}\frac{Z_I Z_J e^2}{|R_I - R_J|} \quad (2.2)$$

Here the first two terms represent, respectively, the kinetic energy of electrons and nuclei; and the remaining three terms represent electrostatic interactions between electrons and ions, electrons and electrons, and between ions and ions, respectively. The wavefunction, Ψ, has 3N+3M degrees of freedom. Thus, analytically solving this equation is impractical in all but the smallest of systems.

The Born-Oppenheimer approximation[88] reduces the 3N+3M degrees of freedom to 3N. The immense mass difference between electrons and nuclei allows for approximating the nuclear positions as frozen. Thus, the many-body Hamiltonian (Eq. 2.2) can be decoupled in an electron part and a nuclear part. For the purposes of understanding bonding interactions and the thermodynamics of adsorption it is sufficient to only solve the electronic part explicitly.

Density Functional Theory (DFT) further reduces the degrees of freedom by introducing the concept of charge density. Hohenberg and Kohn[86] demonstrated that the ground state charge density, $n_o(r)$, for a system of electrons in an external potential, $V_{ion}(r)$, uniquely determines that potential up to an arbitrary constant. Also, Kohn and Sham[87] states that total energy of the system is a universal functional of the charge density $E[n(r)]$; when the charge density is in its ground state, $n_0(r)$, the total energy, E, is a global minimum (i.e., the ground state energy).

Furthermore, DFT allows the many-body problem to be expressed using the charge density rather than the 3N-dimensional wavefunction:[87]

$$E[n(r)] = T_0[n(r)] + \int V_{ion}(r)n(r)dr + E_h[n(r)] + E_{XC}[n(r)]. \quad (2.3)$$

Here $T_0[n(r)]$, $V_{ion}(r)$, $E_h[n(r)]$, and $E_{XC}[n(r)]$ are the many-body kinetic energy, ionic potential, the classical Coulomb interaction, and the exchange correlation energy, respectively. These can be expressed as:

$$T_0[n(r)] = \frac{-\hbar^2}{2m_e}\sum_{i=1}^{N}\langle\psi_i|\nabla^2|\psi_i\rangle \quad (2.4)$$

$$E_h[n(r)] = \frac{1}{2}\int \frac{n(r)n(r')}{|r-r'|}drdr' \quad (2.5)$$

$$n(r) = \sum_{i=1}^{N}|\psi_i(r)|^2 \quad (2.6)$$

Equation 2.6 expresses the charge density in terms of non-interacting single-particle wavefunctions, ψ_i. The exchange-correlation energy, $E_{XC,}$ in principle includes all quantum-mechanical effects not accounted for by the other terms in the energy functional, such as electron exchange and correlation..

Equation 2.3 can be solved via direct minimization or through a self-consistent approach using a set of single-particle Schrödinger-like equations, called the Kohn-Sham equation for non-interacting wavefunctions.[87]

$$\hat{h}\psi_i(r) = \left[\frac{-\hbar^2}{2m}\nabla^2 + V_{eff}[n(r)]\right]\psi_i(r) = \epsilon_i\psi_i(r) \quad (2.7)$$

$$V_{eff}[n(r)] = V_{ion}[n(r)] + V_h[n(r)] + V_{XC}[n(r)], \quad (2.8)$$

$$V_h[n(r)] = \frac{\delta E_h[n(r)]}{\delta n(r)} \tag{2.9}$$

$$V_{XC}[n(r)] = \frac{\delta E_{XC}[n(r)]}{\delta n(r)} \tag{2.10}$$

To solve the Kohn-Sham equation, an approximate form of the exchange and correlation energy is required. The exact form of this functional is unknown, and the quality of this approximation largely determines the accuracy of the DFT method. The most common approach is to adopt a local approximation.[87] In general, E_{XC} can be expressed using the exchange-correlation energy density,ϵ_{XC}:

$$E_{XC}[n(r)] = \int \epsilon_{XC}[n(r)]n(r)dr. \tag{2.11}$$

The local approximation assumes that ϵ_{XC} at some point r within the system is equal to the exchange-correlation energy in a homogenous electron gas of the same density, n[r]:

$$\epsilon_{XC}[n(r)] = \epsilon_{XC}^{hom}[n(r)]. \tag{2.12}$$

The E_{XC} of a homogenous gas can be accurately calculated using Quantum Monte Carlo (QMC). Further improvements to the accuracy can be achieved by incorporating gradients in the density. This is known as the, Generalized Gradient Approximation (GGA),[89].and is widely used in the modern DFT calculations.

The DFT/GGA approach has proven successful in predicting the properties of many classes of materials. However, one case in which DFT is known to perform poorly is in the treatment of systems exhibiting non-local long-range dispersion energies. As these interactions are important for the physisorption of molecules on surfaces, conventional DFT (LDA and GGA) yield rather poor predictions of adsorption thermodynamics in these cases.[61,86,90] The absence of vdW interactions has limited the applicability of DFT in modeling CO_2 and CH_4 uptake in MOFs. For example, using a

conventional GGA functional, Wu *et al*.[61] reported an enthalpy of adsorption of 20 kJ/mol for CO_2 adsorption in Mg/DOBDC, which significantly underpredicts the experimental value of 47 kJ/mol.[60]

The inclusion of vdW interactions in density functional theory (DFT) is an active area of research, and several approaches[90-98] have been proposed. Two notable methods are the semi-empirical approach of Grimme, variously referred to as DFT-D1,[99] DFT-D2,[100] and DFT-D3,[101] and the non-empirical vdW-DF method of Dion et al.[102] These methods have demonstrated improved accuracy at moderate computational cost across a range of chemical environments.[91,103-107]

2.2.2 DFT-D2

The DFT-D2 method,[100] similar to its successor DFT-D1,[99] adds a dispersion contribution, E_{disp}, to the conventional Kohn-Sham DFT energy, $E_{KS\text{-}DFT}$, to give a dispersion-corrected total energy:

$$E_{DFT-D2} = E_{KS-DFT} + E_{disp} \tag{2.13}$$

The form of E_{disp} is given by:

$$E_{disp} = s_6 \sum_{i<j} \frac{C_6^{ij}}{R_{ij}^6} f_{dmp}(R_{ij}) \tag{2.14}$$

Where,

$$f_{dmp}(R_{ij}) = \frac{1}{1 + e^{-d\left(\frac{R_{ij}}{R_0^{ij}} - 1\right)}} \tag{2.15}$$

$$C_6^{ij} = \sqrt{C_6^i C_6^j} \tag{2.16}$$

$$R_0^{ij} = R_0^i + R_0^j \tag{2.17}$$

Here, C_6 is the atomic dispersion coefficient, which is determined from DFT-PBE0[108] calculations of atomic ionization potentials (I_p) and static dipole polarizabilities (α) through the empirical relation:

$$C_6 = 0.05 N I_p \alpha \tag{2.18}$$

N assumes values of 2, 10, 18, 36, and 54 for atoms from rows 1−5 of the periodic table. The factors 0.05 and N are chosen to reproduce the experimental binding energies and bond distances of rare gas dimers (Ne− Xe) and some weakly interacting complexes.[100] s_6 is a global scaling factor, which depends upon the specific density functional employed, R_0^i is the van der Waals radius of the i[th] atom (computed as in DFT-D1[99]), d determines the steepness of the damping function, and R_{ij} is the interatomic distance between atoms i and j. f_{dmp} is a damping function used to avoid singularities at small R_{ij} and to minimize dispersion contributions from interactions within typical (i.e., covalent) bonding distances. Our DFT-D2 calculations employ the PBE-GGA[89] functional and therefore follow the convention of using $s_6 = 0.75$ and a damping parameter d = 20.[100] The atomic dispersion coefficient and van der Waals radii are set to default values, which are summarized in the Appendix (Table A.1). The maximum range of the dispersion interaction E_{disp} is set to 30 Å.

2.2.3 vdW-DF

The vdW-DF methods take as their starting point the adiabatic-connection fluctuation−dissipation (ACFD) theorem[109] and plasmon-pole approximation for the

response of electron density. In this method[102] the correlation energy is divided into local and nonlocal parts,

$$E_c = E_c^0 + E_c^{nl} \tag{2.19}$$

With the total exchange-correlation energy given by:

$$E_{XC} = E_X^{GGA} + E_c^0 + E_C^{nl} \tag{2.20}$$

Here, E_X^{GGA} is GGA exchange energy, and the local part of the correlation energy, E_c^0, is treated with the LDA. The nonlocal component, E_c^{nl}, accounts for long-ranged electron correlation effects responsible for van der Waals interactions, and is evaluated using a double integral over electron densities *n(r)* at two different locations, *r* and *r'*.

$$E_c^{nl} = \frac{1}{2}\iint n(r)\Phi(r,r')n(r)drdr' \tag{2.21}$$

Here, $\Phi(r,r')$ is non-local kernel, which is a operator of the charge density, its gradient at *r* and *r'*, and $|r-r'|$. Since E^{nl} is only a function of distance, evaluation of eq (2.21) can be expedited by tabulating in terms of *r* and *r'* in advance. Additional information can be found in ref 102.

In this study we consider the following vdW-DFs: revPBE-vdW, which is the "original" vdW-DF introduced in ref 102, and the four variants introduced by Klimes and co-workers,[110,111] optB86b, optB88, optPBE, and Lee et al.,[112] rPW86 (vdW-DF2). The latter four functionals differ from the revPBE-vdW in their choice of the exchange energy, E_x^{GGA}, corresponding to the first term on the right-hand side of eq (2.19)

2.2.4 Implementation: VASP

Van der Waals augmented DFT calculations were performed using the Vienna ab initio Simulation Package (VASP)[113]. The projector-augmented-wave (PAW) method[114]

was used to describe interactions between core and valence electrons. The ground state charge density and energy were calculated using a Block Davison algorithm[115] coupled with a Pulay mixing scheme.[116] A regular Monkhost-Pack[117] grid, suitably reduced for symmetry, was used for sampling of reciprocal space. A conjugate gradient algorithm[118] performed geometric optimizations of atom positions within the computational cell.

2.2.5 Adsorption Enthalpy (ΔH)

Adsorption energies ΔE were calculated using the following expression:

$$\Delta E = \frac{1}{n}(E_{MOF+Gas} - E_{MOF} - E_{Gas}) \tag{2.22}$$

where, E_x is the total energy of the Gas-containing MOF, the MOF itself, and a Gas molecule (CO_2 or CH_4), respectively. The number of adsorbed CO_2 and CH_4 molecules contained in the MOF unit cell is given by n.

The initial binding energies (Δ E) obtained by our calculations are static, 0 K energies and do not include zero point (E_{ZPE}) and thermal energy (E_{TE}, T = 0 → 300 K) contributions. To compare with experimental measurements of CO_2 and CH_4 adsorption enthalpies at room temperature, finite-temperature enthalpic contributions were calculated within the harmonic approximation.[119,120] Normal-mode vibrational frequencies were determined for the relaxed DFT-D2 and vdW-DF structures using the so-called direct method.[121] For supercells containing MOFs or MOFs with adsorbed gas, thermal energy contributions arise primarily from vibrational contributions. Thus, the enthalpy of a MOF or MOF+gas supercell can be written as:

$$H^{MOF} = E0 + E_{ZPE} + E_{TE} \tag{2.23}$$

$$E_{ZPE} = \frac{\hbar\omega_i}{2} \tag{2.24}$$

$$E_{TE} = \sum_i \frac{\hbar\omega_i}{\exp\left(\frac{\hbar\omega_i}{K_B T}\right) - 1} \tag{2.25}$$

where E_0 is the static total energy, E_{ZPE} is the zero point energy, E_{TE} is the thermal energy due to vibrational contributions, k_B is the Boltzmann constant, and ω_i is the vibrational frequency for the i^{th} normal mode. In contrast, the enthalpy of gas-phase CO_2 is given by an identical expression plus an additional contribution of 7/2 k_BT arising from translational, rotational, and PV degrees of freedom; this contribution is equal to 4 k_BT for a CH_4 molecule. Replacing E by E_{ZPE} and E_{TE} on the right-hand side of eq (2.23) allows for the isolation of ZPE (ΔE_{ZPE}) and thermal energy contributions (ΔE_{TE}) to the adsorption energy. Taking into account the ZPE and TE, the adsorption enthalpy is calculated as

$$\Delta H = \Delta E + \Delta E_{ZPE} + \Delta E_{TE} \tag{2.26}$$

We set T=300K in all of our calculations. Finally, we define the static dispersion energy contribution arising from use of vdW-corrected density functionals as ΔE_{vdW}. This contribution is calculated relative to the static PBE-GGA binding energy such that

$$\Delta E_{vdW} = \Delta E_{vdW-DFT} - \Delta E_{GGA} \tag{2.27}$$

2.3 Grand Canonical Monte Carlo (GCMC)

2.3.1 Monte Carlo Simulation

Monte Carlo (MC) and molecular dynamics (MD) simulations are classical molecular simulation techniques that can to describe materials' properties at the atomic scale. Compared to MD, which integrates Newton's laws of motion to evolve the dynamics of a system in time, MC is governed by statistical mechanics. Conventional MC schemes are independent of time [one exception being Kinetic Monte Carlo (KMC)][122], and the simulation is focused on evaluating the average properties of a system, such as average number adsorbed molecules at specified temperature and pressure within a MOF. In a typical MC simulation the system reaches equilibrium after progressing through a number of "start-up" steps; upon reaching equilibrium new configurations are sampled from a specified thermodynamic ensemble.[123] Common ensembles used in MC simulations include: canonical, micro canonical, and grand canonical ensembles, As will be described in more detail below, the Grand Canonical ensemble is the most commonly used ensemble for simulating gas uptake isotherms. For example, in a MC simulation of adsorption, the equilibrium state would correspond to a configuration containing an equilibrium number of adsorbed molecules.

Figure 2.2 provides a flow chart of one MC step for an adsorption process. From a starting configuration, the algorithm first chooses a trial movement for a selected adsorbate molecule from amongst 4 choices: insertion, deletion, translation, and rotation. Then, using the chosen movement a new configuration is generated. Based on the energy of the new configuration the movement is either accepted or rejected based on an

'acceptance rule'. If the movement is accepted, the new configuration replaces the old configuration; if not, then the algorithm returns to the original configuration. The process then begins again.

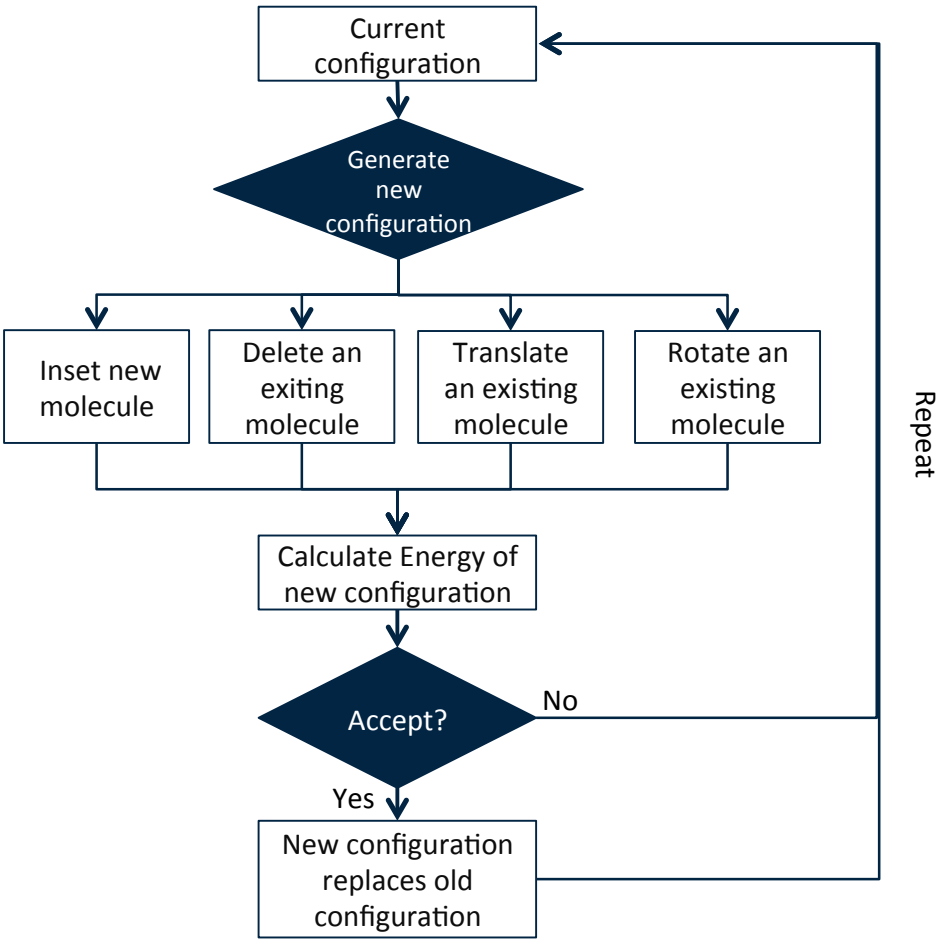

Figure 2.2 Flow chart describing the a MC step for simulating gas adsorption within the grand canonical ensemble.

Random number generation is one of the key components of the MC algorithm.[124] For instance, in adsorption calculations, the algorithm requires the generation of 3 or 4 random numbers for each MC step. The first random number chooses the movement type. A second number is generated to describe movements such as a new molecule's coordinates for insertion, or for choosing one of the existing molecules for deletion,

translation, or rotation. For translation and rotation the method requires one more random number to specify the size of the displacement from an original position or a rotation. Finally, another random number is used for deciding whether the trial move is accepted or rejected Thus, all MC algorithms rely upon an efficient random number generator.

A second key component in MC simulation is the acceptance rule. The acceptance rule determines whether a (new) trial configuration is accepted as a new configuration. Here we discuss the widely-used acceptance rule described by Metropolis *et al.*[125] As previously described, the MC algorithm generates random trial configurations from the original or old state (o) to a new state (n). We define $P_{eq}(o)$ and $P_{eq}(n)$ as the probability of finding the system in state o and n, respectively. In addition, $\pi(o \rightarrow n)$ and $\pi(n \rightarrow o)$ are the transition probability to go from state o to n. Invoking the concept of detail balance, it is possible to relate the configuration probabilities and transition probabilities:

$$P_{eq}(o)\pi(o \rightarrow n) = P_{eq}(n)\pi(n \rightarrow o) \tag{2.28}$$

In other words, in equilibrium the average number of accepted moves from n to o is exactly equal to the number of reverse moves. $\pi(o \rightarrow n)$ can be divided two terms: the first being a matrix determining the probability for a trial movement from state n to o ($\alpha(o \rightarrow n)$), and the second being the probability of accepting the trial movement, $P_{acc}(o \rightarrow n)$.

$$P_{eq}(o)\alpha(o \rightarrow n)P_{acc}(o \rightarrow n) = P_{eq}(n)\alpha(n \rightarrow o)P_{acc}(n \rightarrow o) \tag{2.29}$$

In Metropolis scheme,[125] α is symmetric matrix:

$$\alpha(o \rightarrow n) = \alpha(n \rightarrow o) \tag{2.30}$$

Thus, the statement of detailed balance reduces to

$$P_{eq}(o)P_{acc}(o \rightarrow n) = P_{eq}(n)P_{acc}(n \rightarrow o) \tag{2.31}$$

which leads to

$$\frac{P_{acc}(o \to n)}{P_{acc}(n \to o)} = \frac{P_{eq}(n)}{P_{eq}(o)} \tag{2.32}$$

There are many possible choices for $P_{acc}(o \rightarrow n)$. Metropolis *et al.*[125] adopted the following acceptance rule,

$$P_{acc}(o \to n) = \min\left(1, \frac{P_{eq}(n)}{P_{eq}(o)}\right) \tag{2.33}$$

The probabilities, $P_{eq}(o)$ and $P_{eq}(n)$ are calculated using the probability distribution of an specified thermodynamic ensemble.

2.3.2 Grand Canonical Monte Carlo

Most common monte carlo method for studying adsorption is grand canonical monte carlo (GCMC)[126]. GCMC uses the grand canonical ensemble to calculate the relative probabilities of a particular microstate that is consistent with the specified macrostate (for example, determined by a fixed temperature and pressure). In turn, these probabilities determine the acceptance rule for generating new configurations/microstates through Eq. 2.33. The grand canonical ensemble describes thermodynamic equilibrium in open system which can exchange particles with an imaginary reservoir. In this case the chemical potential (μ), temperature (T), and pressure (P) are constants, and determined by interactions with the infinitely large reservoir.

The partition function for the grand canonical ensemble (Ξ) can be written in terms of the canonical ensemble partition function, Q(N,V,T):

$$\Xi(\mu, P, T) = \sum_{N=0}^{\infty} e^{\beta\mu N} Q(N, V, T), \tag{2.34}$$

where N is the number of particles, and $\beta = 1/k_B T$. The partition function of the canonical ensemble is given by:

$$Q(N,V,T) = \frac{1}{h^3 N!} \iint e^{-\beta H(p^N, r^N)} dp^N dr^N, \tag{2.35}$$

where H is the Hamiltonian operator, r is the Cartesian coordinate of a particle, and p represents momenta. The Hamiltonian operator consists of momentum and potential energy terms:

$$H = \sum_i \frac{p_i^2}{2m_i} + U(r^N), \tag{2.36}$$

where m is the mass of a particle, U is its potential energy. In MC method particles do not have explicit velocities, rather a thermodynamic average of velocity is used instead. The momentum term can therefore be reduced:

$$\int e^{-\beta\left(\sum_i \left(p_i^2/2m_i\right)\right)} dp = \left(\frac{2\pi m}{\beta}\right)^{(3/2)N}. \tag{2.37}$$

Additionally, by defining the de Broglie wavelength (Λ), and the fractional coordinate (s),

$$\Lambda \equiv \left(\frac{h^2 \beta}{2\pi m}\right)^{1/2} \tag{2.38}$$

$$s = L^{-1} r, \tag{2.39}$$

the canonical partition function can be further simplified:

$$Q(N,V,T) = \frac{1}{\Lambda^3 N!} \int e^{-\beta U(r^N)} dr^N = \frac{V^N}{\Lambda^3 N!} \int e^{-\beta U(s^N; L)} ds^N. \tag{2.40}$$

Now, we substitute this partition function into the grand canonical partition function:

$$\Xi(\mu,P,T) = \sum_{N=0}^{\infty} \frac{V^N e^{\beta \mu N}}{\Lambda^{3N} N!} \int e^{-\beta U(s^N; L)} ds^N. \tag{2.41}$$

Thus, the probability of a specific configuration can be expressed as:

$$P(s^N, V) \propto \frac{V^N e^{\beta\mu N}}{\Lambda^{3N} N!} e^{-\beta U(s^N;L)}. \tag{2.42}$$

The acceptance rule can be derived from equation (2.33). More specifically, the rule for insertion is given by:

$$\frac{P_{acc}(o\to n)}{P_{acc}(n\to o)} = \frac{P_{eq}(n)}{P_{eq}(o)} = \frac{V e^{\beta\mu}}{\Lambda^3 (N+1)} e^{-\beta\left[U_n(s^{N+1};L) - U_0(s^N;L)\right]}; \tag{2.43}$$

for deletion:

$$\frac{P_{acc}(o\to n)}{P_{acc}(n\to o)} = \frac{\Lambda^3 N}{V e^{\beta\mu}} e^{-\beta\left[U_n(s^{N-1};L) - U_0(s^N;L)\right]}; \tag{2.44}$$

for translation and rotation:

$$\frac{P_{acc}(o\to n)}{P_{acc}(n\to o)} = e^{-\beta\left[U_n(s^N;L) - U_0(s^N;L)\right]}. \tag{2.45}$$

Note that the rules for translation and rotation are same since these two movements have no change in the number of particles. Therefore, the acceptance rule for particle movement is same as in the canonical ensemble.

The insertion and deletion acceptance rules can be further simplified by using relations connecting chemical potential and pressure:

$$\beta\mu = \beta\mu_{IG}^0 + \ln(\beta f) \tag{2.46}$$

Here,

$$f = \phi p, \tag{2.47}$$

where f is fugacity, ϕ is fugacity coefficient, and μ_{IG}^0 is the chemical potential of an ideal gas at the reference state (25°C, 1 atm). The μ_{IG}^0 is defined as

$$\mu_{IG}^0 \equiv \frac{\ln(\Lambda^3)}{\beta} \tag{2.48}$$

With the above substitutions the acceptance rules in GCMC can be expressed as:

Insertion:

$$P_{acc}(o \to n) = min\left(1, \frac{\beta V f}{N+1} e^{-\beta[U_n(s^{N+1};L) - U_0(s^N;L)]}\right); \quad (2.49)$$

Deletion:

$$P_{acc}(o \to n) = min\left(1, \frac{N}{\beta V f} e^{-\beta[U_n(s^{N-1};L) - U_0(s^N;L)]}\right); \quad (2.50)$$

and translation or rotation:

$$P_{acc}(o \to n) = min\left(1, e^{-\beta[U_n(s^N;L) - U_0(s^N;L)]}\right) \quad (2.51)$$

2.3.3 Force-fields

A force-field (or interatomic potential) is used to calculate the potential energies (U) in GCMC simulations. The force-field is a set of functions that describe atom-atom interactions. Generally, the force-field is divided into two components: bonding and non-bonding interactions. The bonding part includes energy contributions arising from bond stretching, bending, and torsion; the non-boing component includes van der Waals, electrostatic, and hydrogen bonding interactions. In GCMC simulations of adsorption, it is common to treat the framework and gas molecules as rigid entities; hence there is no change to bonding in the framework or adsorbed molecules. One can therefore set the potential energies of intra-framework and intra-molecular interactions to zero. Only frameworks-gas molecule interactions are non-zero. Since in most cases these interactions are of the weak, physisorption type – i.e., there exists no direct orbital overlap typical of the formation of strong covalent bonding – only non-bonding terms are used to describe MOF-adsorbate interactions in GCMC simulations.

As previously mentioned, non-bonding terms are a superposition of van der Waals and electrostatic interactions. To describe the electrostatic component, a Coulomb form is used:

$$E_Q(r) = \frac{qq'}{r}, \tag{2.52}$$

where q and q' are the point charges of two atoms separated by a distance r. For van der Waals interactions there are many choices of the potential form. In this study a Lennard-Jones 12-6 potential and Morse potential are used. The Lennared-Jones potential is given by:

$$E_{vdW} = D_0 \left[\left(\frac{R_0}{r}\right)^{12} - 2\left(\frac{R_0}{r}\right)^{6} \right], \tag{2.53}$$

where D_0 is the depth of potential well, and R_0 is the equilibrium bond length. Several common interatomic potentials such as Driding,[127] Universal (UFF),[128] and TraPPE[129] employ this potential form. Alternatively, the Morse potential can be written as:

$$E_{vdW} = D_0 \left[\left(1 - e^{-\alpha(r-R_0)}\right)^2 - 1 \right], \tag{2.54}$$

where α represent the width of the potential well. Compared to the 12-6 form, the Morse potential contains an additional fitting parameter which can improve its accuracy . This potential is adopted for the customized potential described in chapter 6.

Also, many general potentials (Direding, UFF, and TraPPE) specify only homonuclear interaction parameters such as C-C, and O-O. Consequently, the Lorenz combination rule is applied to determine force-field parameters between non-identical atoms. The Lorenz combination rule is given by the following two expressions:

$$D_{0\_ij} = \sqrt{D_{0\_i} D_{0\_j}} \tag{2.55}$$

$$R_{0\_ij} = \frac{R_{0\_i} + R_{0\_j}}{2}. \tag{2.56}$$

Here, D_{0_i}, and R_{0_i} represent D_0 of i atom, and R_0 of i atom, respectively.

2.3.4 Computational Details

The Sorption module in Accelrys Materials Studio was used for all GCMC calculations.[130] The crystal structure was relaxed using Density Functional Theory in cases where the MOF composition was varied by metal substitution; the MOF was then treated as a rigid framework during GCMC calculations. GCMC sampling was performed using a Metropolis Monte Carlo scheme with three types of moves: exchange (consisting of insertion and deletion of a CH_4 molecule), translation, and rotation, with respective probabilities of 2:1:1. In all cases 10^6 monte carlo steps were used to equilibrate, followed by $2x10^6$ additional cycles to estimate uptake at a given temperature-pressure pair. Isotherms were calculated over the pressure range of 0-100 bar. Usable capacities were estimated assuming both isothermal pressure swing (PS, P_{min} = 5 bar, T = 298 K) and temperature + pressure swing (TPS, P_{min} = 5 bar, T = 323 K) scenarios. Additional isotherms were collected at slightly elevated temperatures (323 K) to estimate the TPS capacity. The excess adsorption is computed according to:

$$N_{excess} = N - \rho_{bulk} \times V_{pore}, \tag{2.57}$$

where N is the total number of adsorbed molecules, ρ_{bulk} is bulk density of methane at a specified temperature and pressure, and V_{pore} is the pore volume of the MOF, which was calculated using the PLATON[131] code.

Chapter 3

Predicting the Thermodynamics of Carbon Capture in MOFs: Comparison of Various Density Functional Theory Methods

3.1 Introduction

As a screening parameter, the energetics (i.e., enthalpy) of CO_2 adsorption is of particular importance as it impacts the capacity[44,45,65], selectivity[45], and efficiency of the carbon capture process[12,15]. Also, we discuss previously, van der Waals augmented DFT can increase accuracy of adsorption energy calculation. Thus, in this chapter, we benchmark various vdW-DF methods for Mg-, Ni-, Co-DOBDC, and Cu-HKUST-1 systems.

The DFT-D methods[99-101] involve the addition of a damped dispersion term (E_{disp}) to the Kohn−Sham DFT energy (E_{KS-DFT}). A similar scheme has been proposed by Wu et al.[132] The accuracy of all of the DFT-D methods[99-101] depends on the atomic dispersion coefficient, C_6. In the DFT-D1 method,[99] this term is derived from experimental molecular polarizability data,[133] which, unfortunately, can be scarce for heavier elements. In the subsequent DFT-D2 implementation,[100] the C_6 coefficients are derived from computed atomic ionization potentials and polarizabilities. Elements in the same row of a given transition metal series are treated as having identical dispersion parameters,[100]

taken as the average of the preceding group VIII and following group III elements. DFT-D2 has been shown to yield accurate experimental binding energies and equilibrium bond lengths for dimers of Krypton;[134] it improves the interlayer binding energy, layer−layer spacing, lattice parameters, and bulk moduli in layered solids such as graphite;[103,135-137] it also provides better agreement with quantum chemical reference data for the binding energies of weekly interacting dimers[100,135] in the S22 training set.[138] Regarding CO_2 adsorption, Valenzano and co-workers have shown that this approach can partially correct for the underbinding observed in B3LYP calculations for CO_2 on Mg/DOBDC.[139]

In contrast to the empirical underpinnings of the DFT-D2 approach, the vdW-DF method[102] includes vdW interactions in a nonempirical fashion. Initial tests of the vdW-DF method demonstrated improved accuracy in describing interactions in noble gas and benzene dimers.[102,140] Several other systems have since been explored with this formalism, including water interactions with benzene and other polycyclic aromatic hydrocarbons;[107,141] biomolecules such as nucleobase pairs and DNA, in which H-bonding and stacking interactions are crucial;[142,143] layered solids such as graphite and V_2O_5;[136,144] and physisorption of molecules onto surfaces[91,145] and within porous materials.[146] In these systems, the vdW-DF method showed improved agreement with experimental data or QC predictions, and generally outperformed conventional density functional calculations.[110,111]

More recently, Klimes et al. have demonstrated that the performance of the vdW-DF can depend sensitively upon the choice of the exchange functional.[110,111] For example, by replacing the revPBE-based functional employed in ref. [102] with a modified B88 functional[111] (referred to as the "optB88" functional), more accurate binding energies

were obtained for the methane dimer and for the S22[138] test set. Mean absolute deviations from reference CCSD(T) binding data for this set decreased from ~6 kJ/mol using revPBE-vdW to ~1 kJ/mol for optB88-vdW. Klimes et al.[110,111] also explored three other exchange functionals: "optPBE", "optB86b", and "rPW86."[112] However, benchmarking on the S22 set revealed that the accuracy of these functionals was less than for optB88.

Given the large improvements reported in refs. [111] and [110], upon altering the exchange functional, the goal of this study is to benchmark these same vdW functionals, along with the DFT-D2 method and conventional LDA and PBE-GGA functionals, against experimental enthalpies for CO_2 adsorption across four MOFs: M/DOBDC (M = Mg, Ni, Co) and HKUST-1.[67,69,147-149] All of the selected MOFs contain coordinatively unsaturated metal sites (CUS). These compounds are of interest because the presence of CUS correlates with high CO_2 uptake at low pressures,[44] presumably due to stronger CO_2−metal interactions. In addition, the thermodynamics of CO_2 adsorption in these systems have been experimentally measured by multiple groups,[60,150-158] adding to the reliability of the data.

Our calculations demonstrate that the LDA and PBE-GGA partially capture trends in the experimental ΔH values; nevertheless, these functionals significantly overbind (LDA) and underbind (GGA) CO_2 with respect to the experimental data. The addition of a semiempirical C_6R^{-6} dispersion term to the GGA exchange-correlation energy using "off the shelf" DFT-D2 parameters results in a substantial improvement in both the magnitude of the adsorption enthalpies and the trends across compounds. However, on average this approach still underbinds CO_2 as compared to the experimental data by 7 kJ/mol CO_2 (~18% of the experimental ΔH). Improved accuracy can be obtained with some

of the vdW density functionals. In particular, the revPBE functional yields a low absolute average error of only 2 kJ/mol CO_2 (4%) relative to experiment. This improvement in energetics is accompanied by a slight decrease in the accuracy of geometries, as the revPBE functional overestimates the metal−CO_2 bond length by about 10%. Our results are in good agreement with a nearly simultaneous study of CO_2 adsorption in Mg/DOBDC, which compared several vdW density functionals.[159] The identification of an efficient vdW density functional capable of accurately predicting the thermodynamics of CO_2 adsorption will facilitate computational screening for optimal carbon capture materials.

3.2 Summary of Methods

As previously mentioned, our calculations are aimed at evaluating the heat of adsorption (ΔH) of CO_2 in four MOFs containing coordinatively unsaturated metal sites (CUS). Three of the MOFs are isostructural variants of M/DOBDC,[60,67,147-149] where M = Ni, Mg, Co, with the fourth being Cu-HKUST-1.[69] The atomic structures of Ni/DOBDC and HKUST-1 were obtained from published literature data;[69,147] initial structures for Mg and Co/DOBDC were created by substituting Mg and Co for Ni in Ni/DOBDC. The primitive unit cells of DOBDC and HKUST-1 contain 54 and 156 atoms with 6 and 12 open metal sites, respectively. MOF structures containing adsorbed CO_2 were constructed from diffraction measurements[61,155] on Ni/DOBDC and HKUST-1. These measurements exhibit one CO_2 adsorption site per CUS metal.[61,155] Similar to what was done for the bare MOF structures, metal substitution was used to generate initial geometries for Mg and Co/DOBDC containing adsorbed CO_2. Including adsorbed CO_2 molecules, the

primitive cells used in our calculations contained 72 atoms in the case of M/DOBDC-based systems, and 192 atoms for HKUST-1-based systems. All calculations on DOBDC-based compounds employed space group $R\bar{3}$ (No. 148); for HKUST- 1, groups $Fm\bar{3}$ (No. 202) and $Fm\bar{3}m$ (No. 225) were used, respectively, for supercells with and without CO_2.

The energy of adsorption per CO_2 molecule was calculated using eight different forms for the energy functional. These include the Ceperley-Alder LDA,[160] PBE GGA,[89] Grimme's DFT-D2 method,[100] and five vdW-DFs in which the exchange-correlation energy is given by one of optB86b-vdW,[110] optB88-vdW,[111] optPBE-vdW,[110] revPBE-vdW,[102] and the modified PW86 functional, referred to as rPW86-vdW or vdW-DF2.[112] The energy of an isolated CO_2 molecule was evaluated using a supercell of dimension 10 × 11 × 12 Å. The bond length of free CO_2 was calculated to be 1.168 Å in the LDA, and ranged from 1.174 to 1.179 Å in the GGA and the GGA-based DFT-D2 or vdW-DF methods. In comparison, the experimental bond length is 1.161 Å.[161]

k-point convergence testing was performed on the Mg/DOBDC and HKUST-1 supercells using mesh densities of 1 × 1×1, 2×2×2, and3×3×3.The variation of CO_2 binding energies (ΔE) at 0 K with respect to k-point sampling density is shown in the Appendix (Table A.2). We find that a k-point mesh of 1 × 1 × 1 is sufficient to converge CO_2 binding energies to within 0.3 and <0.1 kJ/mol, respectively, for Mg/ DOBDC and HKUST-1. Hence, all calculations employ a 1 × 1 × 1 (Γ-point only) mesh.

The structures of the four empty MOFs and their respective CO_2-containing variants were initially optimized by relaxing the unit cell lattice parameters and atomic positions using the LDA or PBE-GGA. To assess the impact of van der Waals

contributions on geometries, structure optimizations were also performed using the revPBE-vdW. The optimized lattice parameters for these MOFs and their corresponding MOF+CO_2 systems are given in the Appendix (Table A.3), and are compared to experimental data. In general, the agreement between the predicted and measured lattice constants is very good. Consistent with prior reports, the average LDA lattice constants are slightly smaller than the experimental values, while the PBE-GGA and revPBE-vdW predictions are slightly larger. As the difference between the PBE-GGA and revPBE-vdW lattice constants is small, 1−2%, structural differences between functionals result in negligible changes to adsorption energies on the order of 1 kJ/mol CO_2. (See Table 3.1 for a comparison of revPBE-vdW adsorption energies calculated with the PBE-GGA and revPBE-vdW lattice constants.) Consequently, the relaxed PBE-GGA lattice constants were used in subsequent adsorption energy calculations employing the DFT-D2 and vdW-DF methods. In the latter cases, the atomic coordinates were reoptimized by minimizing atomic forces to a tolerance of less than 0.01 eV Å. Regarding the impact of CO_2 adsorption on MOF volume, neutron diffraction experiments by Queen et al.[162] found that the volume of Mg/DOBDC varied by less than 0.4% upon adsorption of 1 CO_2 per Mg site. Similarly, computed cell volumes for all functionals change by a negligible amount upon CO_2 adsorption, Appendix Table A.3.

The ground-state magnetic configuration and corresponding magnetic moments were determined for the relaxed MOFs with and without adsorbed CO_2. The presence of adsorbed CO_2 was found to have a negligible effect on magnetic properties. In the case of Co and Ni/DOBDC, a ferromagnetic ground state was

observed with respective magnetic moments of ~3 and ~2 μ_B per metal atom. On the other hand, Cu spins in HKUST-1 adopt an antiferromagnetic configuration with a moment of $0.55\mu_B$.

3.3 Results and Discussion

3.3.1 Adsorption Energies

Calculated CO2 adsorption energies (ΔE) and enthalpies (ΔH) in M/DOBDC (M = Mg, Ni, Co) and Cu-HKUST-1 across all eight examined functionals are reported in Table 3.1. We adopt a sign convention in which negative energies/enthalpies correspond to an exothermic adsorption interaction. The calculated values are compared to adsorption data from 21 experimental measurements culled from the recent literature.[60,150-152,154,156-158] The MOFs examined in this study were chosen on the basis of the existence of at least two independent and consistent experimental measurements of the CO_2 adsorption enthalpy. Because our calculations model the low coverage regime of one CO_2 per metal site, we have selected experimental data at low CO_2 partial pressures, typically less than 10 kPa. A comprehensive listing of the details for each experiment, including temperature, pressure, loading, and methods used, is given in Table 3.2. Experimental data (e.g., −73 kJ/mol for Mg/DOBDC)[153] that differed significantly from the majority of other measurements were excluded. However, even with the exclusion of out-lying data, in cases such as HKUST-1 there remains a large spread in the experimental data. For this MOF, we identified seven enthalpy measurements, ranging from 12.1 to 35 kJ/mol. Presumably, the variation can be attributed to differences in

sample handling, post-synthesis activation processes (i.e., cleanness of the MOF),[60,153] and numerical uncertainties associated with the isotherm fitting technique used to extract ΔH.[158,163,164] Because it is not obvious which data are most reliable, we compare the calculated enthalpies against the mean experimental ΔH for CO_2 adsorption in each MOF, which is given in bold type in Table 3.1. (The standard deviation of the experimental data is reported as "±" in Table 3.1 and with error bars in Figure 3.1.)

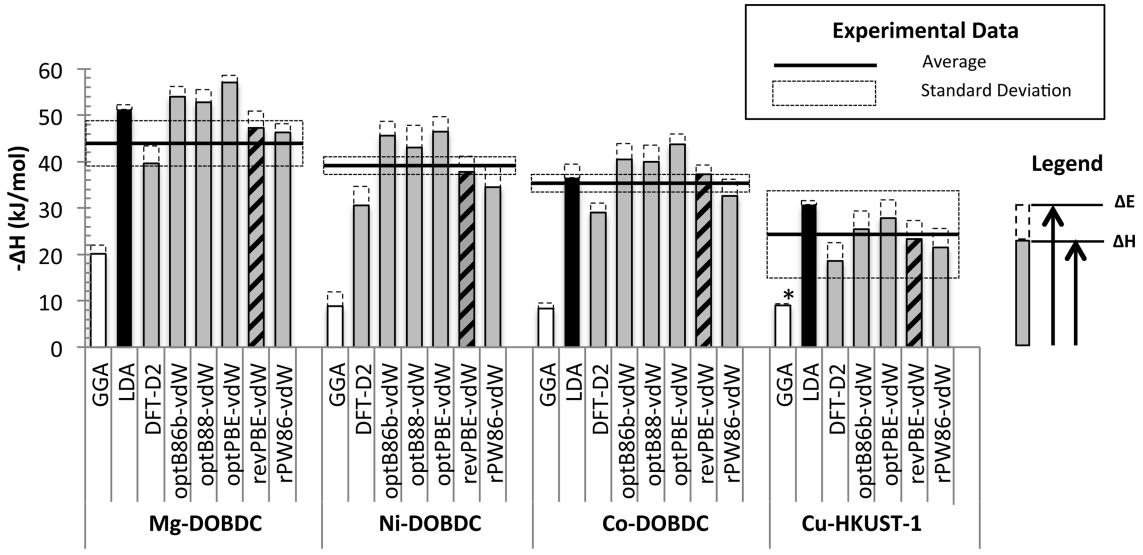

Figure 3.1 CO_2 adsorption energies in M/DOBDC (M = Mg, Ni, Co) and HKUST-1 calculated using standard density functional methods (LDA and GGA), the semiempirical DFT-D2 method of Grimme, and five nonempirical GGA-based vdW density functionals. The black, white, and gray columns depict adsorption enthalpies (ΔH) calculated with LDA, PBE-GGA, and vdW DFT methods, respectively. (Gray/black cross-hatching is used to highlight the revPBE-vdW functional, which yields the best agreement with experimental data.) The total column height represents the 0 K static binding energy, and the dashed segment at the top indicates the sum of zero point (ZPE) and thermal energy (TE) contributions at T = 300 K. The average experimental ΔH is given as a horizontal line; the standard deviation in the experimental data is given by a dashed box. * ZPE+TE contribution for Cu-HKUST-1 in the PBE-GGA sum to −0.5 kJ/mol.

Table 3.1 Comparison of Calculated CO_2 Adsorption Energies (in kJ/mol) with Experimental Data

System	Method	ΔE	ΔE_{vdW}	ΔE_{zpe}	ΔE_{TE}	ΔH	% error	ΔH (exp)
Mg/DOBDC	LDA	-52.3		2.4	-1.3	-51.2	15.8	-44.2±4.6
	PBE	-22.0		1.9	-0.1	-20.2	-54.3	(47,[60] 47,[150]
	DFT-D2	-43.4	-21.4	2.2	1.5	-39.7	-10.2	43,[152] 39,[152]
	optB86b-vdW	-56.2	-34.2	2.1	0.2	-53.9	21.9	39,[151] 42.8,[153]
	optB88-vdW	-55.5	-33.5	2.6	0.1	-52.8	19.5	51.6[154])
	optPBE-vdW	-58.7	-36.7	2.1	-0.6	-57.2	29.4	
	revPBE-vdW	-50.9	-28.9	2.1	1.5	-47.3	7.0	
	rPW86-vdW	-48.2	-26.2	2.1	-0.1	-46.2	4.5	
	B3LYP+D*[139]	-41.5	-23.3	2.1	1.6	-37.9	-14.3	
	MP2:B3LYP+D*[139]	-46.3				-42.7	-3.4	
	LDA[61]	-51.2						
	PBE[61]	-20.2						
Ni/DOBDC	PBE	-12.0		1.8	1.4	-8.8	-77.8	-39.6±1.5
	DFT-D2	-34.8	-22.8	2.9	1.3	-30.6	-22.7	(41,[60] 38,[152]
	optB86b-vdW	-48.6	-36.6	2.4	0.6	-45.6	15.2	41.1,[154] 40[155])
	optB88-vdW	-47.9	-36.6	3.0	1.8	-43.1	8.8	
	optPBE-vdW	-49.8	-37.8	2.5	0.7	-46.6	17.7	
	revPBE-vdW	-41.3	-29.3	1.7	1.8	-37.8	-4.5	
	rPW86-vdW	-39.1	-27.1	3.1	1.5	-34.5	-12.9	
	B3LYP+D*[139]	-38.9	-26.9	2.0	1.4	-35.5		
	MP2:B3LYP+D*[139]	-43.9				-40.5		
Co/DOBDC	LDA	-39.4		2.0	0.8	-36.6	2.5	-35.7±1.9
	PBE	-9.6		1.4	-0.1	-8.3	-76.8	(37,[60] 34.3[154])
	DFT-D2	-31.1	-21.5	1.7	0.4	-29.0	-18.8	
	optB86b-vdW	-43.9	-34.3	1.7	1.8	-40.4	13.2	
	optB88-vdW	-43.6	-34.0	2.0	1.7	-39.9	11.8	
	optPBE-vdW	-46.0	-36.4	1.6	0.7	-43.7	22.4	
	revPBE-vdW	-39.3	-29.7	1.6	0.5	-37.2	4.2	
	rPW86-vdW	-36.2	-26.6	1.8	1.9	-32.5	-9.0	
Cu-HKUST-1	LDA	-31.5		1.7	-0.8	-30.6	29.1	-23.7±8.2
	PBE	-8.9		2.7	-3.2	-9.4	-60.3	(35,[156] 25,[156]
	DFT-D2	-22.5	-13.6	4.8[a]	-0.8[a]	-18.5	-21.9	30,[157] 27.5,[154]
	optB86b-vdW	-29.4	-20.5	4.8[a]	-0.8[a]	-25.4	7.2	21.5,[154] 12.1[158]
	optPBE-vdW	-31.7	-22.8	4.8[a]	-0.8[a]	-27.7	16.9	14.6[158])
	revPBE-vdW	-27.3	-18.4	4.8[a]	-0.8[a]	-23.3	-1.7	
	rPW86-vdW	25.5	-16.6	4.8[a]	-0.8[a]	-21.5	-9.3	
	DFT/CC[165]	-31.5						
	LDA[61]	-32.7						
	PBE[61]	-7.3						

[a]ZPE and TE contributions for the vdW density functionals were evaluated using DFT-D2

Table 3.2 Heat of Adsorption as a Function of Temperature, Pressure, and Loading As Measured by Various Experiments in the Literature

System	ΔH (kJ/mol)	Temp. (K)	Pressure (kPa)	Loading			Method for ΔH calculation
				wt%	(mol CO_2)/ (kg MOF)	(no. CO_2)/ metal site	
Mg/DOBDC	-47	273.296	~0	0.50	0.11	0.01	Toth, C-C[60]
	-47	232-303	NR	NR			Langmuir,VH[150]
	-43	278-298	1-4	18.13	4.12	0.5	From isotherm[152]
	-39	278-298	3-8	24.30	5.52	0.67	From isotherm[152]
	-42.8	278-318	0-107	NR			Sip model[153]
	-73	278-318	~0	0.88	0.20	0.02	Langmuir, C-C[153]
	-51.6	311	10	21.70	4.93	0.60	Toth, VH[154]
	-39	273-298	NR	NR			Virial expansiont[151]
Ni/DOBDC	-41	273,296	~0	0.50	0.11	0.02	Toth, C-C[60]
	-38	278-298	2-7	14.13	3.21	0.50	From isotherm[152]
	-38	278-298	4-9	18.93	4.30	0.67	From isotherm[152]
	-41.1	311	10	13.11	2.98	0.46	Toth, VH[154]
	-40	303-353	~8	7.00	1.59	0.25	TSA[155]
Co/DOBDC	-37	273,296	~0	0.50	0.11	0.02	Toth, C-C[60]
	-34.3	311	10	7.92	1.80	0.28	Toth, VH[154]
HKUST-1	-35	120-290	NR	0.44	0.10	0.02	SIM[156]
	-25	120-290	NR	23.77	5.40	1.09	SIM[156]
	-30	278-298	NR	NR			PSA (DTA)[157]
	-27.5	311	10	1.76	0.40	0.08	Toth, VH[154]
	-21.5	311	10	1.85	0.42	0.08	Toth, VH[154]
	-12.1	300	0.2-133	NR			Lanmuir[158]
	-14.6	300	~0	NR			TAP[158]

NR: not reported, C-C: Clausius-Clapeyron, VH: van't Hoff, PSA: pressure swing adsorption, TSA: temperature swing adsorptions, SIM: sorption isosteric method, DTA: differential thermal analysis, TAP: temporal analysis of products.

3.3.2 Conventional LDA and GGA Functionals

We first turn to results obtained using the conventional LDA and PBE-GGA functionals. As previously mentioned, these functionals do not account for long-ranged electron correlation effects such as vdW interactions. Consequently, we expect limited agreement with experimental data in environments where these interactions are important. This expectation is largely confirmed based on the static 0 K binding energy data (ΔE) in Table 3.1, which shows that the LDA and GGA systematically overbind (ca. 10−32%)

and underbind CO_2 (<50%), respectively, in all four MOFs as compared to the experimental energies. Similar over- and underestimates between LDA and GGA have been reported for a range of other properties such as lattice parameters, bulk moduli, and atomization energies.[110,166-169] A distinction between the LDA and PBE-GGA is evident in their ability to reproduce the experimental trend in ΔH across the four MOFs: $\Delta H^{Mg/DOBDC} > \Delta H^{Ni/DOBDC} > \Delta H^{Co/DOBDC} > \Delta H^{Cu\_HKUST\_1}$. Whereas the LDA correctly captures this trend, the PBE-GGA is only partially successful in the regard as it predicts $\Delta H^{Cu\_HKUST\_1}$ to be more exothermic than $\Delta H^{Ni/DOBDC}$ and $\Delta H^{Co/DOBDC}$. Figure 3.1 provides a graphical depiction of the calculated adsorption energies and their comparison with experiments. Here, the height of the white and black bars represents the GGA and LDA ΔH values, respectively. The dashed portion at the top of each bar indicates the magnitude of zero point and thermal energy contributions. (In the case of Ni/DOBDC, we do not report energetics for the LDA functional due to difficulties in achieving convergence to the magnetic ground state.)

Our LDA and GGA binding energies are in good agreement with previous DFT calculations by Wu et al.[61] on Mg/DOBDC and Cu-HKUST-1. In the case of Mg/DOBDC, we find LDA (GGA) values of 52.3 (22.0) kJ/mol, while for Cu-HKUST-1 we find 31.5 (8.9) kJ/mol (see Table 3.1). Similarly, Wu et al.[61] found LDA (PBE-GGA) values of 51.2 (20.2) kJ/mol for Mg/ DOBDC, and 32.7 (7.3) kJ/mol for Cu-HKUST-1.

Because zero point and thermal energy contributions generally result in a more endothermic CO_2−MOF interaction (see Table 3.1), their inclusion in the underbound GGA data worsens agreement with experiment. On the other hand, these contributions have the opposite effect on the (overbound) LDA energies, improving agreement with

experimental enthalpies to within approximately 15%. As we describe below, additional improvements are possible with functionals that account for vdW interactions.

3.3.3 Semi-empirical DFT-D2 Method

We next examine the performance of the semiempirical DFT-D2 functional,[99,100] which was used in conjunction with the PBE-GGA. Our calculated dispersion-corrected adsorption energies (ΔE) and enthalpies (ΔH) are summarized in Table 3.1. In Figure 3.1 binding energies at 0 K are represented by the combined height of the gray columns and the dashed caps at top. In all of the MOFs examined, the dispersion contribution (ΔE_{vdW}) is significant, ranging from −13.6 kJ/mol in HKUST-1 to −22.8 kJ/mol in Ni/DOBDC. (The value of Edisp is roughly constant at −22 kJ/mol across the entire M/DOBDC series.) As a consequence of the large size of E_{disp}, the use of DFT-D2 results in a significant improvement in CO_2 adsorption enthalpies as compared to the underbound PBE-GGA. For example, in Mg/DOBDC, ΔH decreases from −20.2 kJ/mol (GGA) to −39.7 kJ/mol (DFT-D2), substantially improving agreement with the experimental value of −44.2 kJ/mol. This is similartothevalueof−37.9kJ/molobtainedwiththeB3LYP +D* functional.[139,150]

Factoring in zero point and thermal energy contributions, on average the DFT-D2 adsorption enthalpies are about 18% too endothermic as compared to the average experimental enthalpies. Nevertheless, the experimental trends in ΔH across the MOFs are correctly reproduced by this method. Given that the LDA already overbinds CO_2 in these MOFs, and that most efforts aimed at including vdW interactions into DFT focus

on GGA-based functionals, we did not conduct LDA-based DFT- D2 calculations. (Presumably such an approach would worsen the overbinding behavior observed with the LDA alone.) We emphasize that the present results were obtained using "off the shelf" coefficients for the dispersion energy. We expect that additional improvements in accuracy could be obtained by optimization of the atomic dispersion coefficients. However, given the promising results obtained with the vdW-DF's (described below), such an optimization was not attempted.

3.3.4 van der Waals Density Functionals

Table 3.1 and Figure 3.1 also report the energetics of CO_2 adsorption predicted by the five vdW density functionals: optB86b-vdW, optB88-vdW, optPBE-vdW, rPW86-vdW (also known as vdW-DF2),[110-112] and the original revPBE-vdW.[102] As compared to DFT-D2, all of the vdW-DF's yield more exothermic vdW contributions, with values ranging from −16.6 to −22.8 kJ/mol in HKUST-1 and from −26.2 to −37.8 kJ/mol across the M/DOBDC series. While a more exothermic interaction would offset the underbinding observed in DFT-D2, in three of the five vdw- DF's the vdW contribution is so large that it results in overbinding of CO_2 with respect to experimental measurements. This is the case for optB86b-vdW, optB88-vdW, and optPBE-vdW, where inclusion of vibrational and thermal contributions yields ΔH values that are, respectively, 21.9%, 19.5%, and 29.4% more exothermic than the average experimental values for Mg/DOBDC. (In the case of HKUST-1, we do not report energetics for the optB88-vdW functional due to difficulties in achieving convergence to the antiferromagnetic spin state.[170])

In contrast to the overbinding observed for optB86b-vdW, optB88-vdW, and optPBE-vdW, the ΔH values predicted by revPBE-vdW and rPW86-vdW do not show a tendency for systematic under- or over-prediction of CO_2 enthalpies. In general, these two functionals yield the best agreement with the experimental enthalpies. As shown in Table 3.1, the average error in ΔH with respect to the experimental data across all four MOFs is 8.9% for rPW86-vdW, and only 4.4% (~2 kJ/mol) for revPBE-vdW. To place these values in context, we note that the standard deviation in the experimental ΔH values for the M/DOBDC series is 6.8%. For HKUST-1, the experimental uncertainty is much larger, 34.6%. Therefore, for the MOFs examined here, the revPBE-vdW method is capable of predicting adsorption thermodynamics with accuracy comparable to that of experimental measurements.

Regarding trends in the binding energies, we note that the energies predicted by the vdW functionals across the different MOFs can be rank-ordered as: optPBE > optB86b > optB88 > revPBE > rPW86. That is, optPBE generally results in overbinding of CO_2, whereas rPW86 results in the weakest binding. As previously mentioned, for the vdW functionals considered here, the local and nonlocal correlation components of the exchange-correlation energy ($E_c^0 + E_c^{nl}$) are identical. Therefore, trends in the binding energies can be rationalized in terms of short-ranged repulsion arising from the differing functionals used for the exchange energy E_X^{GGA}.[110,111,159] More specifically, it has been shown that functionals having large values of the exchange energy enhancement factor $F_x(s)$ yield weaker binding, and vice versa. (F_X appears in the expression for the exchange energy density:$\varepsilon_X(n,s) = \varepsilon_X^{LDA}(n)F_X(s)$,where ε_X^{LDA} is the LDA exchange energy density and *n* is the charge density.)

Figure A.2 in the Appendix plots F_x as a function of the reduced density gradient s. For Mg/DOBDC and Ca/ BTT, it has been shown that the distribution of reduced density gradient values is peaked around $s = 1$. Assuming that the distribution is similar in the present systems, Figure A.4 demonstrates that, with the exception of optPBE, the magnitude of F_x for the various functionals at $s = 1$ closely follows the trend in their relative binding energies. In the case of optPBE, the large overbinding can be explained by its preponderance of PBE exchange, which is known to result in attractive interactions in cases where it should not.[111]

3.3.5 Zero point and Thermal Energy Contributions

In concluding this section, we comment on the significance of zero point energies (ΔE_{zpe}) and thermal energy contributions (ΔE_{TE}) to the adsorption enthalpy. As shown in Table 3.1, both ΔE_{zpe} and ΔE_{TE} are small in comparison to the vdW contributions. Within the M/DOBDC series, ΔE_{zpe} assumes a relatively constant value of approximately 2−3 kJ/mol; ΔE_{zpe} is slightly larger, ~5 kJ/mol, in HKUST-1. As $\Delta E_{zpe} > 0$ in all cases, inclusion of ZPE contributions results in a more endothermic CO_2−MOF interaction. Calculated ΔE_{TE} contributions are on average smaller (~1 kJ/mol) than those for ΔE_{zpe}, and in some cases (e.g., HKUST-1) are negative. (Because of the large unit cell of HKUST-1, phonon calculations were only attempted using the LDA, GGA, and DFT-D2 methods. ΔE_{zpe} and ΔE_{TE} values from the DFT-D2 calculation were then used to estimate these contributions for the other vdW functionals.)

Inspection of the data in Table 3.1 and Figure 3.1 (dashed columns) indicates that in all but one of the cases studied (PBE-GGA for Cu-HKUST-1) the summed effect of

ΔE_{zpe} and ΔE_{TE} is to shift MOF−CO_2 interactions to be more endothermic by about 2−4 kJ/mol. The small size and relative constancy of these contributions allow us to draw two conclusions: (1) Differences in accuracy between the different vdW functionals arise primarily from differences in static binding energies, ΔE, with vibrational contributions being less important. (2) In systems having large unit cells, one may approximate the room temperature enthalpy of adsorption ΔH by adding an endothermic shift of ~3 kJ/mol to the static binding energy (ΔE) calculated using the revPBE-vdW method. Prior calculations using the DFT-D2 method in conjunction with the B3LYP functional found values of 2.1 and 1.6 kJ/mol for ΔE_{zpe} and ΔE_{TE}, respectively, in Mg/DOBDC.[139,150] Comparable values of 2.0 (ΔE_{zpe}) and 1.4 kJ/mol (ΔE_{TE}) were also reported for Ni/DOBDC.

3.3.6 Structures

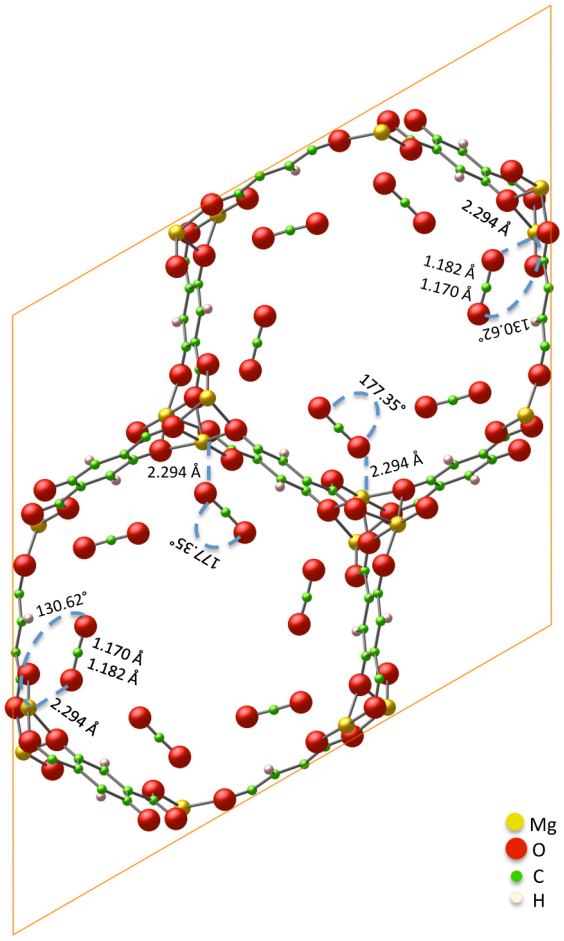

Figure 3.2 Optimized Structure for CO2 adsorbed on Mg/DOBDC as calculated using the optB86b-vdW functional.

Table 3.3 Comparison of Calculated Bond Length (Å) and Angles (°) for CO2-Containing MOFs with Experimental Data[a]

		M···O					
System	Method	Value	% error	MO-C	C-O	∠M-O-C	∠O-C-O
Mg/DOBDC	LDA	2.184	-4.73	1.175	1.162	129.20	176.12
	GGA	2.374	3.56	1.180	1.171	133.16	178.19
	DFT-D2	2.311	0.81	1.181	1.170	130.28	177.04
	optB86b-vdW	2.294	0.07	1.182	1.170	130.62	177.35
	optB88-vdW	2.288	-0.20	1.180	1.168	130.94	177.37
	optPBE-vdW	2.330	1.64	1.183	1.171	130.62	177.88
	revPBE-vdW	2.392	4.34	1.184	1.174	130.95	178.35
	rPW86-vdW	2.336	1.90	1.183	1.171	130.62	177.88
	Experiments[61]	2.283 (0.64)		1.119	1.122	122.78	160.50
	Experiments[162]	2.302 (0.89)		1.062	1.173	129.60	172.09
Ni/DOBDC	GGA	2.471	7.90	1.18	1.173	127.09	178.86
	DFT-D2	2.361	3.10	1.182	1.172	122.36	178.14
	optB86b-vdW	2.326	1.57	1.183	1.171	121.27	178.27
	optB88-vdW	2.340	2.18	1.181	1.170	121.53	178.26
	optPBE-vdW	2.426	5.94	1.183	1.173	120.84	178.66
	revPBE-vdW	2.617	14.28	1.183	1.176	120.29	179.02
	rPW86-vdW	2.470	7.86	1.183	1.173	121.29	178.61
	Experiments[155]	2.29		1.21	1.21	117.00	162.00
Co/DOBDC	LDA	2.274		1.176	1.164	118.02	177.63
	GGA	2.665		1.179	1.174	126.09	179.12
	DFT-D2	2.594		1.181	1.173	116.78	178.29
	optB86b-vdW	2.513		1.182	1.173	118.06	178.43
	optB88-vdW	2.522		1.180	1.171	117.68	178.38
	optPBE-vdW	2.618		1.182	1.175	117.03	178.78
	revPBE-vdW	2.812		1.183	1.177	115.95	179.05
	rPW86-vdW	2.635		1.182	1.174	116.89	178.68
CU/HKUST-1	LDA	2.330	-4.51	1.174	1.163	108.08	178.74
	GGA	2.633	7.91	1.181	1.172	108.37	179.02
	DFT-D2	2.637	8.07	1.181	1.172	108.30	179.03
	optB86b-vdW	2.562	5.00	1.181	1.172	108.44	179.15
	optPBE-vdW	2.635	7.99	1.182	1.173	108.78	180.00
	revPBE-vdW	2.771	13.57	1.184	1.176	106.55	180.00
	rPW86-vdW	2.684	10.00	1.182	1.173	107.83	179.22
	Experiments[61]	2.440 (1.07)		1.322	1.396	114.45	158.04

[a] M···O refers to the bond length between the metal atom and closest oxygen atom in adsorbed CO_2; C-O refers to the bond length between C and O in CO_2 involving the oxygen farthest from the MOF metal site; MO-C is the distance between C and O in CO_2 involving the O atom closest to the metal site; ∠O-C-O is the angle formed by the atoms in a CO_2 molecules; and ∠M-O-C is the angle formed between the metal site its neighboring oxygen in CO_2, and C in CO_2. The experimental data at 20 K except for Ni, which is at 100K. Where available, the experimental occupancy of CO_2 per metal site is given in parentheses.

In addition to comparing adsorption thermodynamics across these systems, it is also instructive to characterize how their equilibrium geometries differ as a function of the energy functional employed. A typical optimized geometry for CO_2 adsorbed in

Mg/DOBDC (obtained with the optB86b-vdW functional) is shown in Figure 3.2. Qualitatively similar geometries were obtained across all of the functionals examined in this study. For example, we find that CO_2 binds to the metal site in an end-on fashion through one O atom irrespective of the specific MOF examined or functional used. DFT studies by Wu et al.[61] and Valenzano et al.[150] also revealed similar binding geometries for CO_2 to the metal site in Mg/DOBDC and HKUST-1.Calculated bond lengths and bond angles are compared to experimental data for the Mg-, Ni-, and Cu-based MOFs from neutron[61,162] (for Mg/DOBDC and HKUST-1) and X-ray diffraction[155] (for Ni/DOBDC) experiments in Table 3.3. (To our knowledge, experimental structure data for Co/DOBDC have not been reported.) Tabulated properties include three bond lengths and two bond angles, where M···O refers to the bond length between the metal atom and closest oxygen in the adsorbed CO_2; C−O refers to the bond length between C and O in CO_2 involving the O farthest from the MOF metal site; MO−C is the distance between C and O in CO_2 involving the O closest to the metal site; ∠O−C−O is the angle formed by the O−C−O atoms within CO ; and ∠M−O−C is the angle 2 formed between the MOF metal site, its nearest-neighbor O (from CO_2), and the C atom within CO_2. For the LDA and GGA functionals, the predicted metal− oxygen bond lengths M···O follow the trends observed for the static binding energies. That is, the overbound LDA adsorption energies ΔE_{LDA} result in shorter M···O bond lengths (~ −4%) relative to the experimental data, while the underbound PBE energies yield M···O values that are too large (3−8%). This behavior is consistent with the notion that stronger CO_2−MOF interactions should result in shorter M···O distances. In contrast, for the six vdW-based functionals, there is no clear relationship between interaction strength and M···O distance. In fact, all of the

vdW-based methods overpredict the experimental M···O bond length to varying degrees. Best agreement with the experimental data is achieved for the optB86b-vdW and optB88-vdW functionals (0.1−5% error), which generally overpredict the enthalpy of CO_2 adsorption. On the other extreme, revPBE-vdW and rPW86-vdW yield the largest errors in bond length (1.9−14.3%), despite having the best agreement with experimental enthalpies. Predicted M···O bond lengths for optPBE-vdW and DFT-D2 fall between these two groups (0.8−8%). In an earlier study, Valenzano et al.74 calculated a M···O distance of 2.31 Å in Mg/DOBDC using the B3LYP+D* method. This is identical to our DFT-D2 value.

The effect of CO_2 loading upon the metal−oxygen length was examined for Mg/DOBDC using the revPBE-vdW, and a weak dependence was observed: M···O grows from 2.367 to 2.392 Å as the loading increases from 1/6 CO_2/Mg to 1 CO_2/ Mg. On the other hand, experiments by Queen *et al.*[162] also found a small change in M···O (~0.09 Å, for coverage between 0.24 and 0.89 CO2/metal); however, in this case, M···O contracts rather expands.

Regarding bond angles, we find that across all eight functionals the computed metal−O−C angles ∠M−O−C are overestimated as compared to experimental data by ~18° and ~3°, respectively, in Mg/DOBDC and Ni/DOBDC, and underestimated by ~6−7° in HKUST-1. An earlier study reported similar values in Mg/DOBDC.[150] The calculated deviation of adsorbed CO_2 from its linear geometry ∠O−C−O is relatively small, ~2−4°, and is largely independent of the functional or choice of MOF. Our ∠O−C−O angles are similar to the DFT values reported by Wu *et al.*[61]: 175.0° (LDA) and 178.0° (GGA) for Mg/DOBDC and 178.7° (LDA) and 179.0° (GGA) for HKUST-1. These computational

predictions differ significantly from the experimental ∠O−C−O bond angle of approximately (~160°). Wu *et al.*[61] suggested that the disagreement could arise from the thermal excitation of low energy CO_2 rotational modes about the metal with a span ±10°. Such rotations would increase uncertainties in the measurement of ∠O−C−O and ∠M−O−C.

We next turn to the C−O bond lengths within the adsorbed CO_2 molecule. In gas-phase CO_2, the C−O bond length is 1.161 Å.[161] Our calculations and experimental measurements find that in the adsorbed state these distances differ from those in free CO_2,[61,155] presumably due to interactions with the MOF metal site. In the case of experiments, the length of both C−O bonds varies inversely with ΔH, ranging from about 1.12 Å in Mg/DOBDC to more than 1.32 Å in HKUST-1. On the other hand, calculations predict these distances to be relatively independent of the MOF adsorbent, regardless of the functional used. With the exception of the Ni/DOBDC system, experiment and theory both predict the C−O bonds to be of unequal length. The calculated C−O bond lengths proximal to M are slightly elongated by ~0.01 Å with respect to the distal one in all DFT calculations. Consistent with our findings, prior DFT[61] and B3LYP+D*[150] calculations also predicted a slight (0.01−0.02 Å) elongation of the C−O bond nearest the metal site. This result differs somewhat from the experimental measurements, which find a slight contraction of this bond length (relative to the C−O bond distal to M) in Mg/DOBDC and HKUST-1.

Regarding structural trends across the MOFs, our calculations predict a rough increase in bond length M···O and a gradual expansion in CO_2 bond angle ∠O−C−O starting from Mg/DOBDC and progressing to Ni and Co/DOBDC, and to Cu in HKUST-

1. This trend follows the decreasing strength of interaction between the MOF and CO_2. Overall, we find that the optB86b-vdW functional yields the best agreement with the experimental geometries. On the other hand, the revPBE-vdW functional, which was the most successful at reproducing adsorption enthalpies, exhibits the largest errors in structural properties among the functionals benchmarked here.

4. Conclusions

Accurate computational methods are needed to predict the capacity, selectivity, and efficiency of porous materials for applications in gas capture and storage. Unfortunately, the most efficient and widely used method for calculating molecule−surface interactions, density functional theory, does not include long-range van der Waals interactions. These interactions are crucial for predicting thermodynamic properties in materials envisioned for carbon capture applications.

Toward the goal of identifying efficient computational schemes capable of predicting the performance of MOF- based adsorbents, in this study we have benchmarked six van der Waals density functionals (DFT-D2 and vdW-DF) with respect to experimental enthalpies for CO_2 adsorption in four prototype metal organic frameworks: M/DOBDC (M = Mg, Ni, Co) and Cu-HKUST-1. Prior studies have identified these systems as promising materials due to their unsaturated metal sites.

Regarding the conventional LDA and GGA functionals, we find that these methods only partially capture thermodynamic trends. Furthermore, they significantly overbind (LDA) and underbind (GGA) CO_2 with respect to the experimental enthalpies. The addition of a semi-empirical r^{-6} dispersion term to the GGA exchange-correlation

energy using "off the shelf" DFT-D2 parameters results in a substantial improvement in both the magnitude of the adsorption enthalpies and the ability to capture trends across systems. However, on average this approach still underbinds CO_2 as compared to the experimental data by ~7 kJ/mol (18%). Better accuracy is obtained with some of the non-empirical vdW density functionals, with the revPBE-based functional of Dion *et al.*[102] yielding an average error of only ~2 kJ/mol (4%) relative to experiment. This improvement in energetics is accompanied by a slight decrease in the accuracy of predicted structures, as the revPBE overestimates the metal−CO_2 bond length by about 10%.

Regarding the generality of our results, we note that the present study is restricted to CO_2 adsorption in MOFs having coordinatively unsaturated metal sites. Nevertheless, the systems considered exhibit two different coordination geometries for the metal sites, and have ion identities spanning the alkaline earth metals (Mg), as well as transition metals having partial (Ni, Co) and full *d* shells (Cu). Consequently, our results appear to be independent of the choice of metal ion. Further study is needed to examine the performance of these functionals for adsorption of other molecules across the broader class of MOF compounds. In this regard, the availability of high-quality experimental data is also essential.

The efficiency and accuracy of the revPBE-vdW functional suggests that density functional methods are viable for rapid screening of potential CO_2 adsorbents. The ability of such an approach to address the large, periodic unit cells typical of MOFs offers advantages over expensive, cluster-based quantum-chemical methods.

Chapter 4

Thermodynamics of Carbon Capture in Metal Substituted M-MOF-74 and M-HKUST-1

4.1 Introduction

In the previous chapter, the ability to accurately predict its magnitude across a range of MOFs would be helpful in screening for optimal CCS compounds. Several van der Waals density functionals (vdW-DFs) were benchmarked against experimental adsorption enthalpies in 4 CUS-containing MOFs: Mg-[60], Ni-[147], Co-DOBDC[148] and Cu-HKUST-1.[69] Comparisons were made between conventional LDA[160] and GGA[89] functionals (with no dispersion interaction), the semi-empirical DFT-D2[100], and vdW-DF's with five distinct GGA-based exchange functionals: revPBE[102], optB86[110,111], optB88[111], optPBE[110,111], and rPW86.[112] The calculations revealed that the revPBE-vdW functional produced very good agreement with the average experimental enthalpies, with an error of ~2 kJ/mol, suggesting that thermodynamic screening based on vdW-DF's is computationally feasible, even for MOFs with large unit cells (e.g., HKUST-1).

Towards the goal of identifying thermodynamically-optimal MOFs for CCS applications, in this chapter we computationally screen 36 metal-substituted variants of M-DOBDC and M-HKUST-1 (M = Be, Mg, Ca, Sr, Sc, Ti, V, Cr, Mn, Fe, Co, Ni, Cu,

Zn, Mo, W, Sn, and Pb) with respect to their CO_2 adsorption enthalpy, $\Delta H^{T=300K}$. Supercell calculations based on the revPBE-vdW functional yield enthalpies in good agreement with experimental measurements, out-performing semi-empirical (DFT-D2) and conventional (LDA & GGA) functionals. Our screening identifies 13 compounds having ΔH values within the targeted thermodynamic window $-40 \leq \Delta H \leq -75$ kJ/mol: 8 are based on M-DODBC (M=Mg, Ca, Sr, Sc, Ti, V, Mo, and W), and 5 on M-HKUST-1 (M= Be, Mg, Ca, Sr and Sc). Variations in the electronic structure and the geometry of the structural building unit are examined and used to rationalize trends in CO_2 affinity. In particular, the partial charge on the coordinatively unsaturated metal sites correlates with ΔH, suggesting that this property may be used as a simple performance descriptor. The ability to rapidly distinguish promising MOFs from those that are "thermodynamic dead-ends" will be helpful in guiding synthesis efforts towards promising compounds. [15]

4.2 Summary of Methods

Thermodynamic screening of CO_2 adsorption enthalpies across metal-substituted variants of M-DOBDC and M-HKUST-1 was performed using van der Waals-augmented density functional theory (DFT[86], VASP[113,114] code). Crystal structures for empty[69,147] and CO_2-containing[61,155] Ni-DOBDC and Cu-HKUST-1 were adopted from diffraction experiments and were used as initial models for metal-substituted versions in which the metal component (M) was selected from elements which have the potential to exhibit a +2 oxidation state. These include: four alkaline earths: Be, Mg, Ca, Sr; 11 transition metals: Sc, Ti, V, Cr, Mn, Fe, Co, Ni, Cu, Zn, Mo, W, and two group-14 metals: Sn, Pb.

The computational cells used for M-DOBDC and M-HKUST-1 contain, respectively, 54 and 156 atoms; 6 and 12 CO_2 molecules were added to these supercells to represent the adsorbed state, corresponding to a coverage of one CO_2 per CUS. For M-DOBDC, the symmetry for both empty and CO_2-containing supercells adopts the $R\bar{3}$ space group, as found in experiments[147]. In the case of M-HKUST-1, CO_2 adsorption at CUS sites can occur in one of four symmetry-equivalent positions, (each having a CO_2 occupancy of 25%,) which differ by a 90° rotation about an axis connecting the two metal sites within an SBU[61]. To account for the fractional occupancy, M-HKUST-1 supercells were constructed such that the CO_2 molecules occupy one of the 4 possible adsorption sites in a quasi-random fashion: the two CO_2 molecules adsorbed on opposite sides of an SBU were positioned in a *trans* configuration (see Fig. S1 in the Supporting Information) to maximize the CO_2-CO_2 separation, and this *trans* configuration was varied from SBU to SBU throughout the cell. Consequently, supercells containing adsorbed CO_2 have a slightly lower symmetry [$Fm\bar{3}$ (#202)] than those without [$Fm\bar{3}m$ (#225)].

4.3 Results

4.3.1 Structures

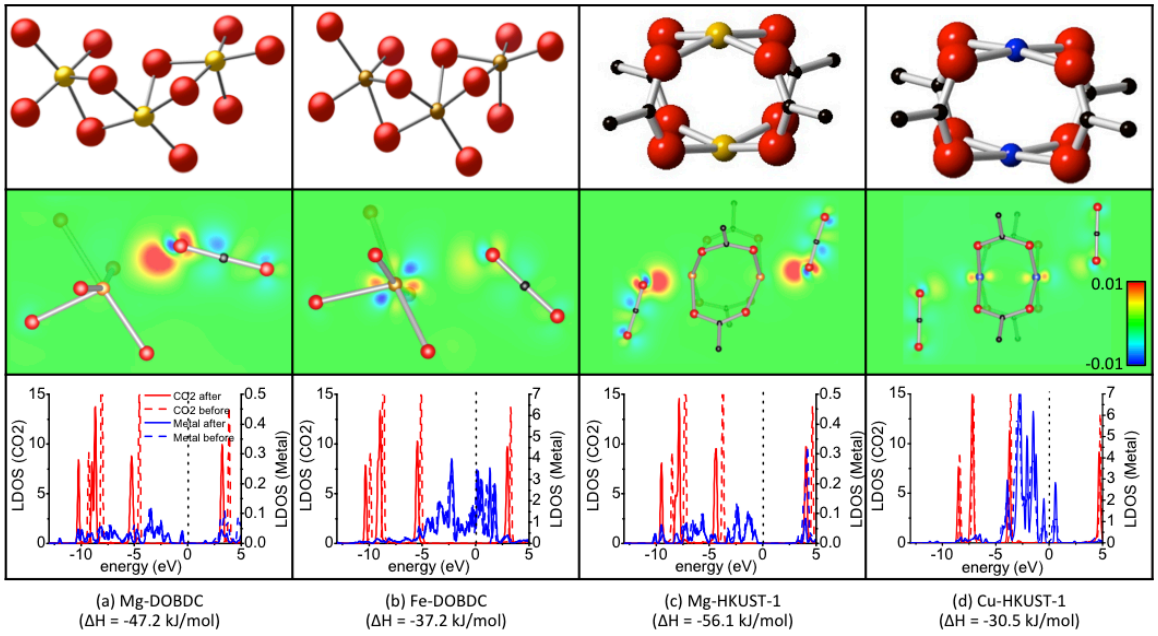

Figure 4.1 Local geometry (top row), charge density difference (middle), and local DOS (LDOS, bottom) for four representative MOFs in the vicinity of the SBU. From left to right: Mg-DOBDC, Fe-DOBDC, Mg-HKUST-1, and Cu-HKUST-1. C = black; O = red; Mg = yellow; Fe = dark yellow; Cu = blue. For clarity, in the case of DOBDC only a portion of the infinite SBU is shown in the top row, while for the charge density difference (units of electrons/Å^3) only the metal and its nearest neighbors are shown. For the LDOS plot solid lines refer to the adsorbed state, and dashed lines refer to isolated CO_2 and MOF.

While isostructural variants of DOBDC and HKUST-1 have been reported for several metal compositions[60,64-67,69-74,147,148], it is unclear if variants beyond those currently known are possible. Here we examine the relaxed structure of the SBU as a qualitative indicator of whether a given isostructural variant is plausible. Figures B.2 and B.3 depict the local coordination of the CUS in M-DOBDC and HKUST-1 as a function of the substituted metal, based on relaxations with the revPBE-vdW functional.

(Optimized cell geometry data appears in Table B.1; metal-oxygen bonding distances are given in Tables B.2 and B.3.) Each structure is classified according to a "red/yellow/green" color scheme based on the extent to which the relaxed structure resembles its respective prototype structure, Ni-DOBDC or Cu-HKUST-1. Structures labeled "green" exhibit geometries that are very similar to the prototype, indicating that isomorphism may be possible. On the other hand, "red" structures exhibit large structural distortions, such as a change in the coordination number of the CUS. We expect that these compounds are much less likely to exhibit isomorphism. Finally, "yellow" compounds fall between these extremes, and refer to systems in which there are moderate structural deviations (e.g., changes in bond length) from the prototype.

In the case of M-DOBDC, 13 of the 18 candidate structures (excluding Be, Cr, Cu, Sn and Pb) exhibit only minor changes to the SBU geometry, and therefore fall within the green category. These compounds maintain the square-pyramidal coordination of the CUS to its nearest-neighbor oxygen atoms. Moreover, bond lengths for the five M-O bonds follow trends similar to those observed in the Ni-DOBDC prototype (Table B.2). The variant containing substituted Pb falls within the yellow category as it exhibits a slightly distorted structure with a much wider range of M-O distances of 2.328 – 2.696 Å (Table B.2). Finally, structures containing Be, Cr, Cu and Sn fall within the red category because their geometries contain CUS with a coordination number of four. In particular, Be adopts a tetrahedral coordination and becomes "buried" inside the MOF structure. This behavior appears to arise from the small ionic radius of the Be^{+2} ion. In this geometry Be is no longer accessible to guest molecules, explaining the relatively low adsorption enthalpy observed in this compound (see below). In contrast to Be, the other

three metals – Cr, Cu, and Sn – exhibit geometries in which the CUS protrudes from the framework, resulting in a change from square-pyramidal-like coordination to square-planar-like with four metal-oxygen bonds.

Structures for the relaxed SBUs in M-HKUST-1 generally exhibit less distortion than in M-DOBDC. In all cases metal substitution preserves the paddle-wheel geometry (Fig. B.3), with the main difference between variants being the position of the metal with respect to the 4-fold oxygen plane. The largest distortions occur for Ca, Sr, Sn and Pb, which we classify as yellow. Metal substitution in these cases results in a large protrusion of the metal out of the oxygen plane, accompanied by an enlargement of the M-M distance (Table B.3). The protrusion appears to arise from a size effect related to the large ionic radii of these metals (Table. B.4). No M-HKUST-1 structures are classified as red.

Considering the smaller number of red structures in the M-HKUST-1 series, it appears that this compound is more amenable to isostructural metal substitution than the M-DOBDC series. In general, the bonds between the CUS and nearest neighbor framework oxygen are slightly smaller in HKUST-1 than in DOBDC; this trend is consistent with the higher coordination of metal sites in DOBDC (5-coordinated, square pyramidal) vs. HKUST-1 (4-coordinated, square planar).

Table B.5 summarizes the structural properties of the CO_2-adsorbed state for both MOFs. In the case of M-DOBDC, CO_2 adsorption does not induce significant changes to the structure of the MOF regardless of the identity of the CUS metal. Distances between the metal and the nearest oxygen in CO_2 vary from a minimum of 2.34 Å in V-DOBDC to a maximum of 4.07 Å in Sn-DOBDC, with shorter bond lengths correlating with larger adsorption enthalpies (Table 4.1), a trend which has also been observed by others.[64]

Adsorbed CO_2 exhibits a slight lengthening of the C-O bond closest to the metal in all versions of M-DOBDC, while the distal C-O bond slightly shrinks. (The revPBE-vdW C-O bond length in an isolated CO_2 molecule is 1.179 Å.) A small (0-3°) deviation from the linear O-C-O bond angle is also observed.

The existence of four symmetry-equivalent adsorption geometries per metal site in M-HKUST-1[61] results in the possibility for shearing of the paddle-wheel SBU upon adsorption of CO_2 (see Fig. 1c for an example involving Mg-HKUST-1). This effect is most pronounced when the two adsorbed CO_2 molecules bonded to an given SBU are oriented in a *trans* configuration, and for cases where the metal-CO_2 interaction is strongest (i.e., Mg, Ca, Sr and Sc, see below). Shearing could be expected if adsorbed CO_2 cannot easily hop between the four sites. We find this is indeed the case, as a rotational energy barrier ($E_a > k_BT$) arising from steric hindrance with the nearby linker prevents easy transitions between adsorption sites. The contribution of shearing relaxations to the CO_2 adsorption energy was estimated by comparing to simulations in which these relaxations were forbidden. We find that shearing can lower binding energies (i.e., more exothermic) by up to 3-6 kJ/mol for M = Ca and Sr.

Regarding the geometry of metal-CO_2 interactions, M-O bond distances in M-HKUST-1 are generally smaller than in M-DOBDC, ranging from 1.95 Å in Be-HKUST-1 to 3.84 Å in Pb-HKUST-1. Adsorbed CO_2 generally exhibits a more linear geometry in M-HKUST-1, suggestive of slightly weaker bonding interactions with the MOF; other features of the CO_2 structure follow trends similar to those observed in M-DOBDC. (An exception is Sc-HKUST-1, in which the bending angle of CO_2 is 140.8º.)

As previously described, the metal ions in the relaxed Cr, Cu, and Sn-based DOBDC variants adopt distorted square-planar-like geometries, and it is natural to ask whether these compounds locally resemble the analogous HKUST-1 geometries and possess similar binding energies for CO_2. Indeed, in both Cu/Sn-DOBDC and Cu/Sn-HKUST-1 comparable binding energies (Table B.6) are found (see Figure B.2, B.3 and Table B.2, B.3). While in the case of Cr-DOBDC and Cr-HKUST-1 both compounds exhibit similar square-planar geometries and M-O distances, however, the slight submersion of Cr below the square pyramid plane in Cr-HKUST-1 makes it less accessible and results in weaker binding with CO_2

4.3.2 Thermodynamics

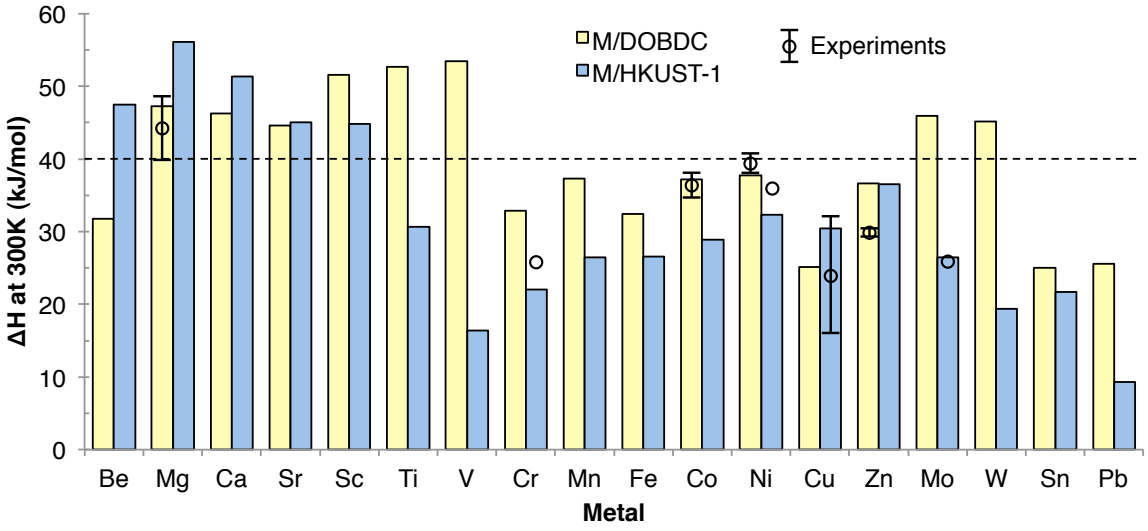

Figure 4.2 Adsorption enthalpies for metal substituted variants of DOBDC and HKUST-1 calculated with the revPEB-vdW functional. Data points and error bars refer, respectively, to the average and range of reported experimental enthalpies. The dashed line is the lower limit of the optimal enthalpy range for CO_2 capture (-40 kJ/mol).[15]

Table 4.1 Calculated adsorption enthalpies (kJ/mol CO_2), metal-oxygen bond lengths (Å) (involving the nearest oxygen atom in CO_2), and metal charge (REPEAT method[171]) for metal substituted-variants of DOBDC and HKUST-1.

Metal	M-O (Å)	Metal Charge	ΔH (kJ/mol) DFT-D2	rPBE-vdW	Experiments
			M-DOBDC		
Be	4.049	1.248	-15.6	-31.8	
Mg	2.392	1.556	-38.5	-47.2	-44.2±4.6[60,150-154]
Ca	2.623	1.487	-36.1	-46.3	
Sr	2.842	1.460	-30.4	-44.6	
Sc	2.406	1.553	-41.8	-51.5	
Ti	2.394	1.738	-47.9	-52.7	
V	2.276	1.520	-52.2	-53.5	
Cr	3.286	1.082	-17.4	-32.9	
Mn	2.695	1.191	-28.9	-37.3	
Fe	2.717	1.309	-23.6	-32.4	
Co	2.812	1.099	-28.9	-37.2	-35.7±1.9[60,154]
Ni	2.617	1.173	-29.3	-37.7	-39.6±1.5[60,154,155]
Cu	3.228	0.866	-15.6	-25.1	
Zn	2.867	1.217	-29.5	-36.6	30.5+0.5[139,172]
Mo	2.528	1.377	-47.3	-45.9	
W	2.450	1.140	-41.6	-45.1	
Sn	4.007	0.176	-14.2	-25.1	
Pb	4.977	0.782	-9.4	-25.6	
			M-HKUST-1		
Be	1.945	1.367	-41.3	-47.5	
Mg	2.221	1.574	-47.0	-56.1	
Ca	2.624	1.527	-50.1	-51.3	
Sr	2.861	1.482	-45.9	-45.1	
Sc	2.096	1.270	-43.6	-44.8	
Ti	2.686	1.285	-30.9	-30.6	
V	2.772	1.014	-23.4	-16.4	
Cr	3.149	1.232	-20.4	-22.1	-26.7[75]
Mn	3.106	1.036	-20.9	-26.4	
Fe	3.282	0.992	-12.0	-26.5	
Co	2.584	1.149	-22.2	-28.9	
Ni	2.731	1.041	-23.6	-32.3	-36. 8[75]
Cu	2.769	0.940	-17.8	-30.5	-23.7±8.2[75,157,158,173]
Zn	2.384	1.236	-34.4	-36.6	
Mo	3.340	1.237	-17.5	-26.4	-25. 6[75]
W	3.127	1.270	-15.9	-19.4	
Sn	3.811	0.270	-14.1	-21.7	
Pb	3.840	0.591	-5.1	-9.3	

Calculated enthalpies for CO_2 adsorption at 300 K are tabulated in Table 4.1 and summarized graphically in Fig. 4.2. A complete compilation of thermodynamic data (calculated using the LDA[160], PBE-GGA[89], semi-empirical DFT-D2[100] and revPBE-vdW[102]) across all 36 metal substituted MOFs is given in Table B.6. For comparison, experimental adsorption enthalpies from the literature are also included in Table 4.1 and Fig. 4.2. In the case of Mg, Ni, Co, Zn-DOBDC and Cu-HKUST-1, several experimental measurements have been performed by different groups yielding a relatively robust estimate of thermodynamic properties of these compounds. Experimental data has also recently been reported for Cr, Ni and Mo-HKUST-1, however only one measurement has been performed for each of these cases. Consistent with prior studies[174], we find LDA and GGA yield rather poor agreement with experimental adsorption enthalpies: the omission of vdW interactions in these methods results in significant under- (GGA) and over-estimation (LDA) of the experimental adsorption enthalpies.

The inclusion of dispersion interactions in DFT-D2 and the revPBE-vdW functionals significantly improves the accuracy of the predicted binding energies. In the case of ΔH, the revPBE-vdW exhibits better agreement with experimental data than the DFT-D2 functional: The average error of revPBE-vdW compared to experiments, 3.6 kJ/mol, is approximately half that for DFT-D2, 7.1kJ/mol, consistent with our prior benchmarking of these methods.[174] Trends in binding energies across the metals within each MOF prototype are largely captured in each of the PBE-GGA, DFT-D2, and revPBE-vdW functionals; this implies that the degree of dispersion interaction is proportional to the respective PBE-GGA binding energy.

According to a recent report,[15] optimal adsorbents for post-combustion or direct-air carbon capture will exhibit adsorption enthalpies between 40 – 75 kJ/mol. While the targeted range of ΔH is based on considerations related to regeneration efficiency, other authors have suggested[12] that CO_2 capacity may also scale with ΔH, suggesting that enthalpies towards the higher end of this range may be desirable. Excluding compounds having large structural distortions (i.e., "red" compounds), inspection of the calculated enthalpies in Table 1 reveals that eight variants of M-DOBDC (M = Mg, Ca, Sr , Sc, Ti, V, Mo, and W) and five variants of M-HKUST-1 (M = Be, Mg, Ca, Sr, and Sc) fall within the targeted thermodynamic window. Of these, [Sr, Mo, W]-DOBDC and all five M-HKUST-1 variants have to our knowledge not been previously identified as promising materials; they therefore represent targets of interest for experimental synthesis and testing. More generally, with the exception of Be-DOBDC (for reasons previously described), substitutions involving alkaline earth metals show promise. While other properties of these materials will certainly be important in assessing their viability in carbon capture applications (e.g., cost, selectivity, robustness to water vapor and other reactive flue gas species, *etc.*), the efficient computational identification of those compounds which hold promise from those which are "thermodynamic dead ends" is clearly of value.

Our predicted energetics qualitatively agree with those of Park *et al*.[64] who calculated the static binding energy (ΔE) for CO_2 on a subset of M-DOBDC compounds using the semi-empirical DFT-D2 method. The trends predicted by both methods are similar; nevertheless, the agreement with experimental data is significantly better with vdW-DF as DFT-D2 tends to systematically under-predict binding energies, a feature

which was observed in our prior study.[174] The good agreement with experimental data combined with the modest computational cost – vdW-DF calculations are only ~50% more expensive than a conventional GGA calculation – suggests that the vdW-DF method is well suited for efficient characterization of CO_2 capture in MOFs.

Incidentally, those MOFs that were identified as less likely to exhibit isomorphism exhibit amongst the smallest CO_2 adsorption enthalpies. For example, in M-DOBDC Sn and Cu exhibit enthalpies of only ~25 kJ/mol, and are followed closely by Pb and Be. Similarly, in M-HKUST-1, Pb and Sn fall near the bottom of the range of calculated enthalpies (9.3 and 21.7 kJ/mol, respectively).

4.3.3 Electronic Structure

Figure 4.1 compares the local geometry near the CUS metal (after CO_2 adsorption), charge density difference, and local density of states (LDOS) for four MOFs whose behavior spans the range of properties observed in the screened compounds. For M-DOBDC we illustrate the cases M = Mg and Fe. Both of these compounds have been synthesized,[60,66] but the performance of only Mg-DODBC has been tested with regard to CO_2 uptake. Mg-DOBDC exhibits a strong CO_2 affinity, -47.2 kJ/mol (Table 2.1), whereas the interaction between CO_2 and Fe-DOBDC falls on the weaker end of the scale, -32.4 kJ/mol. These thermodynamic trends are reflected in the degree of charge redistribution in these compounds (Fig. 4.1, middle panels): in Mg-DOBDC there is a large accumulation of charge (+0.011 *e*-/Å^3) on the CO_2 oxygen closest to the CUS metal. This is accompanied by charge depletion on the C and O (in CO_2) farthest from the CUS. These features confirm that the Mg CUS in DOBDC induces a large polarization of the

CO_2 molecule, consistent with the large calculated adsorption enthalpy. This behavior should be contrasted with the charge density of the more weakly bound Fe-DOBDC, which shows a much smaller polarization of CO_2 and a maximum charge accumulation (0.004 *e*-/Å^3) that is nearly three times smaller than that for Mg-DOBDC.

These data are consistent with previous studies[61,64] that have argued that strong electrostatic interactions between CUS cations and the CO_2 quadrupole constitute the main MOF/CO_2 interaction. These interactions result in polarization and a slight bending of the CO_2 molecule. In addition, Park et al.[64] also suggested a forward donation of loan-pair electrons in CO_2 to metal occurs in M-DOBDC compounds with M = Ti, V. Such an interaction would strengthen the CO_2 attraction at these metal sites, resulting in higher adsorption energies.

Turning to M-HKUST-1, Fig. 4.1 compares the cases having M = Mg and Cu. Mg-HKUST-1 is a hypothetical MOF that our calculations predict as having the largest CO_2 adsorption enthalpy within the M-HKUST-1 series, -56.1 kJ/mol (Table 2.1). On the other hand Cu-HKUST-1 is the well-known prototype for the HKUST-1 series; it has a moderate adsorption enthalpy of -30.5 kJ/mol. Similar to the two DOBDC cases described above, trends in charge density difference distributions for Mg and Cu-HKUST-1 largely follow the calculated binding energies. Adsorption on Mg-HKUST-1 results in a much stronger polarization of the CO_2 molecule, with a maximum charge density accumulation (0.016 *e*-/Å^3) on the nearest O atom that is more than five times greater than that observed in Cu-HKUST-1 (0.003 *e*-/Å^3).

Figure 4.1 (bottom panel) compares changes to the local density of states (LDOS) of both the CUS metals and CO_2 molecules before and after adsorption. In all cases there

is no significant change in metal DOS below Fermi level upon CO_2 adsorption. In contrast, the CO_2 states are uniformly shifted to lower energies upon adsorption. The magnitude of this shift follows closely the trends in adsorption energy, and is further supports the hypothesis that electrostatic effects constitute the primary bonding interaction. These results are in good agreement with the DFT-D2 data of Park *et al*.[64] Charge density difference and local density of states plots for all compounds examined in this study are provided in Figs. B.4 – B.9 in the Appendix.

In contrast to substitutions involving alkaline earths, where ΔH is relatively smaller for the M-DOBDC-based compounds, Fig. 4.2 shows that M-DOBDC compounds containing transition metals generally have adsorption enthalpies that are slightly larger than their corresponding M-HKUST-1 variants. Exceptional cases occur for M = Ti, V, Mo, and W, where the difference in ΔH between DOBDC and HKUST-1-based compounds is especially large, exceeding ~ 20 kJ/mol. These differences in affinity are also evident in the charge density difference plots (Figs. B.4 and B.5): there is significant accumulation of charge between the metal atom and CO_2 in the DOBDC-based compounds, whereas in HKUST-1 the accumulation is much smaller. The larger CO_2 affinity and charge accumulation associated with these four metals in DOBDC appears to arise from forward donation of electrons from the CO_2 HOMO (lone pair electrons) to partially occupied *d* states on the metal. The reason this donation is more facile in DOBDC than in HKUST-1 can be understood from the local density of states on the metal sites (Fig. B.10). In DOBDC the square-pyramidal coordination of the metals allows in some cases for significant state density near the Fermi level. The effect is most significant for Ti, V, Mo, and W; hence these states would be energetically well-suited to

accept donated electrons. In contrast, in HKUST-1 the LDOS for essentially all metals is negligible at the Fermi level. Finally, the increase in negative charge on Ti, V, Mo, and W following adsorption, and the simultaneous increase in positive charge on CO_2, (Table B.7) further suggests that these energetic differences can be traced to the efficacy of forward electron donation.

4.3.4 Trends

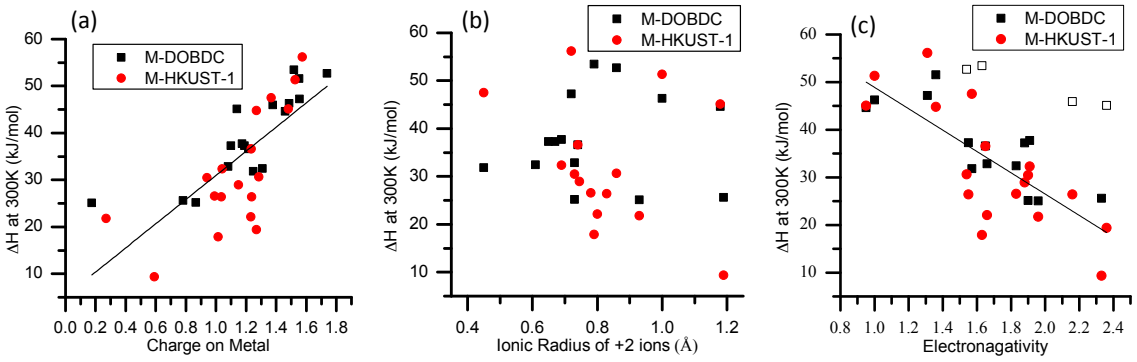

Figure 4.3 Correlation between calculated adsorption enthalpy and (a) partial charge on metal ions, (b) tabulated ionic radii of +2 metal ions, and (c) Pauling electronegativity.

Figure 4.2 shows that in two thirds of the possible compounds DOBDC-based structures have a higher affinity for CO_2 than those based on HKUST-1. A notable exception to this trend are the variants based on the alkaline earth metals (AEM). These trends can largely be explained by the accessibility and charge state of the CUS metal, as described below.

Figure 4.3 examines the correlation between adsorption enthalpy and the CUS metal's calculated oxidation state (a), ionic radius (b, Table B.4), and electronegativity. Values for the charges are summarized in Table 4.1. Larger charges on the metal are expected to enhance the electrostatic interaction between MOF and CO_2, resulting in

higher adsorption enthalpies. We find that the average metal partial charge in DOBDC of +1.22 is larger than the average of +1.14 in HKUST-1, in agreement with the stronger affinities generally observed in DOBDC-based compounds. As demonstrated in the figure 4.3(a), the magnitude of the metal charge correlates with the adsorption enthalpy, as could be expected given that electrostatic interactions are a significant portion of the MOF-CO_2 interaction. In particular, compounds having CUS partial charges larger than approximately 1.4 exhibit adsorption enthalpies within the desired window of $\Delta H > 45$ kJ/mol.[15] Such a correlation suggests that by calculating partial charges alone one could quickly identify MOFs with promising thermodynamics. Such an approach would represent a significant savings over full-scale adsorption calculations that require optimizing adsorption geometries.

In the case of alkaline earth metal (AEM) substitutions, M-HKUST-1 variants are predicted to have larger ΔH than the corresponding M-DOBDC variants. This behavior differs from the general trend mentioned above; nevertheless it still can be attributed to the magnitude of the charges on CUS cations, which are larger in M-HKUST-1 than in M-DOBDC in the case of AEM (Table 4.1). The absence of *d*-electrons in the AEM allows for relatively higher charge on the CUS in the four-fold-coordination environment of HKUST-1 vs. the five-fold-coordination of M-DOBDC. Additional attraction for CO_2 in AEM-HKUST-1 appears to arise from interactions with other atoms in the SBU, as suggested by the larger non-linearity of the O-C-O angle (Table B.5).

In addition to the charge on the metal, it has also been suggested[67] that metal ions having small ionic radii should strongly polarize guest molecules, resulting in a more exothermic adsorption enthalpy. Since ionic radii are tabulated quantities (Table B.4.), a

correlation between radii and CO_2 affinity could be easily exploited to direct synthesis efforts towards specific metals. Figure 4.3(b) plots calculated adsorption enthalpies vs. the tabulated ionic radius of the 2+ ions used in this study. The figure demonstrates that in these compounds there is no general correlation between ΔH and ionic radius. This behavior can be understood by noting that ionic radius will also impact the structure of the SBU. A good example is Be. As the element having the smallest ionic radius, one would expect that Be will have a strong polarization effect on CO_2, resulting in a large ΔH. While the expected behavior holds for Be-HKUST-1 (ΔH = -47.5 kJ/mol), Be-DOBDC has a low enthalpy of ΔH = -31.8 kJ/mol. This is due to size effects within the SBU: the small radius of Be ions results in a "burrowing" of the Be ion into the framework, where it adopts a tetrahedral coordination and is no longer readily accessible to adsorbed CO_2. While correlations between ΔH and radius could be expected across some subset of the examined compounds where the structure effects are small (for example, the trend holds for Mg, Ca, and Sr), in general the connection between CO_2 affinity and ionic radius of the CUS is complicated by changes to the MOF structure arising from ion size effects.

As the electrostatic interaction between the MOF's metal cations and adsorbed CO_2 molecules appears to comprise a significant fraction of the adsorption enthalpy, it is natural to ask whether the electronegativity of the metal correlates with ΔH. Presumably, those metals that are the least electronegative will exhibit the largest positive partial charges due to ionic interactions with the MOF ligands; in turn, the induced metal charge should result in stronger interactions with CO_2. Figure 4.3(c) plots the tabulated Pauling electronegativities of the metals vs. the calculated ΔH values. With the exception of Ti, V,

Mo, and W-DOBDC, for which forward donation constitutes a significant fraction of the bonding (shown as empty symbols in the figure), it is clear that a correlation exists between enthalpy and electronegativity. Such a correlation suggests that MOFs containing electropositive metal ions will have amongst the highest affinities for CO_2.

4.4 Conclusions

Van der Waals-augmented DFT has been used to screen 36 metal substituted variants of M-DOBDC and M-HKUST-1 (M = Be, Mg, Ca, Sr, Sc, Ti, V, Cr, Mn, Fe, Co, Ni, Cu, Zn, Mo, W, Sn, and Pb) with respect to their CO_2 adsorption enthalpy at T = 300K. The prototype compounds were selected based on their high capacities for CO_2, their potential for forming isostructural metal-substituted variants, and to examine the impact of their distinct metal cluster geometries (square-planar vs. square pyramidal). An analysis of the structure of the metal cluster was used to qualitatively assess the likelihood that a given substituted metal will adopt an isostructural geometry, and suggests that the M-HKUST-1 structure is more amenable to metal substitution than is M-DOBDC.

Consistent with our prior benchmarking, enthalpies calculated with the non-empirical revPBE-vdW functional are in good agreement with experimental measurements, and suggest that this functional is a reliable and efficient method for treating the large unit cells typical of MOFs. Electronic structure trends across the metals reveal that electrostatic interactions comprise a significant portion of the MOF-CO_2 bond, in agreement with several literature reports. These trends further suggest that the geometric accessibility and partial charge of the CUS metal correlates with the magnitude

of the adsorption enthalpy. Thus, the metal charge could be used as a simple descriptor to rapidly identify MOFs with targeted adsorption enthalpies without the need for expensive adsorption calculations. The dependence on the metal's charge state is further reflected in a correlation with the metal's electronegativity, suggesting that strongest affinities will be obtained for MOFs containing the most electropositive metals. On the other hand, due to structural effects the ionic radius of the CUS metal does not generally correlate with the adsorption enthalpy: extremely small and large ions alter the structure of the MOF, potentially limiting the accessibility of these ions to adsorbed CO_2.

Finally, our calculations identify several compounds having CO_2 affinities that fall within the targeted range of -40 to -75 kJ/mol. While other properties of the identified compounds need to be assessed (stability, selectivity, etc.), the ability to rapidly distinguish promising compounds from those that are "thermodynamic dead-ends" via computation will be of value in guiding synthesis efforts towards promising compounds.

Chapter 5

Methane Adsorption in M-DOBDC and Other MOFs Mined from the Cambridge Structure Database

5.1 Introduction

Now, we move on the methane storage of MOFS. While many features have been suggested to impact methane uptake in MOFs,[175,176] we note that essentially all of the high CH_4-capacity MOFs contain a combination of coordinatively unsaturated (metal) sites, CUS[68,152,177,178] and deep-well "pocket" sites. (Throughout this article we will collectively refer to both CUS and pocket sites as "enhanced binding sites," EBS.) It has been argued that CUS result in relatively strong CH_4—MOF binding through enhanced coulomb interactions,[62] while at the pocket sites comparable (or stronger) adsorption energies arise from enhanced Van der Waals interactions.[68] Experiments have confirmed that CUS and pocket sites act as primary adsorption sites for CH_4;[62,68,179,180] thus, high volumetric capacities could be expected if these sites could be arranged in a high-density fashion. In addition, substitution of the CUS metal has been shown to dramatically alter the uptake of other small molecules such as CO_2,[60] suggesting a pathway for performance tuning. Nevertheless, EBS can also result in high uptake at low pressure,[68] resulting in a tradeoff between high total capacities *vs.* reduced usable capacities during isothermal

pressure swing desorption. Finally, CUS consisting of heavy transition metals will increase the MOF mass, and thereby reduce the gravimetric storage density.

In light of the potential tradeoffs associated with enhanced binding sites, in this study we examine the extent to which metal substitution at CUS impacts the thermodynamics and capacity for CH_4 adsorption in the prototype MOF, M-DOBDC. Experiments by Wu *et al*.[68] reported methane uptake in five metal-substituted M-DOBDC variants, M = Mg, Mn, Co, Ni, and Zn, with high excess capacities ranging from 149 to 190 cm^3/cm^3. These measurements identified the CUS as the primary CH_4 adsorption site, with unusually large adsorption enthalpies approaching 20 kJ/mol. A recent re-evaluation of these capacities found that Ni-DOBDC exhibits the highest total volumetric capacity for CH_4 of any experimentally-tested MOF (228 cm^3/cm^3, at 298 K and 35 bar).[27]

In the present study we extend the composition range of the CUS by considering 18 metal-substituted variants of M-DOBDC. In previous chapter, on the thermodynamic screening of M-DOBDC compounds demonstrated that some of these MOFs are promising for CO_2 capture, with predicted adsorption enthalpies (ΔH) falling within the desired thermodynamic window -40 to -75 kJ/mol.[15] Taken together, these factors motivate us to consider the M-DOBDC series as candidate methane storage materials. To this end, a combination of van der Waals-augmented density functional theory[86] (vdW-DFT) and semi-empirical grand canonical Monte Carlo calculations are used to predict the thermodynamics and capacities for CH_4 uptake in the M-DOBDC series. In addition, we re-visit the predicted capacities in other prominent MOFs, including, MOF-5, PCN-11, PCN-14, and HKUST-1. Our hope – and the emerging trend[51] – is for computation to

accelerate the search for promising methane adsorbents. Consequently, a portion of our study is devoted to assessing the accuracy of these methods by validating the predicted adsorption enthalpies and capacities with experimental data. These comparisons are timely because van der Waals Density Functionals are rapidly evolving[100,102,181], and typical classical interatomic potentials do not always capture interactions with CUS[62,182]. Such comparisons provide an important benchmark as the field of CH_4 storage continues to grow.

Regarding the energetics of CH_4 adsorption, accurate thermodynamic data are important because these properties strongly impact the thermal behavior of a MOF-based methane storage system. An ANG system will release heat during uptake, and potentially require heat input to bring about maximum desorption. Managing this heat exchange process will influence the efficiency, design, and cost of the storage device. Other factors being equal, a desirable methane adsorbent will have both a high capacity and a small enthalpy of adsorption.

Recent reports have shown that vdW-DF[102,112] can yield accurate estimates of the enthalpy of adsorption (ΔH) for H_2 and CO_2 in MOFs.[64,81,146,174] In the case of CO_2, the mean absolute deviation (MAD) between the calculated vdW-DF1[102] and experimental ΔH across several metal substituted MOFs was only 3.4 kJ/mol.[174,183] A natural question is whether comparable accuracy can be attained for methane adsorption. In the present study we find that the rPW86-based vdW-DF2[112] method outperforms conventional (PBE-GGA[184]), semi-empirical (DFT-D2),[100] and other vdW-based density functionals in predicting ΔH for CH_4. Agreement with experimental adsorption enthalpies is good, with a mean absolute deviation of 3.7 kJ/mol. In contrast to CO_2 adsorption, which exhibits

relatively strong electrostatic interactions that are 10-20 kJ/mol more exothermic than for CH_4,[174,183] the dominant contribution for methane binding arises from weaker dispersion interactions.

Regarding CH_4 capacity, GCMC is the standard method for predicting CH_4 uptake in porous materials.[51,175] Nevertheless, the accuracy of these predictions are only as good as the interatomic potentials employed. Although earlier GCMC calculations have found good agreement with measured CH_4 isotherms at moderate temperatures and pressures[185], more recent work has identified discrepancies with experiments at low temperatures and pressures[62,179] and in the location of preferred adsorption sites.[62] Herein we assess the sensitivity of the predicted uptake to the choice of interatomic potential by comparing six "off the shelf" CH_4-MOF potentials. The potentials differ in their description of the CH_4 molecule (single site[129,186] vs. 5-site,[187,188] charged vs. uncharged), and in the parameters used to describe the MOF atoms (charged vs. uncharged, UFF[128] vs. DREIDING[127]). We find that a simple uncharged single-site model for CH_4 based on the TraPPE[129] potential yields CH_4 uptake in DOBDC in best agreement with experiments.

The optimal inter-atomic potential is used to predict CH_4 uptake across the remainder of the M-DOBDC series, and in other noteworthy MOFs (MOF-5, PCN-11/14, and HKUST-1) as a function of maximum operating pressure (P_{max}) and for three operating scenarios: (i) *total capacity* at 298 K; (ii) *usable capacity* at 298 K assuming a pressure swing between P_{max} and 5 bar; and (iii) *usable capacity* assuming both a temperature and pressure swing from 298 K, P_{max} to 358 K (85°C), 5 bar. Although none of the studied compounds come close to achieving the DOE targets, we find that Be-DOBDC, PCN-11, and (surprisingly) MOF-5, provide the best combination of *usable*

gravimetric and volumetric capacities. Importantly, the EBS-containing MOFs Be-DOBDC and PCN-11 perform best at pressures less than ~50 bar; however, the presence of EBS is detrimental at higher pressures, where MOF-5 emerges as the best adsorbent. Moreover, the higher heat management requirements expected for EBS-containing MOFs (due to their larger ΔH) suggests that compounds without EBS should receive additional study as promising materials for CH_4 storage.

Finally, we expand our screening to a database of existing MOFs generated by Goldsmith *et al*.[55]. In particular, CH_4 uptake was predicted for those MOFs having surface areas larger than 1000 m^2/g. The screening shows that the correlation between volumetric and gravimetric CH_4 capacity is concave downward, similar to what has been found in prior screening of hypothetical MOFs. Our screening identifies SUKYON as a promising candidate given its high volumetric and gravimetric CH_4 densities.

5.2 Summary of Methods

5.2.1 Force-fields for CH_4 adsorption

To quantify the accuracy of the GCMC predictions, and their sensitivity to the choice of interatomic potential, isotherms were calculated using several existing potential forms and compared against experimental data.[68,177,178,189] Four descriptions of the CH_4 molecule were considered:

1. TraPPE:[129] represents methane as a neutral, single site spherical molecule.

2. Five-site model:[187] a charged 5-site model where C and H atoms are assigned charges of -0.66 and 0.165, respectively.

3. AA (all atom) model:[188] a neutral 5-site model.

4. TraPPE-EH:[186] an uncharged extension of the TraPPE model in which fictitious H atom sites are added at the center of the four C-H bonds.

Two parameterizations were examined for atoms associated with the MOF: (i) UFF[128]: the Universal Force Field is used for all MOF atoms, and (ii) DREIDING[127] parameters are used for H, C, and O atoms, with UFF[128] parameters for the metal sites. To simplify notation, we adopt the abbreviations "U" for UFF-based potentials, and "D-U" for the potential that mixes parameters from DREIDING and UFF.

Combining the description of the CH_4 molecule with the two descriptions for the MOF, a total 6 sets of force fields were considered: (*i.*) D-U+Five-site, (*ii.*) D-U+TraPPE, (*iii.*) U+Five-site, (*iv.*) U+TraPPE, (*v.*) D-U+AA, and (*vi.*) D-U+TraPPE-EH. These models were compared against experimental data for CH_4 adsorption in M-DOBDC with M = Mg, Mn, Co, Ni, and Zn.[68] The D-U+TraPPE potential was found to best reproduce the measured uptake data. This model was subsequently applied to the remainder of the M-DOBDC series and to MOF-5, PCN-11, PCN-14, and HKUST-1.

5.2.2 Methodology for screening MOFs mined fron the CSD

We calculated CH_4 capacities for ~600 known MOFs from the CSD. As previously described, Goldsmith *et al.*[55] constructed a database of ~22,700 "computation ready" compounds by searching the entire CSD. To reduce the expense of running calculations on such a large number of compounds, the compounds were filtered

according to their surface area. That is, we considered only compounds whose surface area was greater than 1000 m^2/g. This restriction is in line with the rough correlation between MOF surface area and gravimetric uptake and results in a screen consisting of 579 compounds. Compared to calculations on metal-substituted M-DOBDC and M-HKUST-1, these MOF structures were not relaxed; rather their structures were used as-is by adopting the experimental structure from the CSD..

To facilitate automation of the calculations, GCMC calculations were performed using the MUSIC code,[190] whose command-line interface can be easily scripted. A series of python and shell scripts were used to automate structure extraction from Goldsmith's database, as well as to prepare and analyze the output of GCMC calculations. Although Goldsmith' database intended to omit disordered structures,[55] some MOFs in that collection still exhibit disorder in their benzene rings. These structures were fixed by hand, and their geometry was optimized using a classical force-field. Finally, the "repaired" structures were run through GCMC..

5.3 CH_4 Adsorption in M-DOBDC

5.3.1 DFT benchmarking

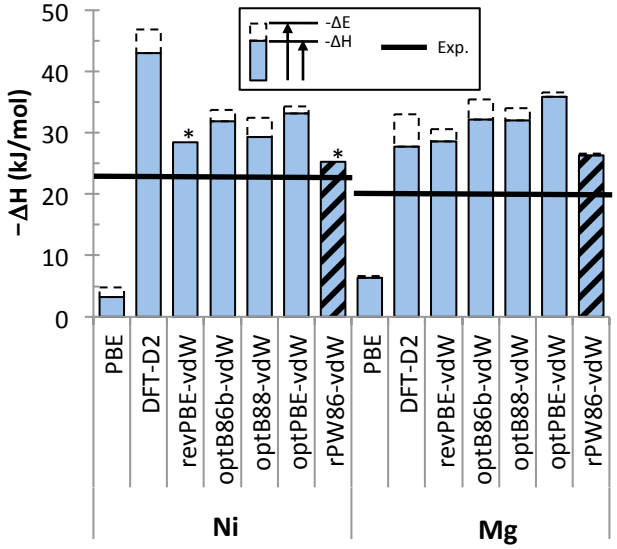

Figure 5.1 Comparison of calculated CH_4 adsorption energies in Mg and Ni-DOBDC as a function of calculation method with experimental data (Ref. 68). Adsorption enthalpies (ΔH) at 300 K are represented by solid columns. Cross-hatching is used to highlight the vdW-DF2 method (rPW86-vdW), which yields the best agreement with experimental data. The total column height corresponds to the 0 K static binding energy (ΔE); the dashed portion indicates the sum of zero point (ZPE) and thermal energy (TE) contributions. The experimental CH_4 adsorption enthalpy is depicted using a horizontal line. An asterisk indicates cases where ZPE+TE contributions are negative, see Table C.2 for numerical data.

Calculations on an alkaline earth and a transition metal-based system – Mg and Ni-DOBDC – were used to assess the accuracy of several "conventional" (i.e., PBE-GGA) and dispersion-corrected density functionals with respect to experimental adsorption enthalpies. These included the semi-empirical DFT-D2,[100] and the vdW-DF method with five distinct exchange functionals: revPBE (vdW-DF1),[102] optB86b,[110] optB88,[111]

optPBE,[111] and rPW86 (vdW-DF2).[112] Figure 5.1 and Table C.2 compare the calculated ΔH values for Mg and Ni-DOBDC with the experimental enthalpies from Reference 68. The experimental data were extrapolated to a coverage of 1 CH_4 per metal site by adding 2.7 kJ/mol to the reported enthalpies. The dashed portion of the columns in Fig. 5.1 represents the summed contribution of zero point (ΔE_{ZPE}) and thermal (ΔE_{TE}) energies to ΔH at 300 K. This contribution is typically endothermic,[174,183] ranging from 0.3 to 5.4 kJ/mol. [Exceptions occur for Ni-DOBDC in the cases of the revPBE (vdW-DF1) (-0.1 kJ/mol) and vdW-DF2 (-1.4 kJ/mol) functionals.]

As shown in Figure 5.1, the PBE-GGA significantly under predicts the experimental ΔH in both MOFs, with an average absolute error of 18 kJ/mol. The use of dispersion corrections greatly improves agreement with the experimental enthalpies, although in all cases the calculated ΔH values somewhat overestimate experiments. The best agreement is obtained with the vdW-DF2 functional, which uses rPW86-based exchange. In this case the calculated ΔH for Mg and Ni-DOBDC are, respectively, -26.3 and -25.3 kJ/mol. Sillar *et al.*[191] reported a methane adsorption enthalpy of -26.4 kJ/mol on Mg-DOBDC using a hybrid method based on MP2/PBE+D, in good agreement with our value. Compared to experiments, vdW-DF2 exhibits a small MAD of 3.7 kJ/mol, which is followed by the vdW-DF1 method (revPBE-based exchange) with an error of 6.4 kJ/mol. Comparable accuracy was reported for these two functionals in the case of CO_2 adsorption in MOFs.[174,183] MAD for the other dispersion-corrected functionals range from 9 – 13 kJ/mol. Given that the rPW86 and revPBE based vdW-DFs most closely reproduce the experimental enthalpies, we have adopted these functionals for calculations on the remaining M-DOBDC variants.

5.3.2 Thermodynamic Properties

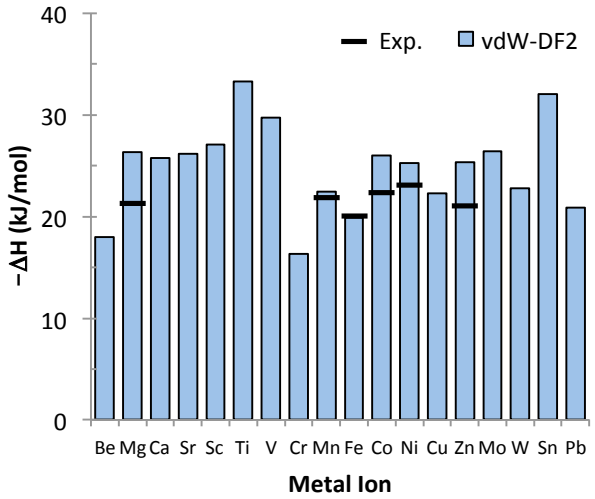

Figure 5.2 Adsorption enthalpies (ΔH) at T = 300 K for 18 metal substituted DOBDC MOFs calculated using the vdW-DF2 functional. Black horizontal lines indicate the experimental enthalpies from Reference 68, 192

Table 5.1 summarizes the methane adsorption enthalpies computed with the vdW-DF2 method across all 18 metal-substituted DOBDC variants; experimental data for Mg, Mn, Co, Ni and Zn-DOBDC from References 68 and 192 is included for comparison. These same data are depicted graphically in Figure 5.2. Contributions from the static binding energy (ΔE), zero point (ΔE_{ZPE}) and thermal energies (ΔE_{TE}) to the CH_4 adsorption enthalpies are given for vdW-DF2, vdW-DF1, and the PBE-GGA in Table C.3. Consistent with the preceding benchmarks, the vdW-DF2 method most accurately reproduces the experimental ΔH across the five M-DOBDC variants for which measurements have been reported. For this method the MAD of 2.7 kJ/mol is slightly less than that for vdW-DF1, 3.8 kJ/mol. In further agreement with experiments, the calculated ΔH values across these 5 M-DOBDC systems are relatively constant, varying by only 3-4 kJ/mol.

Table 5.1 Calculated adsorption enthalpies (kJ/mol CH_4) from vdW-DF2 for 18 metal substituted-variants of M-DOBDC. Experimental data is taken from Refs. 68,192.

Metal	Be	Mg	Ca	Sr	Sc	Ti	V	Cr	Mn
Calc.	18.1	26.3	25.8	26.2	27.1	33.3	29.7	16.4	22.5
Expt.		21.2							21.8
Metal	Fe	Co	Ni	Cu	Zn	Mo	W	Sn	Pb
Calc.	19.9	26	25.3	22.3	25.4	26.4	22.8	32	20.9
Expt.	20.0	22.3	22.9		21				

Across the full range of metal substitutions the methane adsorption enthalpy (ΔE) varies from -16.4 kJ/mol in the least exothermic case of Cr-DOBDC, to -33.3 kJ/mol in Ti-DOBDC, which has the most exothermic interaction with CH_4 overall. In addition to Cr, the other M-DOBDC variants that bind CH_4 relatively weakly ($|\Delta H| < 23$ kJ/mol) include: Be, Fe, Pb, Cu, Mn, and W. At the opposite extreme, Sn and V (in addition to Ti) show the strongest affinities for methane with ΔH = -32 and -29.7 kJ/mol, respectively. Ni, Zn, Ca, Co, Sr, Mg, Mo, and Sc fall in the intermediate ΔH range of -25 to -27 kJ/mol.

To put these values into perspective, earlier calculations[183] of adsorption enthalpies for CO_2 on M-DOBDC reported interactions which were much more exothermic and which exhibited a wider range of values: ΔH = -25 to -53.5 kJ/mol at 300 K. Clearly CH_4 adsorption in M-DOBDC is generally weaker than for CO_2. Nevertheless, several trends are shared between these two adsorbates. For example, adsorption in the 3d metals is strongest for the early transition metals (Sc, Ti, V). Moving to the right in the periodic table, the interaction weakens for Cr and then roughly strengthens again as one continues across the 3d series. The trends between CO_2 and CH_4 are also similar for the alkaline and alkaline earth metals, where Mg, Ca, and Sr exhibit relatively strong adsorptive interactions with both molecules. A shared exception is the lower binding

energy for Be-DOBDC. Upon relaxation, Be becomes buried (and therefore inaccessible) inside the MOF structure, preventing direct interactions with the adsorbed guest molecule, and resulting in less exothermic adsorption enthalpies. Consequently, a site slightly displaced towards the ligand is the preferred location for CO_2 adsorption in Be-DOBDC.[183]

5.3.3 Electronic Structure

The different magnitudes of the adsorption enthalpies for CO_2 vs. CH_4 on M-DOBDC can be attributed to differences in the strength of electrostatic interactions between the CUS and the adsorbate molecules. Although neither CO_2 nor CH_4 possesses a permanent dipole, they differ in their polarizability and distribution of atomic charges. CO_2 is more polarizable, and its outer oxygen atoms have a net negative charge. These two factors result in a more exothermic interaction with (positive) CUS ions, and a more pronounced sensitivity to the charge state of the metal, which is manifested as a wider range in ΔH.[183] In contrast, CH_4 has a lower polarizability and its hydrogen atoms have a slight positive charge, resulting in less exothermic, and more uniform, interactions with the CUS.

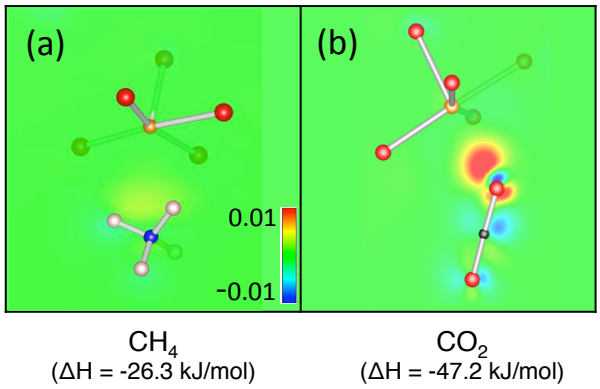

Figure 5.3 Charge density difference plots (relative to the isolated components) for (a) CH_4 and (b) CO_2 adsorption (in chapter 4) on Mg-DOBDC. For simplicity, only the CUS metal and its nearest neighbors are shown. Red represents charge accumulation and blue is charge depletion. Blue spheres = C, white = H, gold = Mg, and red = O.

Evidence that electrostatic interactions play a smaller role in CH_4 adsorption can be seen in the charge density difference plots of Figure 5.3, which compare the degree of charge redistribution upon adsorption of CH_4 and CO_2 on Mg-DOBDC. (Additional data for M = Sn, Mo and Zn are presented in Figure C.1.) Compared to CO_2,[183] the degree of charge density redistribution on CH_4 and in the regions between CH_4 and the MOF is much smaller (0.011 e/Å^3 for CO_2, *vs.* 0.003 e/Å^3 for CH_4), consistent with the smaller CH_4 adsorption enthalpy (~21 kJ/mol less exothermic than for CO_2), and suggesting that van der Waals interactions play a more dominant role in CH_4-MOF adsorption. The charge density redistribution for CO_2 in Mg-DOBDC has a maximum that is 20% greater than for CH_4 in Mo-DOBDC (Figure C.1(b)), and also occurs over a larger region. Although there is no significant charge redistribution between CUS and CH_4 in Sn-DOBDC (Figure S1d), however, the somewhat more exothermic adsorption enthalpy (as described below) originates from secondary interactions involving the ligand.

Local density of states (LDOS) plots for Mg, Mo, Zn, Sn-DOBDC before and after CH_4 adsorption are shown in Figure C.1. Although there is no noticeable change in

the MOF metal-projected DOS upon adsorption, in all cases the CH_4 states shift towards lower energies, consistent with the presence of a weak electrostatic component to binding. A larger shift in the CO_2 DOS upon adsorption was previously observed in these systems.[183] Additional evidence that van der Waals contributions are the primary component of the CH_4 binding energy is given in Table C.4, which shows that the van der Waals contribution is generally large and exothermic Finally, we recall that adsorption of CO_2 in M-DOBDC and M-HKUST-1 was accompanied by a large distortion in the CO_2 molecular geometry.[174,183] However, no significant change of this type is observed in the case of CH_4.

Our prior study of CO_2 capture in metal-substituted MOFs identified a trend relating the magnitude of ΔH with the effective charge on the CUS.[183] This trend arose from the strong electrostatic contributions to the CO_2-MOF interaction. In the case of CH_4 adsorption, Table C.4 and Figure C.3(c) show (with the exception of Sn) the presence of a similar, but somewhat weaker trend. That this trend is less pronounced for CH_4 is consistent with the smaller role played by electrostatics in this system. [Due to its unique adsorption geometry (as discussed previously), these correlations often do not hold for Sn-DOBDC.] In addition, Figure C.3(b) shows that ΔH weakly correlates with the ionic radius of the CUS, in cases where the radius is relatively small (< 1.0 Å). This trend can be explained as follows: In the adsorbed MOF complexes, hydrogen from CH_4 is in close proximity to the carboxyl oxygen atoms on the MOF, while the carbon from CH_4 approaches the MOF's CUS. Such an arrangement minimizes the separation between pairs of oppositely charged (attracting) atoms. An increase to the ionic radius of the CUS elongates metal-O bonds in the MOF and allows the bulky CH_4 to approach the

framework more closely. This has the effect of minimizing these bond lengths and increasing the strength of interaction. Finally, Table C.5 and Figure C.3 (d) illustrate a clear trend between increasing bond exothermicity (more negative ΔH) and decreasing Metal – C(CH_4) and O – H(CH_4) distances.

Experiments[68] have demonstrated that CUS are the primary adsorption site for CH_4 in DOBDC at pressures up to a loading of one CH_4/metal. At higher loadings other sites will become occupied; however, these secondary (or tertiary) sites have not been widely explored. To probe these, calculations were performed at several alternative adsorption sites in Ni-DOBDC. The three sites identified as being most energetically favorable are illustrated in Figure C.2. We find that the adsorption energy at the carboxyl oxygen site (Fig. C.2 (b)) adjacent to the CUS is comparable to that at the CUS: the carboxyl site is only 0.3 kJ/mol less favorable (ΔE = -23.6 kJ/mol) than the CUS site (Fig., C.2(a), ΔE = -23.9 kJ/mol), likely due to the fact that CH_4 maintains a similar bond length (3.54 Å) to the CUS in this position. Binding to the aromatic ring C-site (Fig. C.2(c)) is somewhat weaker, ΔE = -20.6 kJ/mol. Calculated bond distances between C (in CH_4) and the different MOF sites correlate with the binding energy: 3.29 (Metal site), 3.53 (carboxyl O-site), and 3.70 Å (C-ring site).

5.3.4 Comparison of Interatomic Potentials

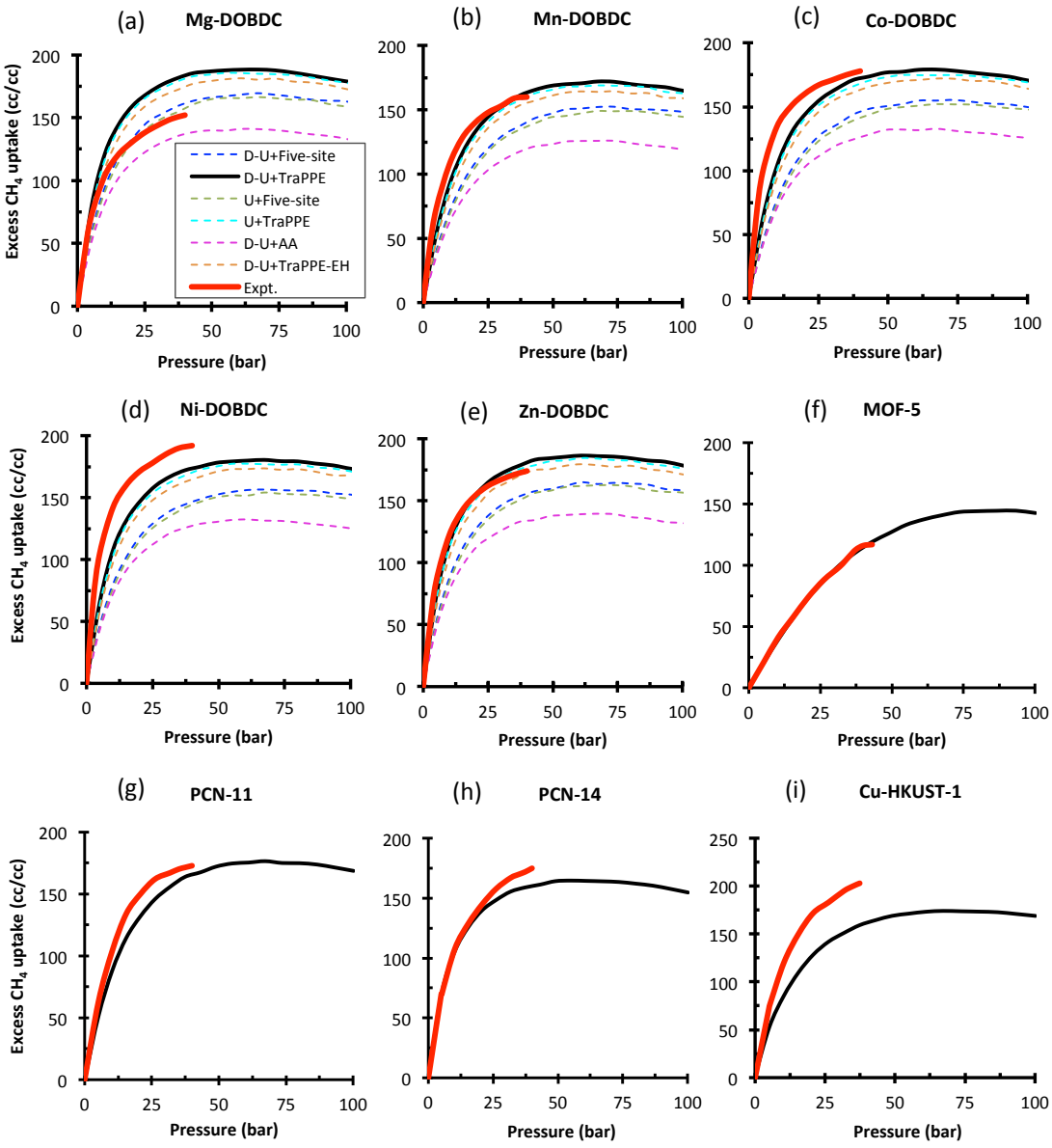

Figure 5.4 Comparison of calculated excess CH_4 adsorption isotherms (at 298 K) evaluated using 6 distinct force-fields with experimental isotherms for [Mg, Mn, Co, Ni, Zn]-DOBDC, MOF-5, PCN-11 and for PCN-14 and Cu-HKUST-1 (Refs. 27, 68, 152, 177, and 189). Descriptions of the force-field models are provided in the Methods Section. Experimental isotherms are depicted using a solid red line; the black solid line highlights the performance of the D-U+TraPPE force-field, which yields the best overall agreement with the experimental data.

The methane storage capacity predicted by GCMC calculations will depend upon the inter-atomic potentials used to describe the interaction between methane and the MOF. It is therefore helpful to examine the degree to which common potentials reproduce experimental isotherms.[51,179,182,193,194] Here we explore how varying the force-field properties – e.g., presence/absence of partial atomic charges, unified atom vs. a 5-site model of CH_4, *etc.* – impacts the accuracy of the predicted storage capacity. The performance of 6 distinct force fields is assessed (details are provided in the Methods Section): D-U+Five-site, D-U+TraPPE, U+Five-site, U+TraPPE, D-U+AA, and D-U+TraPPE-EH. Comparisons are made first to the experimental excess adsorption isotherms reported by Refs. 68 and 24 across a series of five M-DOBDC compounds with M = Mg, Mn, Co, Ni and Zn, and are subsequently extended to MOF-5, HKUST-1, PCN-11 and PCN-14.[27,177,189]

Figure 5.4(a)-(e) compares the methane isotherms for M-DOBDC calculated with these force fields to experimental measurements.[27,68] Several observations can be made from these data. First, varying the LJ parameters of the MOF atoms between the UFF (U) and Dreiding+UFF (D-U) force fields results in a negligible difference in the predicted isotherms. This is not surprising given that both models use LJ parameters from the UFF to describe the CUS, and the CUS site is the primary adsorption site (Fig. C.4). Second, the predicted uptake is much more sensitive to the potential used to describe the methane molecule. For example, the uncharged all atom (AA) model for CH_4 shows the greatest deviation with experiments, and consistently (and significantly) underestimates the measured uptake. Likewise, methane uptake is generally under-predicted by the five-site charged model. Overall, we find that the D-U+TraPPE model (solid black line) yields the

best agreement with experiments. As the TraPPE-EH potential is closely related to the TraPPE, we expect (and observe) that isotherms predicted by these two force-fields are similar.

The performance of the 6 force fields in reproducing the experimental CH_4 uptake for M-DOBDC has been quantified by evaluating the mean absolute deviation (MAD). The MAD was calculated as an average over the deviation in CH_4 uptake at 8 pressures in the range 0.1 – 35 bar: 0.1, 5, 10, 15, 20, 25, 30, and 35 bar. Comparisons at lower pressures such as 5 bar are desirable because estimates of usable capacity rely on the differential uptake at 5 bar and at higher pressures. The MAD for each force field averaged across the M-DOBDC series is summarized in Figure 5.5(a). Deviations are smallest (16 cm^3/cm^3) for the D-U+TraPPE model and largest (45 cm^3/cm^3) for the uncharged all atom (AA) potential.

The performance of the D-U+TraPPE force-field was examined further by comparing its predicted CH_4 uptake to experimental data for four other prominent MOFs: MOF-5,[189] PCN-11,[177] PCN-14,[27] and HKUST-1.[27] Calculated excess isotherms are shown in Figure 5.4(f)-(i), while Figure 5.5(b) plots the MAD for each individual compound. The simulated isotherms are in reasonably good agreement with measurements, especially for the cases of MOF-5, PCN-11, and PCN-14. In these three MOFs the MAD with respect to experimental uptake ranges from a low of 1.0 (MOF-5) to a high of 12.5 (PCN-11) cm^3/cm^3 for the pressure range 0.1 – 35 bar. However, the agreement with experiments is somewhat worse for HKUST-1 (MAD = 33), with GCMC under-predicting CH_4 uptake, similar to what has been observed in prior studies.[63] Likewise, inspection of the isotherms for PCN-11 and PCN-14 [Figs. 5.4(g,h)] also

shows that GCMC systematically underestimates uptake in these MOFs, albeit to a smaller degree. In all three of these MOFs the deviation from experiments is small at low CH_4 loading (i.e., low pressures), but then grows as the loading increases. Notably, the tendency for GCMC to under-predict uptake does not apply to the M-DOBDC compounds, which also contain CUS.

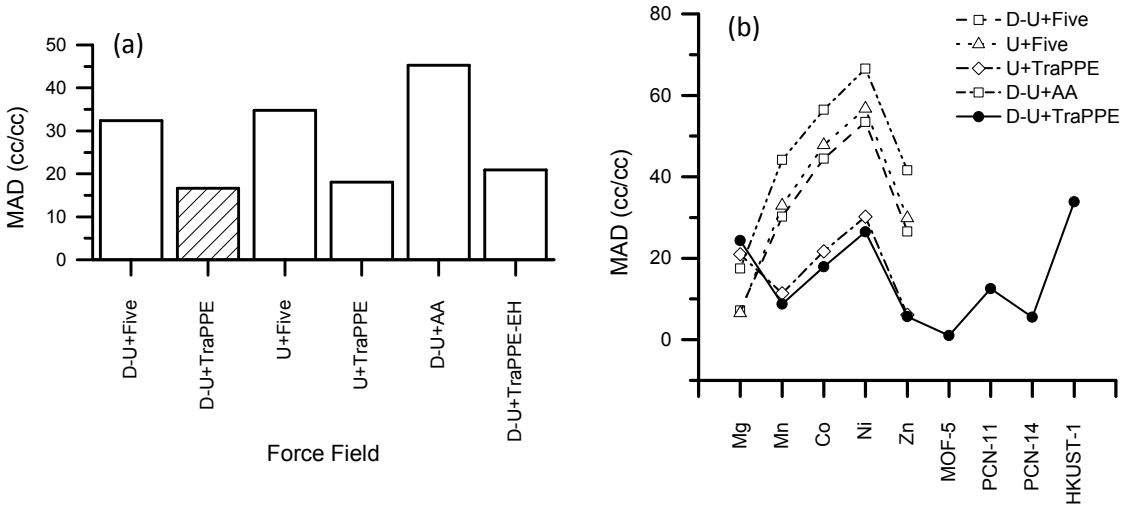

Figure 5.5 Mean Absolute Deviation (MAD) between the calculated CH_4 uptake and experiments. (a) MAD as a function of inter-atomic potential. Here the MAD is averaged over 5 M-DOBDC variants (M = Mg, Mn, Co, Ni, Zn). The best-performing potential, D-U+TraPPE, is highlighted with cross-hatching. (b) MAD for individual MOFs.

These trends can be understood by referring to previous experiments[62,63,68] and GCMC modeling.[62,63] In the cases of PCN-11, PCN-14, and HKSUST-1, it is known[62,63] that conventional classical potentials do not properly account for interactions with the Cu CUS, resulting in limited adsorption at these sites. (Our calculations confirm this behavior – see Fig. C.4 for a plot of the methane adsorption density in PCN-11, PCN-14, and HKUST-1.) Nevertheless, diffraction experiments[62,63] have shown that these same sites are primary sites for CH_4 adsorption, with a high occupancy (93%)[63] of CH_4 under saturation conditions. In the regime of low loadings/low pressures, it has been reported

that the CUS fill more slowly than the more-easily-accessed "pocket" sites: for example, in HKUST-1 only 44% of the CUS are occupied at 59% of maximum loading.[63] On the other hand, adsorption within the pocket sites is correctly captured by GCMC.[62,179] Taken together, these observations suggest that the omission of enhanced CH_4-CUS binding in classical potentials will result in an under-prediction of CH_4 uptake that is small at low coverage, but then grows as the CH_4 loading increases. This same trend is observed in Figs. 5.4(g-i). We also expect that the extent to which GCMC underestimates experiments will correlate with the fraction of CH_4 molecules adsorbed at CUS. At 35 bar and 298 K, experiments find the fraction of adsorbed CH_4 at CUS to be largest in HKUST-1 (61%), and somewhat smaller in PCN-11 (41%) and PCN-14 (27%).[62] These percentages track the MAD for these three compounds, Fig. 5.5(b).

In contrast to the behavior of HKUST-1, PCN-11, and PCN-14, GCMC calculations on the M-DOBDC series show no such systematic deviation with the experimental uptake. This is because GCMC *does* correctly reproduce the CUS as being the primary CH_4 adsorption site[68] (see the CH_4 density distribution plots for Mg- and Ni-DOBDC in Fig. S4.) The reason that the CUS sites are property treated in M-DOBDC with classical potentials may be due to the fact that in M-DOBDC the CUS sites coincide with corner sites in the framework, where enhanced vdW interactions are likely to occur.

To test this hypothesis, we calculated the CH_4 uptake in a fictitious MOF, "C-DOBDC," in which the Ni CUS from Ni-DOBDC was replaced with a C atom. Figure C.10 compares the CH_4 density distribution for Ni-DOBDC and C-DOBDC, revealing that there is no significant difference between these MOFs. Moreover, the calculated CH_4 uptake in both cases differs by less than 10% (~15 cm^3/cm^3). Finally, the isosteric heats

of adsorption, Q_{st}, calculated using the classical potentials (Table C.8) show almost no sensitivity to the composition of the CUS, unlike the DFT or experimental data (Table 5.2). These calculations confirm that it is the geometry of the corner-like CUS site, rather than the presence of the CUS itself, which makes these sites preferred locations for CH_4 adsorption in DOBDC.

Despite these limitations, the simple D-U+TraPPE potential yields quite reasonable predictions of CH_4 capacity: including data from all 9 MOFs, we find that the D-U+TraPPE force field exhibits a MAD of 15 cm^3/cm^3 across the range of 0.1 – 35 bar. (For comparison, evaluating the MAD at a single pressure of 35 bar gives a MAD of 14 cm^3/cm^3.) As most high-capacity MOFs have excess CH_4 capacities exceeding 150 cm^3/cm^3, a MAD of this magnitude would result in an error of approximately 10%. While we believe this is sufficient to enable screening of candidate MOFs,[51] outliers with larger deviations on the order of 30 cm^3/cm^3 (such as HKUST-1) do exist (Fig. 5.4i). Hence, further optimization of CH_4—MOF force fields would be discuss in next chapter.

Of course one should not forget that variation in the synthesis and measurement of CH_4 uptake may also contribute to the deviations observed with simulation. For example, follow-up measurements[27] of methane adsorption on Ni-DOBDC and PCN-14 found that total uptake capacity at 35 bar differed from previous reports[68,178] by 28-35 cm^3/cm^3; similar differences were observed for HKUST-1.[27,164,195] To address these uncertainties, round-robin testing by different groups on a small number of prototype materials would clearly be beneficial. With these caveats in mind, we have employed the D-U+TraPPE force field to predict total methane storage capacities across the remainder

of the M-DOBDC series, and to examine the effect of realistic operating conditions on the achievable (i.e., usable) CH_4 capacity.

5.3.5 CH_4 Storage Capacity: Total *vs.* Usable

Table 5.2 Predicted volumetric (cm^3/cm^3) and gravimetric (g/g) CH_4 storage capacities in several MOFs as a function of pressure and temperature. All capacities include adsorbed and gas-phase CH_4. "Total" refers to the capacity at 298 K assuming an isothermal pressure swing between the maximum pressure (P_{max} = 35, 65, or 100 bar) and zero bar. "Usable" refers to the capacity obtained from either an (a) isothermal (298 K) pressure swing (PS) between $P_{max} \rightarrow$ 5 bar; or (b) temperature + pressure swing (TPS) from 298 K, P_{max} to 358 K, 5 bar.

MOF	P_{max} = 35 bar				P_{max} = 65 bar				P_{max} = 100 bar			
	Total		Usable		Total		Usable		Total		Usable	
	298 K		298 K (PS)	358 K (TPS)	298 K		298 K (PS)	358 K (TPS)	298 K		298 K (PS)	358 K (TPS)
	cc/cc	g/g	cc/cc	cc/cc	cc/cc	g/g	cc/cc	cc/cc	cc/cc	g/g	cc/cc	cc/cc
Be-DOBDC	204	0.17	118	169	230	0.20	144	195	245	0.21	160	211
Mg-DOBDC	200	0.16	122	168	228	0.18	150	196	243	0.20	165	211
Ca-DOBDC	187	0.15	123	161	218	0.18	153	191	235	0.19	170	208
Sr-DOBDC	175	0.11	116	150	206	0.13	147	181	222	0.14	163	197
Sc-DOBDC	179	0.11	100	147	198	0.12	119	166	211	0.13	132	179
Ti-DOBDC	192	0.13	128	165	223	0.16	159	196	240	0.17	176	213
V-DOBDC	189	0.12	124	162	220	0.15	155	193	237	0.16	171	210
Cr-DOBDC	178	0.11	117	152	207	0.13	147	182	225	0.14	164	199
Mn-DOBDC	178	0.12	123	155	210	0.14	155	187	228	0.15	173	205
Fe-DOBDC	185	0.12	127	160	215	0.14	157	190	233	0.15	175	208
Co-DOBDC	188	0.12	124	162	218	0.14	154	191	234	0.15	170	208
Ni-DOBDC	189	0.11	122	162	217	0.13	150	189	234	0.14	167	207
Cu-DOBDC	171	0.10	111	145	197	0.11	137	172	212	0.12	152	187
Zn-DOBDC	196	0.12	121	166	225	0.14	150	195	241	0.15	166	210
Mo-DOBDC	174	0.08	115	149	200	0.10	141	175	215	0.10	156	190
W-DOBDC	183	0.06	118	156	210	0.07	145	183	226	0.08	160	198
Sn-DOBDC	197	0.09	98	157	219	0.10	120	179	234	0.11	135	194
Pb-DOBDC	210	0.08	113	169	234	0.09	138	194	248	0.10	152	208
MOF-5	132	0.16	110	120	189	0.24	168	178	225	0.28	203	213
PCN-11	183	0.18	130	159	222	0.22	169	198	244	0.24	191	220
PCN-14	178	0.16	108	148	205	0.19	134	175	222	0.20	151	192
HKUST-1	178	0.15	125	152	219	0.18	165	192	242	0.20	188	215

The methane storage capacity was evaluated for pressures up to 100 bar, and was tabulated for three operating scenarios using maximum working pressures, P_{max}, of 35, 65, and 100 bar. The operating scenarios include: (*i.*) *total capacity* at 298 K and P_{max}; (*ii.*) *usable capacity* at 298 K, assuming an isothermal pressure swing (PS) from P_{max} to 5 bar; and, (*iii.*) *usable capacity* assuming both a temperature and pressure swing (TPS) from 298 K and P_{max} to 358 K (85°C) and 5 bar. Total methane uptake isotherms at 298 K for P = 0 – 100 bar are shown in Figure 6 for four representative MOFs from the M-DOBDC series (M = Ni, Cu, Be, and Pb) and for MOF-5, PCN-11, PCN-14 and HKUST-1. A summary of the storage capacities for all 22 MOFs across all operating scenarios is given in Table 3; isotherms for all compounds are provided in Figure S5. In the following sections we first report total capacities, and then subsequently expand our analysis to consider usable capacities under PS and TPS operating scenarios.

Total capacity: We define the total methane capacity at a specified temperature (298 K) and pressure P_{max} as the sum of CH_4 stored in a single-crystal MOF monolith both as adsorbed molecules on the surfaces of pores, and as gas-phase molecules within those pores. The total capacity is an upper bound to the achievable (or useable) capacity in a practical storage system, given that: (*i.*) the total capacity represents the capacity that could hypothetically be achieved if *all* CH_4 could be removed from the MOF. For PS operation, this would require a vanishing pressure of CH_4 within the storage vessel, whereas the DOE targets (Table 1) specify a lower pressure limit of 5 bar; (*ii.*) the adsorbent media in a practical system will exhibit a lower packing density than that of a hypothetical single crystal monolith. Consequently, a viable CH_4 storage material must have a total capacity that (likely far) exceeds the targets.

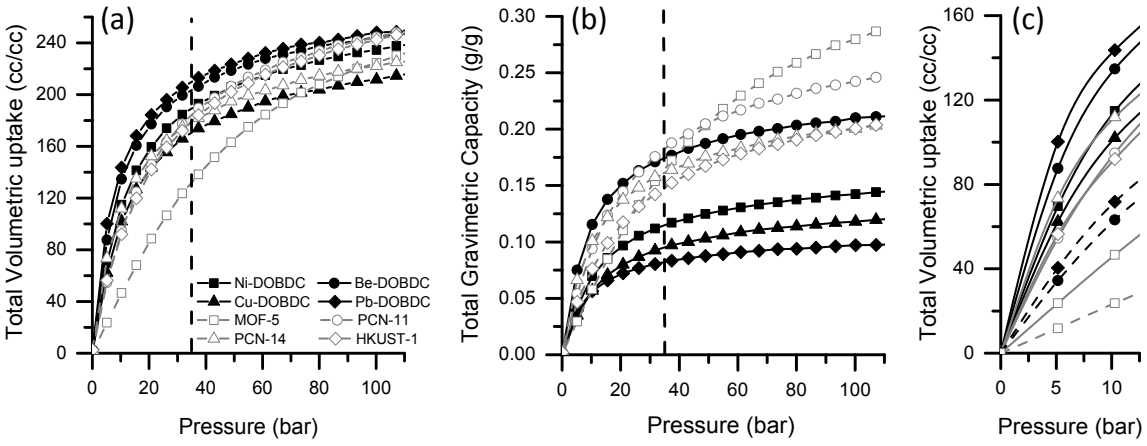

Figure 5.6 Calculated CH_4 adsorption isotherms (evaluated using the D-U+TraPPE interatomic potential) for selected M-DOBDC variants, and for MOF-5, PCN-11, PCN-14 and HKUST-1. (a) Total volumetric uptake (cm^3/cm^3) for 0 – 100 bar and 298 K. The vertical dashed line indicates a pressure of 35 bar, which is the pressure at which the DOE storage targets are specified. (b) Total gravimetric uptake (g/g) for 0 – 100 bar and 298 K. (c) Magnification of the volumetric isotherms in panel (a) at low pressure, P = 0 – 12.5 bar. Dashed isotherms are for T = 358 K.

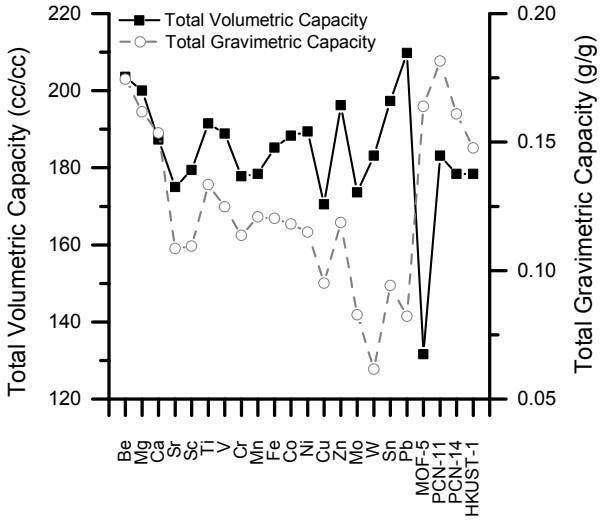

Figure 5.7 Total CH_4 uptake at 35 bar and 298 K on a volumetric (left axis) and gravimetric (right axis) basis. Calculations were performed using the D-U+TraPPE force field; Metal symbols (M) along the x-axis refer to the composition of M-DOBDC.

Figures 5.6(a) and 5.7 illustrate that for P_{max} = 35 bar, the total volumetric capacities of the MOFs studied here fall within a range of 171 – 210 cm^3/cm^3. (MOF-5 is an exception to this trend, with a much lower capacity of 132 cm^3/cm^3.) In the case of the M-DOBDC compounds, the comparable volumetric capacities can be explained by the fact that the CUS act as primary adsorption sites,[68] and the density of these sites is similar across the nominally isostructural M-DOBDC series, ranging from 3.62 – 4.98 sites/nm^3, Table C.6. Two hypothetical M-DOBDC compounds with M = Be and Pb are predicted to have the highest total volumetric uptake at 204 and 210 cm^3/cm^3, respectively. Moreover, several other members of the M-DOBDC family (M= Mg, Ca, Ti, V, Fe, Co, Ni, Zn, W, and Sn) have calculated total capacities exceeding 180 cm^3/cm^3 (Table 5.2). Similar volumetric capacities of 178-183 cm^3/cm^3 are predicted for PCN-11, PCN-14, and HKUST-1.

Unfortunately, the volumetric benefits conferred by the high density of CUS in the M-DOBDC compounds generally come at a cost to gravimetric performance. Figures 5.6(b) and 5.7 illustrate this tradeoff. For example, even though Pb-DOBDC has the highest total volumetric capacity at P_{max} = 35 bar, the high mass of Pb (207.2 amu) results in this compound having the 2nd-lowest gravimetric uptake overall (0.08 g/g). Conversely, M-DOBDC compounds in which the CUS consists of the light alkaline earth metals Be and Mg have amongst the best gravimetric capacities, 0.17 and 0.16 g/g, respectively. Given that these compounds also have high volumetric capacities (204 & 200 cm^3/cm^3, Table 5.2), this pair of MOFs exhibits the best combination of total volumetric and gravimetric CH_4 capacity under these conditions. Continuing the correlation of gravimetric capacity with the mass of the CUS, M-DOBDC compounds for which M

consists of a 1st row transition metal have somewhat lower capacities of 0.10 – 0.13 g/g. Finally, gravimetric capacities are also high in PCN-11, PCN-14, and HKUST-1, ranging from 0.15 to 0.18 g/g. Although these compounds have Cu-based CUS, the density of these sites is lower than in the M-DOBDC series (1.82 – 2.58 sites/nm^3), lessening their gravimetric penalty.

If operation at pressures above 35 bar is possible, then slightly higher total capacities can be achieved. Figures 5.6(a-b) illustrate CH_4 uptake isotherms for selected MOFs for pressures up to 100 bar, while Table 5.2 summarizes total capacities at P_{max} = 65 and 100 bar. For the best-performing MOFs at 35 bar, Be- and Mg-DOBDC, a near doubling of P_{max} to 65 bar results in only a small 13% increase in volumetric capacity (228-230 cm^3/cm^3), and a 15% increase in gravimetric capacity (0.18-0.20 g/g). At these pressures the capacity of PCN-11 (222 cm^3/cm^3, 0.22 g/g) also begins to "catch-up" with these two compounds. Increasing the pressure further to 100 bar results in diminishing capacity gains in all three of these compounds of only 7-9% for both volumetric and gravimetric CH_4 density. At this pressure PCN-11 attains the best overall capacity of 244 cm^3/cm^3 & 0.24 g/g, while Be/Mg-DOBDC and HKUST-1 are close runners-up (242 – 245 cm^3/cm^3 & 0.20 – 0.21 g/g). Although these high total capacities represent a best-case scenario, they are only 70% of the DOE volumetric target of 349 cm^3/cm^3, and less than half (48%) of the 0.5 g/g gravimetric target. As we describe next, accounting for residual CH_4 present at the lower pressure limit of 5 bar (i.e., during a pressure swing) further reduces these capacities.

Usable capacity — isothermal pressure swing (PS): As previously described, the usable capacity differs from the total capacity in that the former assumes a minimum

operating pressure of 5 bar (consistent with the DOE targets), while the latter assumes the hypothetical desorption of all CH_4, corresponding to a minimum pressure of 0 bar. Figure 5.6(c) magnifies the adsorption isotherm for selected MOFs from panel 5.6(a) within the low-pressure region, P < 12.5 bar. With the exception of MOF-5, it is clear that each of the examined MOFs retains significant quantities of CH_4 at 5 bar. These "residual capacities" range from 53 cm^3/cm^3 in HKUST-1 and PCN-11 to 97 cm^3/cm^3 in Pb-DOBDC, and represent 30-46% of the total volumetric capacity at 35 bar. In contrast, the CH_4 capacity of MOF-5 at 5 bar is only 22 cm^3/cm^3. The smaller uptake in MOF-5 can be attributed to the absence of EBS in its crystal structure. In contrast, all of the other MOFs examined here contain EBS. The increased interactions occurring at EBS – be they through enhanced electrostatics at CUS or enhanced vdW bonding at pocket sites – results in a more rapid filling of these sites at low pressures, which is manifested as a steeper rise in the isotherms of these MOFs.[63]

The consequences of significant residual CH_4 capacity at low pressure can be seen in Table 5.2. The calculated usable volumetric capacities assuming a PS to 5 bar are significantly lower than the *total* capacities. (Usable gravimetric capacities are reported in T able C.7.)For P_{max} = 35 bar, PCN-11 exhibits the highest usable volumetric capacity of 130 cm^3/cm^3, and 2nd highest gravimetric capacity of 0.13 g/g. These values are 28-38% smaller than the largest *total* capacities – 210 cm^3/cm^3 in Pb-DOBDC and 0.18 g/g in PCN-11 – at the same P_{max}. This trend towards reduced capacity extends to higher pressures of P_{max} = 65 and 100 bar, where the largest usable volumetric capacities are respectively 28% and 18% smaller than the largest total capacities at the equivalent P_{max}.

As P_{max} increases, the identity of the best-performing MOFs also changes. In particular, MOF-5 emerges as the MOF having the best combination of usable gravimetric and volumetric PS capacity at pressures above approximately 50 bar. The calculated capacity for MOF-5 at 65 bar is 168 cm^3/cm^3 & 0.21 g/g, and 203 cm^3/cm^3 & 0.25 g/g at 100 bar. This might come as a surprise given that MOF-5 has the *lowest* total volumetric capacity at these same P_{max}. *This behavior highlights the pitfalls that may arise by focusing only on total, rather than on usable, capacity.* In our opinion, the reporting of usable capacities should be given a much higher priority. The re-emergence of venerable MOF-5 as a high capacity adsorbent can be traced to the shape of its isotherm, Fig. 6(a-c). Due to the absence of EBS, CH_4-MOF-5 interactions are relatively weak, ΔH = 12 kJ/mol[189]. Thus, the MOF-5 isotherm has a less pronounced slope at lower pressures, resulting in less retained CH_4 at 5 bar compared to the other MOFs. On the other hand, its slope is steepest at higher pressures, resulting in a more rapid increase in uptake with increasing pressure. Taken together, these observations suggest that EBS – due to their tendency to increase uptake at low pressures – can be *detrimental* at higher pressures for operating scenarios that employ an isothermal pressure swing. Figure S6 illustrates the crossover in CH_4 storage density for MOF-5 and PCN-11 as a function of P_{max}.

Usable capacity – temperature + pressure swing (TPS): Higher usable capacities can be achieved if desorption is triggered by a combined pressure and temperature swing. This operating scenario could be implemented using waste heat from combustion to warm the storage vessel during driving. The system would then be cooled at the forecourt during refueling. The benefits of this approach are illustrated in Fig. 5.6(c), which shows

a reduction in the amount of residual CH_4 stored at 5 bar upon heating to 85°C (358 K). (Our choice for this specific desorption temperature is motivated by the DOE requirement that the system temperature not exceed 358 K.)[41] Whether TPS operation would be advantageous will depend on the tradeoff between higher CH_4 capacity *vs*. the costs and efficiency losses associated with an in-tank heat exchanging system and additional cooling at the forecourt.

Table 5.2 demonstrates that TPS operation does in fact increase capacity beyond that of PS operation. For example, for P_{max} = 35 bar, Be-DOBDC is predicted to have the highest usable TPS capacity of 169 cm^3/cm^3. This is a 30% increase over the highest usable PS capacity (130 cm^3/cm^3 for PCN-11), yet remains 17% less than the total capacity of Be-DOBDC (204 cm^3/cm^3). At higher pressures the capacity advantage of TPS over PS diminishes: at 65 bar the capacities of the best-performing TPS MOFs are 17% larger than the best PS MOFs, and only 8% larger at 100 bar.

We note that the unfavorable performance associated with the EBS-MOFs under PS operation is minimized upon inclusion of a temperature swing. For example, Table 5.2 shows that Be- and Mg-DOBDC have amongst the highest TPS capacities at all values of P_{max}. This is of course due to the lower residual capacities present in these compounds at higher temperatures, Fig 5.6(c), and suggests that EBS-MOFs can yield competitive capacities under TPS operation.

A summary of the best-performing MOFs and their respective capacities as a function of operating conditions is given in Table 5.3. (Here, "best-performing" refers to those MOFs that provide the best combination of volumetric and gravimetric capacity.) Of the 22 MOFs examined, Be-DOBDC, PCN-11, and MOF-5 emerge as the most

promising methane adsorbents. Be-DOBDC and PCN-11 yield the best performance at low-to-moderate pressures of 35-65 bar, while MOF-5 is best at moderate to-high pressures. To our knowledge Be-DOBDC has not yet been synthesized. However, given that the performance of well-known Mg-DOBDC is very similar to that of Be-DOBDC, one may substitute Mg for Be and achieve comparable properties.

Table 5.3 MOFs exhibiting the best combination of volumetric and gravimetric CH_4 density as a function of operating conditions.

Operating Condition, P_{max}	Best MOF(s) (CH_4 capacity: cm^3/cm^3 : g/g)
Total, 35 bar	Be-DOBDC (204 : 0.17)
Total, 65 bar	Be-DOBDC (230 : 0.20); PCN-11 (222 : 0.22)
Total, 100 bar	PCN-11 (244 : 0.24); MOF-5 (225 : 0.28)
Usable PS, 35 bar	PCN-11 (130 : 0.13)
Usable PS, 65 bar	MOF-5 (168 : 0.21)
Usable PS, 100 bar	MOF-5 (203 : 0.25)
Usable TPS, 35 bar	Be-DOBDC (169 : 0.15)
Usable TPS, 65 bar	PCN-11 (198 : 0.20)
Usable TPS, 100 bar	MOF-5 (213 : 0.27)

In addition to capacities, the thermal properties of the MOF can also impact performance. In particular, large enthalpies of adsorption (Fig. 5.2) will generate greater cooling and heating loads during CH_4 uptake and release. These loads translate to higher costs and mass penalties associated with the heat exchanging subsystem in the storage vessel. As MOFs with EBS typically exhibit larger adsorption enthalpies – for example, ΔH ranges from 21 to 26 kJ/mol in Mg-DOBDC (Ref. 68 and Table 5.2) and is estimated

at 15 kJ/mol in PCN-11[177] – we anticipate that these MOFs will be less desirable than MOF-5 (ΔH = 12 kJ/mol[189]) from a heat management standpoint.

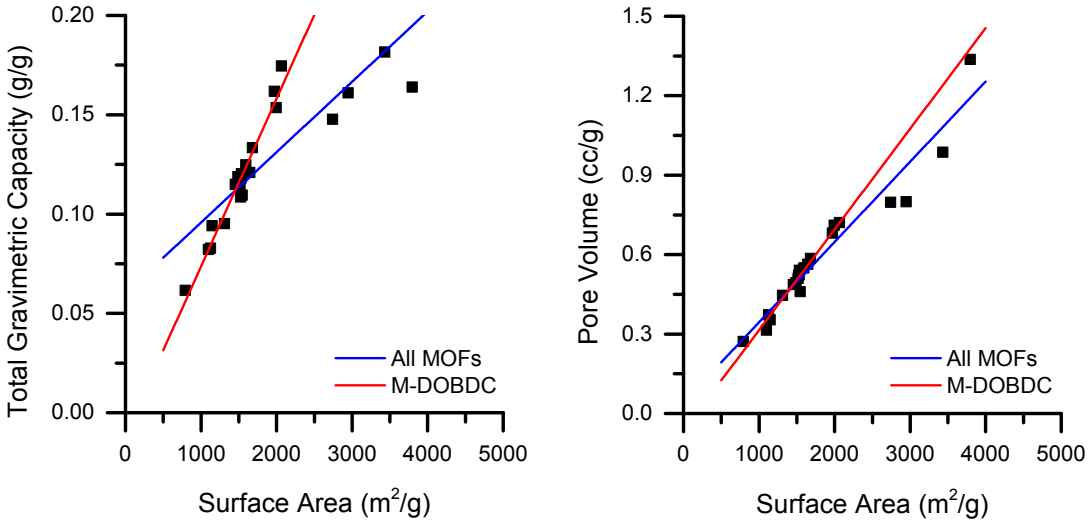

Figure 5.8 Relationship between surface area and (a) total gravimetric CH_4 capacity and (b) MOF pore volume in the M-DOBDC series (red line) and across all MOFs examined in this study (blue line) at P = 35 bar, T = 298 K.

We conclude our discussion by referring to Fig. 5.8, which illustrates trends in gravimetric CH_4 capacity and pore volume *vs*. MOF surface area.[196] Similar trends are well known, for example, in the case of hydrogen storage in porous adsorbents;[164,197] a natural question is whether similar behavior holds for methane, as suggested by a few recent studies.[27,51,175] The existence of such trends would facilitate computational screening[59] based on simple geometric features such as surface area[196] and density. For the MOFs examined here, Fig. 5.8 confirms that a strong linear correlation exists between surface area and either gravimetric capacity (Fig. 5.8(a)) or pore volume (Fig. 5.8(b)) across the M-DOBDC series. However, these correlations become less pronounced when the data set is expanded to include the higher-surface-area compounds (MOF-5, PCN-11,

PCN-14, and HKUST-1). In these cases pore volume remains linearly correlated with surface area, but a similar trend is not observed for the gravimetric capacity. Measurements across a wider set of MOFs would be helpful in clarifying the generality of these trends. Additional analysis of correlations between CH_4 uptake and various MOF properties are presented in Fig. C.7-8 in the Supporting Information.

5.4 CH_4 Adsorption in MOFs Mined from the CSD

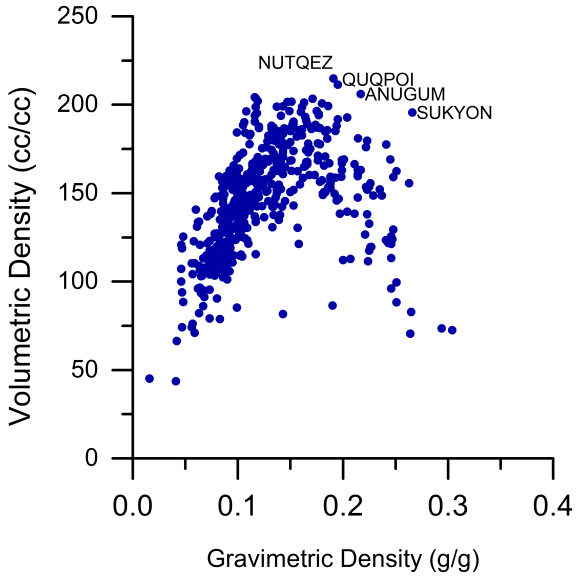

Figure 5.9 Total volumetric and gravimetric density of stored CH_4 in ~600 MOFs mined from the CSD. The CSD identifiers of high-performing MOFs are labled.

Figure 5.9 plots the predicted CH_4 volumetric and gravimetric capacity at 35 bar and 298K for ~600 MOFs mined from the CSD having surface areas greater than 1,000 m^2/g. The distribution of volumetric densities has a concave downward shape. The result is similar to what was observed for H_2 adsorption in MOFs studied by Goldsmith *et al*,[55] and to prior work involving hypothetical MOFs. At gravimetric capacities below ~0.15 g/g, the volumetric and gravimetric CH_4 densities exhibit a linear positive correlation.

However, after ~0.2 g/g, the trend is reversed, such that increasing gravimetric density reduces the volumetric density. For example, the volumetric capacities of the compounds with the highest gravimetric densities (0.3 g/g), XAHQAA (CSD identifier) or CMOF-L4b, is predicted to be only 72.4 cm^3/cm^3, which is the 7th lowest volumetric density amongst the entire dataset of simulated compounds. The concave downward trend can be explained by a correlation between mass density and surface area. That is, MOFs which have high gravimetric uptake typically have extremely large surface areas (Figure 5.9 (b)). Since the mass density of MOFs generally decreases as the surface area increases,[55] density of MOFs having large surface area is extremely low. For instance, referring again to the MOF XAHQAA (which exhibits high a gravimetric density of CH_4), the surface area and mass density of this compound are 6424 m^2/g and 0.17 kg/m^3, respectively. This should be compared to 1168 m^2/g and 1.12 kg/m^3 for YARYEV, respectively, which is a MOF that has similar volumetric CH_4 density (74.1 cm^3/cm^3), but a low gravimetric CH_4 uptake (0.05 g/g).

Further correlation analyses comparing surface area or pore volume and volumetric or gravimetric CH_4 densities are given in Figure 5.10. The surface area and gravimetric CH_4 capacity exhibit a linear relationship, in agreement with experimental results.[27] However, as we discussed, the high gravimetric capacities over 0.3 g/g are typically traded off for lower volumetric capacities (Figure 5.9). Mason et al.[28] argued that volumetric capacity is more important factor than gravimetric capacity in determining the driving range of NG vehicles. Based on the concave downward relationship between surface area and volumetric density, Figure 5.10 (a), the optimal range of surface area for achieving high volumetric densities is 2000-3500 m^2/g. This

range is similar to the range of 2500-3000 m^2/g suggested by screening of hypothetical MOFs by Wilmer *et al*.[51]

Figures 5.10 (c)-(d) analyze the correlation of volumetric and gravimetric CH_4 density with pore volume. Regarding volumetric density, the data shows a concave downward trend similar to what was observed with respect to surface area (Fig. 5.10 (a)). That is, volumetric density is positively correlated with pore volumes less than ~ 1 cc/g. while pore volumes larger than ~1.5 cm^3/g, yield a decrease in volumetric density. Thus, the optimal range of pore volume falls into 1.0 – 1.5 cm^3/g. In contrast to the volumetric density, the relationship between gravimetric density and pore volume follows an increasing trend for all pore volumes. This relationship appears to be comprised of two roughly linear regions: below 2 cc/g the gravimetric density increases rapidly; beyond 2 cc/g the density levels out and increases more slowly.

To identify optimal MOF structures from figure 5.9 we introduce a "score" metric to pinpoint compounds having high volumetric and/or gravimetric densities. This score is defined as

$$score = \frac{V}{349} + \frac{G}{0.5}, \tag{5.1}$$

where V and G are the respective volumetric and gravimetric densities of a given MOF. The values in the denominator are the numerical targets specified by the U.S. DOE for an adsorbent material used in an ANG storage tank. A material that exactly matched both the volumetric and gravimetric targets would achieve a score equal to 2.0

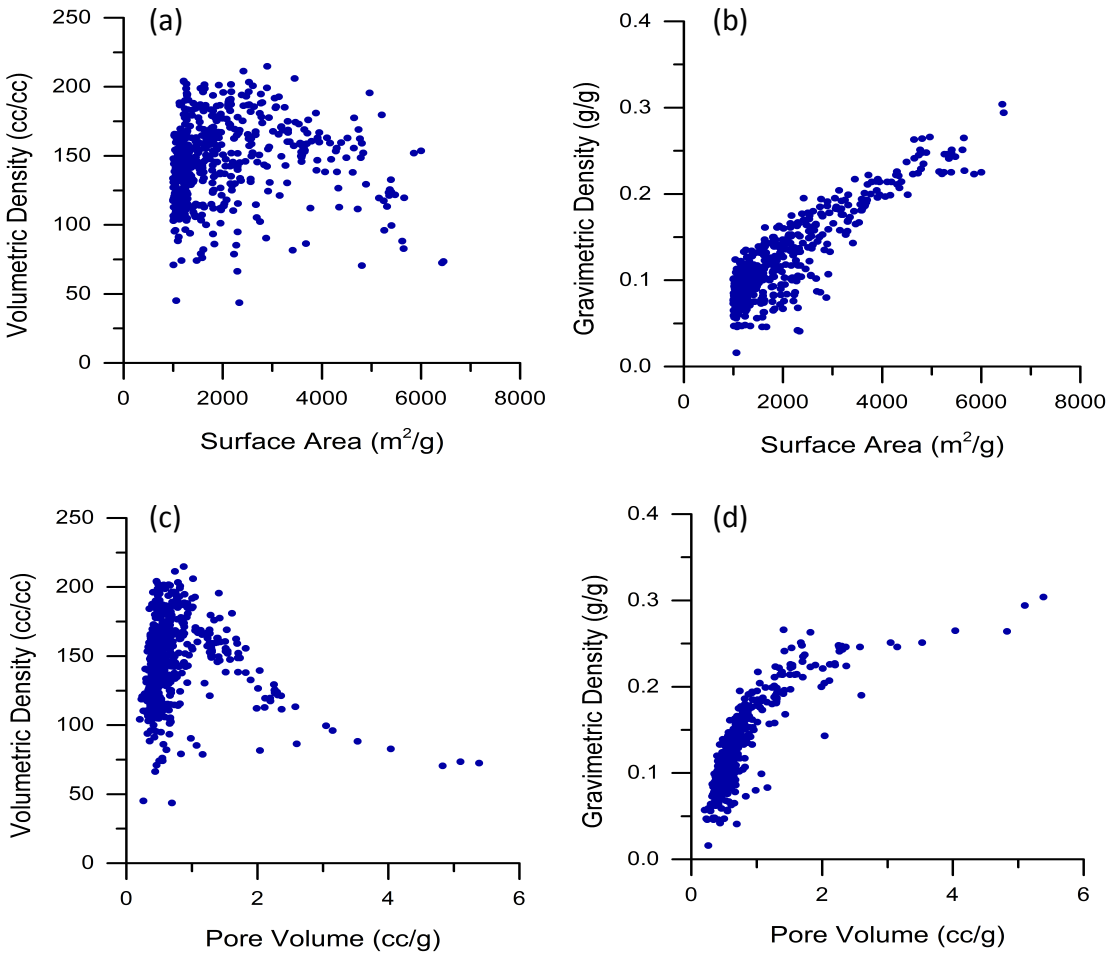

Figure 5.10 Correlation analysis involving several MOF properties: (a) surface area vs. volumetric density, (b) surface area vs, gravimetric density, (c) pore volume vs. volumetric density, and (d) pore volume vs. gravimetric density.

Table 5.4 Highest scoring MOFs as a function of operating conditions

	Best MOFs	Surface Area (m^2/g)	Pore Volume (cc/g)	Volumetric Capacity (cc/cc)	Gravimetric Capacity (g/g)	Score
Total	SUKYON	4964.8	1.41	195.6	0.266	1.09
	ANUGUM	3452.2	1.02	206	0.217	1.02
PS	SUKYON	4964.8	1.41	144.8	0.197	0.81
	OHUKIM	4645.8	1.82	123.4	0.209	0.77
TPS	SUKYON	4964.8	1.41	173.3	0.236	0.97
	DIDDOK	4652.4	1.42	158.6	0.215	0.88

Table 5.4 shows the top two MOFs identified by our screening under both total and usable operating conditions. The MOFs identified include: SUKYON, ANUGUM, OHUKIM, and DIDDOK. The usable conditions examined here are same as previously described: adsorption at 35 bar and 298K, and desorption at 5 bar and 298K (pressure swing, PS) or at 5 bar and 358K (temperature + pressure swing, TPS). The MOF SUKYON has amongst the highest CH_4 storage capacity across all operating scenarios. The crystal structure for this compound is illustrated in Figure 5.11. To our knowledge, there has not yet been an experimental measurement of CH_4 density in SUKYON. However, experimental surface area of this compound is low, 1020 m^2/g,[198] compared to our theoretical estimation, 4577 m^2/g. Possible explanations for the difference are the presence of retained solvent molecules, or a change in the structure (such as pore collapse) after the activation process. Goldsmith *et al*.[55] suggested that advances in experimental activation techniques could result in synthesis of MOF compounds that approach the theoretical surface area, as demonstrated in the case of MOF-5.[55] Thus, we suggest that the simulated surface areas for SUKYON represent a theoretical maximum; if SUKYON could be synthesized in a form that attains this surface area, then we expect that the measured CH_4 capacity would be similar to that from our calculations.

Compared to PCN-11, which yielded the best performance in the previous section, SUKYON exceeds the performance of PCN-11 on both a volumetric and gravimetric basis: SIKYON uptake is 14 cm^3/cm^3 higher volumetrically, and 0.07 g/g higher gravimetrically (PS operation at 35 bar). Considering TPS operation, the volumetric

capacity of SUKYON is comparable to that predicted for Be-DOBDC (within 4 cm^3/cm^3), while the gravimetric capacity is 0.09 g/g higher.

It is also instructive to compare the predicted performance of SUKYON to the measured uptake of Cu-HKUST-1, which holds the record for highest measured CH_4 uptake. We observe that SUKYON surpasses the gravimetric density of Cu-HKSUT-1 by ~0.08 g/g under all operating scenarios. However, Cu-HKUST-1 are nearly identical in volumetric performance: the experimental value for HKUST-1, 227 cm^3/cm^3,[28] is 1-2 cm^3/cm^3, higher than that of SUKYON under both PS and TPS operation. Finally, the performance of SUKYON could be further increased upon metal-substitution of its Cu-paddle-wheel CUS. Moreover, as we describe the next section, the present projection for CH_4 uptake in SUKYON is likely underestimated due to poor treatment of the CH_4-CUS interaction by general interatomic potentials.

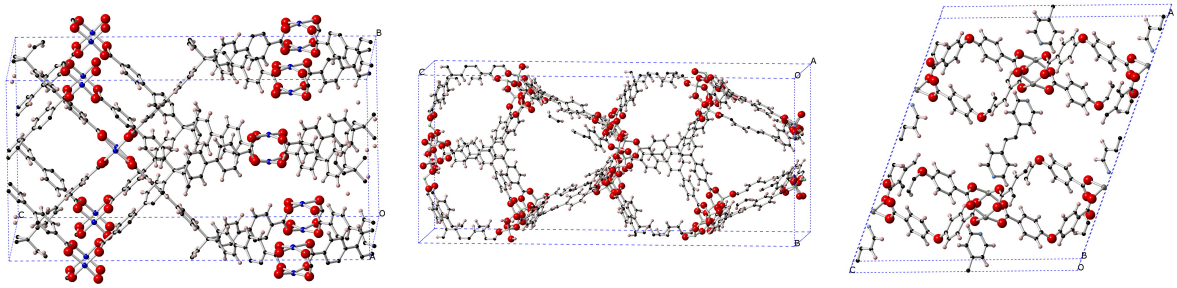

(a) SUKYON (b) OHUKIM (c) DIDDOK

Figure 5.11 Crysral structure of three high-performing MOFs identified by GCMC screening: (a) SUKYON, (b) OHUKIM, and (c) DIDDOK

5.5 Conclusions

We have presented a computational study of the adsorption thermodynamics, electronic structure, and methane storage capacity in MOFs. Compounds examined include 18 metal-substituted variants of M-DOBDC, as well as several other prominent MOFs, including: MOF-5, PCN-11/14, and HKUST-1. Important aspects of our study include: (*i*) the benchmarking of Van der Waals density functionals for prediction of ΔH; (*ii*) assessment of common interatomic potentials for predicting CH_4 uptake; (*iii*) estimation of *usable* methane capacity under likely operating conditions, and (*iv*) clarification of the role of enhanced binding sites in CH_4 storage.

Regarding thermodynamic properties, methane adsorption enthalpies on the benchmark Mg- and Ni-DOBDC systems were calculated using several vdW-DFT methods and compared against experimental data. The vdW-DF2 scheme was found to yield the best agreement with experiments, with a small mean absolute deviation (MAD) of 3.7 kJ/mol. Applying this formalism across the entire M-DOBDC series, we observe that ΔH varies from -16 to -34 kJ/mol, and weakly correlates with the ionic radius of the CUS. The calculated enthalpies are 10-20 kJ/mol less exothermic than for CO_2 adsorption in the same M-DOBDC compounds, suggesting that CH_4 adsorption in MOFs is dominated by weaker dispersion interactions. This assertion is supported by analysis of the charge density redistribution upon adsorption in Mg-DOBDC, which showed significantly less polarization in adsorbed CH_4 compared to prior studies on CO_2.

In addition to these thermodynamic analyses, CH_4 adsorption isotherms were evaluated using GCMC and compared against experimental data for 9 prototype MOFs. The performance of 6 common inter-atomic potentials was critically assessed, taking into

account variations in the description of the CH_4 molecule and the framework atoms. Of the various models considered, the uncharged, single-site TraPPE model for CH_4 in combination with a mixed DREIDING/UFF description for the MOF atoms yielded the best agreement with experiments, with a MAD of 15 cm^3/cm^3 at 298 K and pressures up to 35 bar.

The optimal potential was then used to predict the *usable* CH_4 capacities for isothermal pressure swing (PS) and temperature + pressure swing (TPS) operating scenarios. Significant differences exist between *total* capacities and less-frequently-reported *usable* capacities, with the usable capacities falling significantly below the (hypothetical) total capacities. We suggest that future studies of methane storage give less emphasis to total capacities in favor of reporting usable capacities, which should more closely resemble the performance of a realistic storage system. In our calculations Be-DOBDC, PCN-11, and MOF-5 emerge as the MOFs having the best combination of usable gravimetric and volumetric CH_4 densities. For pressure swing operation, PCN-11 yields the best performance at pressures below approximately 50 bar (130 cm^3/cm^3 & 0.13 g/g at 35 bar), while MOF-5 is best at higher pressures (168 cm^3/cm^3 & 0.21 g/g at 65 bar). Due to their tendency to retain CH_4 at low pressures, enhanced binding sites such as CUS or pocket sites are deemed to be detrimental for PS operation at higher pressures.

Finally, the CH_4 capacities of ~600 MOF structures previously mined from the CSD were calculated in a high-throughput fashion. A trade-off between volumetric and gravimetric CH_4 capacities was identified, similar to what has been observed in screening of hypothetical MOFs. Of the MOFs screened, the compound with CSD identifier "SUKYON" is predicted to exhibit the best performance under all operating conditions

considered. Due to limitations in the interatomic potentials used for our screening analysis, we hypothesize that the actual uptake of SUKYON is underestimated in our calculations. Metal-substitution of CUS in SUKYON may also result in additional improvements in its uptake. These two issues are explored in more detail in the next chapter for M-HKUST-1; they also serve as a possible extension of this work in the future.

Chapter 6

Parameterization of Interatomic Potentials for CH_4 Adsorption in M-HKUST-1

6.1 Introduction

As we discuss previous chapter, gas uptake is predicted using Grand Canonical Monte Carlo (GCMC), typically employing general, or "off the shelf," interatomic potentials such as the Drieding[127] or Universal Force Field.[128] (For a review summarizing the status of force fields in nano-porous materials see Ref. 199) These potentials can accurately reproduce the experimental CH_4 isotherms in the subset of MOFs where CUS are absent, such as in MOF-5.[200] Also, it has reasonable accuracy in M-DOBDC. However, as demonstrated by Wu *et al.*[62] and Getzchmann *et al.*,[63] general force-fields fail to properly reproduce CH_4 interactions with CUS in Cu-HKUST-1. This leads to poor agreement with diffraction experiments: these measurements indicate that CUS are preferred sites for CH_4 adsorption, whereas GCMC with general potentials predicts almost no adsorption at these sites, Figure 6.1(a). The poor description of the Cu-CH_4 interaction typical of these potentials results in an underestimation of CH_4 uptake that scales with the number of CUS sites.[201] This is unfortunate, as CUS-containing MOFs are amongst the most promising compounds known for gas capture and storage.[27,28] It is

therefore likely that screening studies that do not account for CH_4-CUS interactions will underpredict uptake in those systems, leading to "false negatives" in the results. The poor predictive capability of general potentials has prompted the development of force-fields that aim to capture CUS-adsorbate interactions within a subset of existing MOFs.[199] For example, Chen *et al.*[179] proposed a MMSV (Morse-Morse-Spline-van der Waals) potential to describe CH_4 adsorption in HKUST-1 at low temperature and pressure. Similarly, potentials describing CO_2 adsorption in three M-DOBDC variants (M= Mg, Fe, and Zn) have been reported.[202-204]

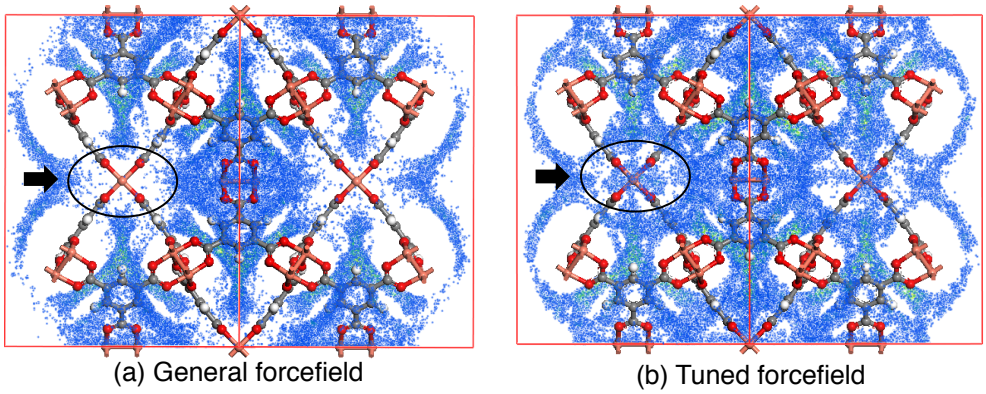

Figure 6.1 Predicted CH_4 density distribution (blue points) in the Cu-HKUST-1 unit cell at 5 bar and 298K from GCMC simulations using: (a) a general interatomic potential (Universal Force Field) and (b) a force-field tuned to reproduce the Cu-CUS/CH_4 interaction. Black ovals/arrows highlight adsorption sites in the vicinity of the Cu paddle wheel.

In the present chapter we develop a set of customized interatomic potentials that describe CH_4 adsorption in the M-HKUST-1 series of MOFs. The potentials are subsequently applied to screen for metal-substituted M-HKUST-1 compositions that could outperform Cu-HKUST-1 in terms of CH_4 storage capacity. The potentials were initially developed and validated for Cu-HKUST-1 by fitting a simple Morse potential to van der Waals-aware density functional theory calculations (vdW-DF2 functional)[112] of

CH_4-Cu CUS binding energies. Transferability of the potential to other Cu-containing MOFs with CUS such as PCN-11 and PCN-14 was confirmed by assessing the potential's ability to reproduce measured CH_4 adsorption isotherms. The potential fitting was subsequently extended to 17 additional metal-substituted variants of M-HKSUT-1. Simulated isotherms using the tuned potentials suggest that M-HKUST-1 with M = Ca or Fe should exceed the performance of Cu-HKUST-1 under practical (i.e., usable) operating conditions. These compositions are suggested as synthetic targets for further experimental scrutiny.

6.2 Methods

Our calculations treat the CH_4 molecule within the single site approximation; a 12-6 potential form was used to describe interactions between CH_4 molecules using TraPPE[129] parameters; CH_4 interaction parameters with C, H, and O atoms within the MOF were adopted from the UFF.[128] Prior studies[51,201] have shown that general force-fields such as DREIDING[127] and UFF[128] provide reasonable estimates of CH_4 uptake in MOFs that do not contain CUS; for example, Figure D.1 shows the good agreement between calculated (UFF) and measured CH_4 isotherms for MOF-5,[200] which does not contain CUS.

However, as previously described, general force fields do correctly capture CH_4-CUS interactions. This effect is illustrated in Fig. 6.2, which shows that a general potential based on the UFF significantly underestimates the interaction strength between CH_4 and the Cu CUS in the paddle-wheel cluster of HKUST-1. A consequence of this

"missing interaction" is the under prediction of CH_4 uptake shown by the calculated (UFF) isotherm in Fig 6.3.

This deficiency of the general potentials was addressed by developing a customized CH_4—metal interatomic potential using a simple Morse form.

Our force-field parameterization scheme is based on fitting to CH_4-CUS interaction energies from van der Waals-augmented[102] Density Functional Theory (DFT)[86] calculations on the periodic M-HKUST-1 primitive cell (156 MOF atoms). Prior calculations using this method yielded enthalpies of CH_4 adsorption in very good agreement with experiments.[201] A minimum of 7 configurations along a direction perpendicular to the metal-O plane in the Cu paddle wheel (see inset of Fig. 6.2) was used in the fit. Calculations were performed in a spin-averaged configuration given that prior calculations[183] have found that magnetism associated with the CUS impacts adsorption energies by less than 1 kJ/mol (See Table D.1). K-point sampling was performed at the Gamma point, and the planewave cutoff energy was set to 500 eV. All DFT calculations were performed with the VASP[113,114] code.

The Cu-CH_4 Morse interaction parameters were fit to the energy/configuration pairs from DFT using the non-linear fitting routines implemented in GULP.[205] All three metal-CH_4 parameters were fitted simultaneously with the constraint that all other CH_4-MOF and CH_4-CH_4 interaction parameters were fixed at their respective UFF and TraPPE values. The accuracy of the fitted parameters was assessed by evaluating the mean absolute derivation (MAD) from the DFT binding energy curve and from the experimental CH_4 isotherm. (The resulting force field for Cu-HKUST-1 was also checked for transferability by predicting isotherms in other MOFs containing Cu-paddle wheel

clusters, such as PCN-14 and PCN-11.) Finally, this procedure was repeated for each of the other 17 metals considered for substitution in M-HKUST-1.

6.3 Results

6.3.1 Interatomic Potential for M-HKUST-1

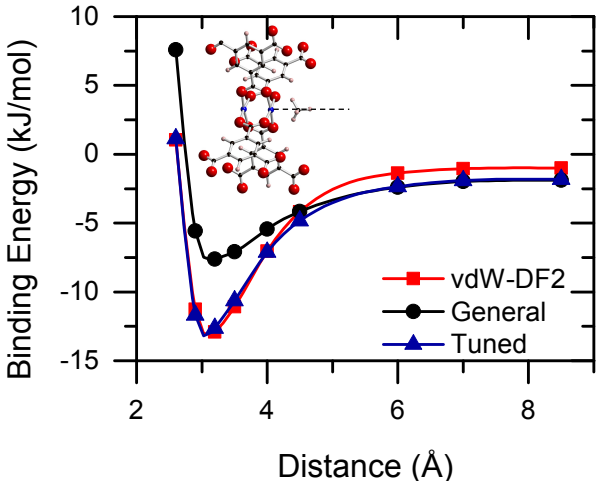

Figure 6.2 Cu-CH_4 binding energy as a function of CH_4-Cu distance in Cu-HKUST-1. Red squares: reference energies calculated from vdW-DF2 calculations on the HKUST-1 primitive cell; Black circles: an "off the shelf" potential based on the Universal Force Field; Blue triangles: customized potential obtained by fitting to vdW-DF2 calculations. The inset illustrates the direction of the CH_4 molecule's approach to the Cu CUS used to generate the binding energy curves.

Figure 6.2 shows the CH_4-Cu binding energy (BE) curves for Cu-HKUST-1 calculated with vdW-DF2, the general UFF force-field, and the tuned force-field. Compared with the vdW-DF2 BE curve, the general force-field underestimates the depth of the minimum energy configuration by nearly 50% due to a CH_4-Cu interaction which is too weak. The deviation between these models is smaller at larger separations, with the general potential now slightly overbinding relative to the vdW-DF2 data. In contrast,

the tuned potential reproduces well the DFT binding energies near the potential minimum. For this potential the mean absolute deviation (MAD) is only 0.5 kJ/mol. This should be compared with the general potential, whose MAD is much larger, 3.1 kJ/mol. The tuned potential also exhibits some slight overbinding at larger separations, however, as shown below, these features do not appear to negatively impact the predicted isotherms. While a function with a more flexible form (i.e., having more fitting parameters) could in principle yield a better fit over the full range of interaction distances,[179] we prefer a simple model which can be rapidly adapted to explore many distinct MOF compositions. Additional comparisons between the tuned potential and DFT binding energies at different positions near the Cu-CUS (without additional fitting) are provided in Figure D.2. Parameters for the tuned potential are tabulated in table D.2.

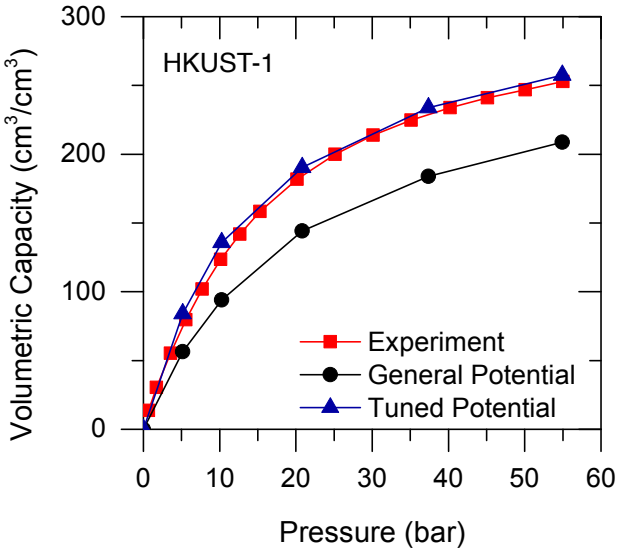

Figure 6.3 Comparison of the experimental CH_4 total volumetric isotherms (Ref. 28) in HKUST-1 at 298 K (red curves) with isotherms calculated using either the tuned interatomic potential (blue curves) or the Universal Force Field (General Potential, black curves).

Figure 6.3 compares the calculated CH_4 uptake isotherms from both the general and tuned potentials with experimental data for Cu-HKUST-1 from Mason *et al.*[28] It is

evident that the uptake estimated from the tuned potential compares very well with the experimental data: the MAD averaged over the pressure range of 5-55 bar is only 7 cm^3/cm^3. In contrast, the general potential underestimates the experimental data across the entire pressure range. We attribute this discrepancy to the "missing interaction" between CH_4 and the Cu CUS typical of general potentials. Finally, Figure D.3 demonstrates that our tuned potential (optimized only for Cu-HKUST-1) also can reproduce the experimental CH_4 isotherms for other MOFs containing Cu paddle wheel SBUs, such as PCN-14 and PCN-11. These results suggest that the potential may be transferable to other systems having similar CUS geometries; additional analysis of the transferability of the present potentials is planned for a future publication.

The tuned potential also appears to yield a more reliable description of CH_4 adsorption at the CUS sites, as can be seen by comparing panels (a) and (b) of Fig. 6.1, which illustrates the density of adsorption sites in Cu-HKUST at P = 5 bar and T = 298 K. As previously mentioned, the general potential used to generate Fig. 6.1(a) does not identify CUS as a preferential adsorption site, in disagreement with diffraction studies.[62,63] In contrast, the tuned potential exhibits a much higher density distribution in the vicinity of the Cu CUS, Figure 6.1 (b). Given the improvements in uptake and site preference that can be achieved with the tuned potential, we proceeded to apply a similar fitting strategy to generate new potentials and estimate CH_4 capacity across the remainder of the M-HKUST-1 series. Parameters for the new potentials for all metal substitutions M are given in Table D.3; Figure D.4 provides comparisons between the binding energy curves derived from DFT, the tuned potential, and a representative general potential.

6.3.2 CH_4 Adsorption in M-HKUST-1

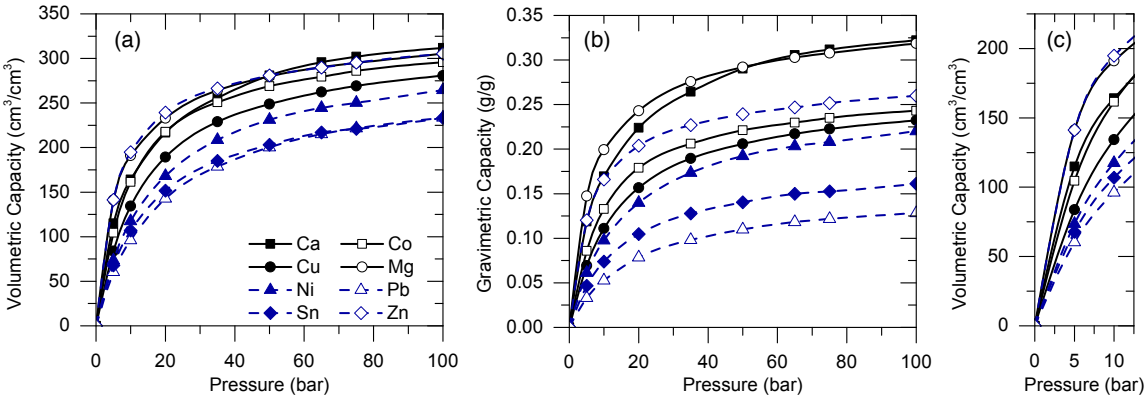

Figure 6.4 (a) Total volumetric (cm^3 at STP/cm^3 MOF) and (b) gravimetric storage densities (g CH_4/g MOF) for CH_4 in selected M-HKUST-1 compounds predicted by GCMC simulations using the tuned interatomic potentials. Panel (c) is a magnification of panel (a) that shows the isotherms near the 5 bar minimum pressure used to estimate usable capacities.

Figure 6.4 shows the total volumetric and gravimetric CH_4 adsorption isotherms for selected compositions within the M-HKUST-1 series for pressures up to 100 bar. (Here "total" refers to the full amount of CH_4 stored in the MOF as both adsorbed and gas-phase CH_4. Volumetric densities assume a single crystal density of the MOF, and therefore serve as an upper bound to the density in a practical system that would employ the MOF media in powder or densified form.[206,207]) A complete tabulation of total and usable capacities across all 18 M-HKUST-1 MOFs is provided in Table 6.1 and Table D.4. Usable capacities were evaluated both for pressure swing (PS) and temperature-pressure swing (TPS) scenarios. Desorption conditions were set at 5 bar and

Table 6.1 Predicted CH_4 storage capacities and metal-site adsorption energies (ΔE) as a function of metal composition in M-HKUST-1. Capacities are reported for two maximum operating pressures (P_{max} = 35 and 65 bar, T = 298 K). In addition, usable capacities are reported for two desorption scenarios: isothermal pressure swing (PS) to P_{min} = 5 bar, and temperature + pressure swing (TPS) to P_{min} = 5 bar, T = 323 K. Capacities for P_{max} = 100 bar are given in the Appendix D.

M	ΔE kJ/mol	P_{max} = 35 bar						P_{max} = 65 bar					
		Total		Usable (P_{min} = 5 bar)				Total		Usable (P_{min} = 5 bar)			
		298 K		PS (298 K)		TPS (323 K)		298 K		PS (298 K)		TPS (323 K)	
		cc/cc	g/g	cc/cc	g/g	cc/cc	g/g	cc/cc	g/g	cc/cc	g/g	cc/cc	g/g
Be	-17	224	0.22	127	0.13	156	0.16	260	0.26	163	0.16	191	0.19
Ca	-18	256	0.26	141	0.15	175	0.18	296	0.31	181	0.19	215	0.22
Co	-16	251	0.21	146	0.12	179	0.15	280	0.23	175	0.14	208	0.17
Cr	-12	229	0.21	146	0.13	171	0.15	262	0.24	179	0.16	205	0.18
Cu	-14	229	0.19	145	0.12	171	0.14	262	0.22	179	0.15	205	0.17
Fe	-15	243	0.21	151	0.13	180	0.15	274	0.23	182	0.15	211	0.18
Mg	-27	264	0.28	123	0.13	166	0.17	290	0.30	149	0.16	192	0.20
Mn	-14	250	0.21	148	0.13	180	0.15	280	0.24	178	0.15	210	0.18
Mo	-11	225	0.18	145	0.11	170	0.13	260	0.20	179	0.14	205	0.16
Ni	-10	209	0.17	135	0.11	156	0.13	244	0.20	171	0.14	192	0.16
Pb	-5	179	0.10	118	0.06	136	0.07	215	0.12	155	0.09	173	0.09
Sc	-6	214	0.21	133	0.13	157	0.15	248	0.24	168	0.16	192	0.18
Sn	-4	185	0.13	117	0.08	138	0.10	217	0.15	149	0.10	170	0.12
Sr	-18	244	0.21	149	0.13	180	0.15	278	0.24	183	0.16	214	0.18
Ti	-9	222	0.20	138	0.13	163	0.15	255	0.23	171	0.16	196	0.18
V	-10	211	0.19	139	0.13	160	0.15	248	0.23	176	0.16	197	0.18
W	-11	230	0.13	144	0.08	170	0.10	264	0.15	178	0.10	204	0.11
Zn	-24	266	0.23	125	0.11	171	0.15	290	0.25	148	0.13	194	0.17

298K for PS operation; 5 bar and 323 K (50°C) were used for TPS. Three different values are examined as maximum pressure limits for gas adsorption, P_{max} = 35, 65, and 100 bar.

Regarding total capacities, Table 6.1 shows that volumetric and gravimetric capacities vary widely across the M-HKUST-1 series, ranging from 179 to 266 cm^3/cm^3 and 0.1 to 0.26 g/g at 35 bar. The highest uptake capacities at 35 bar are projected for M = Mg and Zn, with respective CH_4 densities of 264 cm^3/cm^3, 0.28 g/g, and 266 cm^3/cm^3, 0.23 g/g. These values are comparable to those of the best-performing hypothetical MOFs identified by Wilmer *et al.*[51] Incidentally, Mg and Zn are also the two metals for which the calculated CH_4-CUS adsorption energy (ΔE) is largest, Table 6.1, suggesting a correlation between total capacity and adsorption enthalpy. In addition to these two

compositions, our screening identifies 5 additional substitutions that out-perform Cu-HKUST-1 on both a volumetric and gravimetric basis. These include M = Ca, Co, Fe, Mn, and Sr. At higher pressures Ca overtakes Mg as the highest-performing M-HKUST-1 variant, with capacities of 296 cm^3/cm^3 & 0.31 g/g at 65 bar, and 312 cm^3/cm^3 & 0.32 g/g at 100 bar.

Regarding usable capacities, the highest-performing compositions at moderate pressures (35 and 65 bar) include Fe and Mn from the transition metal series, and Sr and Ca from the alkaline earths. This ordering is largely maintained regardless of whether PS or TPS operation is assumed. The performance of Ca-HKUST-1 is noteworthy for its high gravimetric capacity (25-29% higher than for Cu-HKUST-1), a result that follows directly from its low atomic mass. Despite their high total capacities, Mg and Zn are absent from the list of high-capacity compositions when ranked according to usable capacity. (In fact, Mg and Zn-HKUST-1 generally perform worse than Cu-HKUST-1 under usable conditions.) This can be explained by the high CH_4 uptake exhibited by these compositions at lower pressures (Figure 6.4c), which arises from their relatively strong CH_4-CUS interactions of -24 to -27 kJ/mol. Additional plots of usable capacity as a function of pressure and desorption temperature are given in Figs. D.5 and D.6.

Can the alternative M-HKUST-1 compositions suggested here be realized experimentally? In this regard we point to several recent experiments that have synthesized HKUST-1 variants with M = Cr[70], Mo[74], Ni[71], Ru[73], Fe[208], and Zn.[72] While some challenges have been encountered with activation of Fe-, and Zn-HKUST-1,[72,75] new activation techniques may hold promise for realizing these, and other, compositions.[209] To our knowledge, CH_4 adsorption measurements have not been

performed on these MOFs. Our results suggest that additional experimental effort should be devoted to the synthesis and testing of compositions having M = Fe, Mn, Ca and Sr.

6.4 Conclusions

We have developed a new set of interatomic potentials describing CH_4 adsorption across the M-HKUST-1 series of MOFs. The potentials explicitly account for interactions between methane and coordinatively unsaturated metals sites, M = Be, Ca, Co, Cr, Cu, Fe, Mn, Mg, Mo, Ni, Pb, Sc, Sn, Sr, Ti, V, W, and Zn. This interaction is poorly described by existing general potentials, leading to inaccurate predictions of the preferred adsorption sites, and an underprediction of uptake by simulated isotherms. The new potential assumes a simple Morse functional form, and is constructed by fitting to van der Waals-informed density functional calculations (vdW-DF2 functional). Testing on the benchmark Cu-HKUST-1 system revealed that the tuned potential yields a methane uptake isotherm in excellent agreement with the most recent experimental measurements. Furthermore, the potential shows promise for transferability to other MOFs containing paddle-wheel clusters, such as PCN-11 and PCN-14.

The new potentials were applied to screen the M-HKSUT-1 series for compositions that could exceed the CH_4 storage density of Cu-HKUST-1, which currently holds the record for highest methane storage density amongst experimentally tested materials. Our screening suggests that compositions with M = Ca and Fe should exceed the performance of Cu-HKUST-1 under usable operating conditions. These compositions are suggested as promising targets for experimental synthesis and characterization.

Chapter 7

Conclusions

The discovery of efficient adsorbent materials would enable two technologies aimed at reducing carbon emissions. These include: carbon capture (and subsequent sequestration) from the flue gasses of fossil-fuel-based power plants and the on-board storage of natural gas for natural gas vehicles. Capturing anthropogenic CO_2 emissions from the combustion of fossil fuels would help to mitigate the impact of climate change. Also, the widespread adoption natural gas as a vehicular fuel could reduce reliance on imported petroleum and further minimize CO_2 emissions compare to gasoline. Both of these applications stand to benefit from the development of a robust, high-capacity adsorbent material. The discovery of such a compound has been the focus of this dissertation.

Metal Organic Frameworks (MOFs) are promising candidates for gas capture and storage due to their high surface areas and tunable properties. This tunability allows for a building block approach to MOF synthesis, which has resulted in literally thousands of MOF candidates. The large number of MOFs suggests that experimental synthesis and testing of all compounds is impractical. Therefore the strategy pursued in this research

has been to predict MOF properties computationally, in presumably a fraction of the time needed to conduct comparable experiments.

A primary focus of our study has been to reveal the properties of metal-substituted MOFs based on the prototypes Ni-DOBDC and HKUST-1. The compounds yield the best CO_2 and CH_4 capacities under operating conditions typical for flue gas capture (CO_2 pressures less than 1 bar) and for vehicle applications (moderate CH_4 pressures of 35 -100 bar). Our calculations explore the possibility for additional performance tuning within this series of compounds by screening 36 metal-substituted variants (M-DOBDC and 18 M-HKUST-1) with respect to their CO_2 adsorption enthalpies and CH_4 capacities. Here M refers to a coordinatively unsaturated metal site having the composition Be, Ca, Co, Cr, Cu, Fe, Mn, Mg, Mo, Ni, Pb, Sc, Sn, Sr, Ti, V, W, and Zn. In addition to this composition search, we explore approximately 600 additional MOFs mined from the CSD as possible CH_4 adsorbents. Our computational approach predicts several properties relevant for gas capture and storage: adsorption thermodynamics, structure, bonding nature, and capacities. This is accomplished by combining simulation techniques ranging from classical Grand Canonical Monte Carlo to quantum mechanical calculations based on dispersion-corrected Density Functional Theory. In some cases a multi-scale approach is employed in which interatomic potentials used for isotherm predictions are parameterized using first principles calculations of MOF/adsorbate interactions.

7.1 Carbon Capture

As an initial step in our research we validated various vdW-DFT methods for predicting the thermodynamics of CO_2 adsorption. In particular, we compared the adsorption enthalpies for CO_2 on Mg, Ni, Co-DOBDC, and Cu-HKUST-1 using 6 different vdW-DFT methods. We find that the revPBE-vdW functional (also known as vdW-DF1) yields very good agreement with experimental data, with a mean absolute deviation (MAD) of ~2 kJ/mol (4%). This is an important observation, as it implies that the thermodynamics of CO_2 adsorption can be calculated with efficient density functional techniques that account for the full periodicity of the MOF crystal structure. These techniques could therefore supplant the conventional approach of using expensive quantum-chemical based methods that require a cluster approximation to the MOF structure. Based on these findings the vdW-DF1 functional was adopted for subsequent CO_2 affinity calculations.

Building on these benchmarking studies, we next screened 18 M-DOBDC and 18 M-HKSUT-1 compounds. Our calculations identify relatively large exothermic adsorption enthalpies for substitutions involving alkaline earth metals (Mg, Ca, and Sr) in both M-HKUST-1 and M-DOBDC, and for the early transition metals (Sc, Ti and V) in M-DOBDC. We find that CO_2 adsorption enthalpies for 8 M-DOBDC (Mg, Ca, Sr, Sc, Ti, V, Mo, and W), and 5 M-HKUST-1 (Be, Mg, Ca, Sr, Sc) variants fall into the optimal enthalpy range (-40 kJ/mol $\leq \Delta H \leq -75$ kJ/mol) for CO_2 capture from flue gasses or via direct air capture. Additionally, an analysis of the electronic structure of the CO_2/MOF interaction demonstrates that electrostatic interactions comprise a significant portion of the MOF-CO_2 bond. As a consequence, a strong correlation is observed between the

partial charges on the coordinatively unsaturated metal sites and the adsorption enthalpy. It is therefore suggested that the partial charge on the metal can be used as a simple descriptor for CO_2 affinity, with those MOFs having metal charges larger than +1.4 falling within the optimal enthalpy range

7.2 Natural Gas Storage

In the case of natural gas storage, CH_4 adsorption affinities across 18 M-DOBDC variants were found to be 10-20 kJ/mol weaker than for CO_2 adsorption in the same compound. This result suggests that weaker van der Waals interactions are the dominant contribution to CH_4-MOF adsorption energies. Charge density redistribution analyses confirm that the polarization in adsorbed CH_4 is significantly less than in adsorbed CO_2, consistent with the absence of a quadruple moment in CH_4.

CH_4 storage capacities were determined using GCMC calculations in M-DOBDC and M-HKUST-1, with additional comparisons to prominent MOFs such as MOF-5, PCN-11, and PCN-14. The generic Dreiding + TraPPE force-field was determined to yield the best accuracy with experimental isotherms based on a comparison with several interatomic potentials taken from the literature. However, these and other "off-the-shelf" potentials cannot accurately reproduce CUS-CH_4 interactions in Cu-HKUST-1, prompting us to develop a new tuned potential for MOFs which contain CUS in a paddle-wheel geometry. The new potentials were constructed by parameterizing to vdW-DF2 reference binding energies. The new potential was validated for Cu-HKUST-1, and then extended to calculate CH_4 capacities of 17 other compositional variants in M-HKUST-1. In addition to predicting the total capacity, we estimate usable capacities under realistic

operating scenarios: isothermal pressure swing (PS) and temperature-pressure swing (TPS). The calculated capacities reveal that Ca & Fe-HKUST-1 should surpass that of Cu-HKUST-1, which currently holds the record for highest measured CH_4 capacity. These MOFs are suggested as promising targets for experimental synthesis and characterization.

Finally, we expanded our screening for CH_4 capacities to another ~600 MOF structures mined from the CSD. The volumetric and gravimetric capacities of these MOFs exhibit a concave downward relationship, similar to what has been observed in the screening of hypothetical MOFs, indicating a trade-off between volumetric capacity and gravimetric capacity. The screening further reveals that the compound SUKYON yields the best performance under all operating conditions. Although we these calculations employed a generic force-field, the volumetric capacities are found to be comparable to the measured values of Cu-HKUST-1. Since SUKYON contains Cu-paddlewheel CUS, it is a good candidate for further study using the tuned interatomic potential (which likely will result in a more accurate, and presumably higher calculated uptake). It may also be an attractive compound for metal-substitution studies.

7.3 Outlook and Next Steps

Looking to the future, there are several ways to expand on the present study. For carbon capture, estimating usable capacities of CO_2 would be an important, but challenging, next step. Our present work in this area has employed DFT calculations to predict the thermodynamics of CO_2 adsorption. Capacities could be predicted using

GCMC calculations, however, the more complicated interaction between polarizable CO_2 and a given MOF presents challenges for generic force-fields.[199] It is therefore likely that potential fitting will be needed to make accurate predictions of CO_2 uptake.

In addition, several other MOF properties should be investigated, including: selectivity for CO_2 with respect to N_2 and other flue gas components, hydrothermal stability, and the effects of SO_x and NO_x.

For CH_4 storage, building from our success in predicting uptake in M-HKUST-1, a natural extension would be to apply our customized interatomic potentials to other CUS-containing MOFs. As a first step, uptake in all MOFs containing the Cu-paddle-wheel structure, with suitable substitutions of other metals on the Cu site, could be explored. Such a search would involve more than a hundred compounds. Of special interest within this set would be metal-substituted structures based on PCN-14, PCN-11, and SUKYON. PCN-11 was predicted to exhibit better performance than Cu-HKSUT-1 when using the generic force-fields described in chapter 5. Also, PCN-14 was the previous experimental record holder in CH_4 capacity. Finally, from our CSD screening, we identified the SUKYON as a promising material.. All of these compounds (and several others with the same paddle-wheel geometry) could be explored by combining metal substitution with our customized potential.

Appendices

Appendix A. Supporting Information for Compare Various vdW-DFT Methods for Carbon Capture

Table 0.1 Emperical dispersion parmeters used in the semi-empirical DFT-D2 calculations

Element	C_6 (in Jnm^6mol^{-1})	R_0 (in Å)
H	0.14	1.001
C	1.75	1.452
O	0.70	1.342
Mg	5.71	1.364
Co	10.80	1.562
Ni	10.80	1.562
Cu	10.80	1.562

Table 0.2 Convergence of CO_2 binding energies at 0K in KJ/mol as a function of k-point sampling density. All calculations employed the revPBE-vdW functional.

System	Mesh	ΔE
Mg/DOBDC	1 × 1 × 1	-50.89
	2 × 2 × 2	-51.20
	3 × 3 × 3	-51.19
Cu-HKUST-1	1 × 1 × 1	-27.33
	2 × 2 × 2	-27.34
	3 × 3 × 3	-27.38

Table 0.3 Lattice constants (Å) and unit cell volume (Å^3) for MOFs with and without adsorbed CO_2.

System	Type	Method	a	c	V
Mg/DOBDC	MOF	LDA	25.7317	6.8090	3904.38
		GGA	26.1234	6.9324	4097.08
		revPBE-vdW	26.0619	7.0939	4172.81
		Expt.[60]	26.0200	6.7210	3940.75
		Expt.[162]	25.9210	6.8625	3993.50
	MOF+CO_2	LDA	25.6558	6.8160	3885.37
		GGA	26.0935	6.9645	4106.66
		revPBE-vdW	26.1370	7.01675	4151.23
		Expt.[61]	25.8810	6.8989	4001.96
		Expt.[162]	25.8240	6.8904	3979.40
Ni/DOBDC	MOF	GGA	25.8898	6.79441	3944.02
		revPBE-vdW	25.6747	7.02715	4011.63
		Expt.[147]	25.7856	6.77010	3898.34
	MOF+CO_2	GGA	25.9468	6.79464	3961.53
		revPBE-vdW	25.9284	6.91467	4025.83
		Expt[155]	25.7836	6.74740	3884.70
Co/DOBDC	MOF	LDA	25.7673	6.6934	3848.71
		GGA	25.1592	6.8902	4083.30
		revPBE-vdW	26.1318	7.1222	4211.98
		Expt[148]	26.1102	6.7192	3967.10
Cu-HKUST-1	MOF	LDA	25.994		17563.80
		GGA	26.4825		18572.70
		revPBE-vdW	26.8211		19294.40
		Expt[69]	26.343		18280.00
	MOF+CO_2	LDA	26.0291		17635.10
		GGA	26.5116		18634.00
		revPBE-vdW	26.7780		19201.50
		Expt[61]	26.2979		18187.09

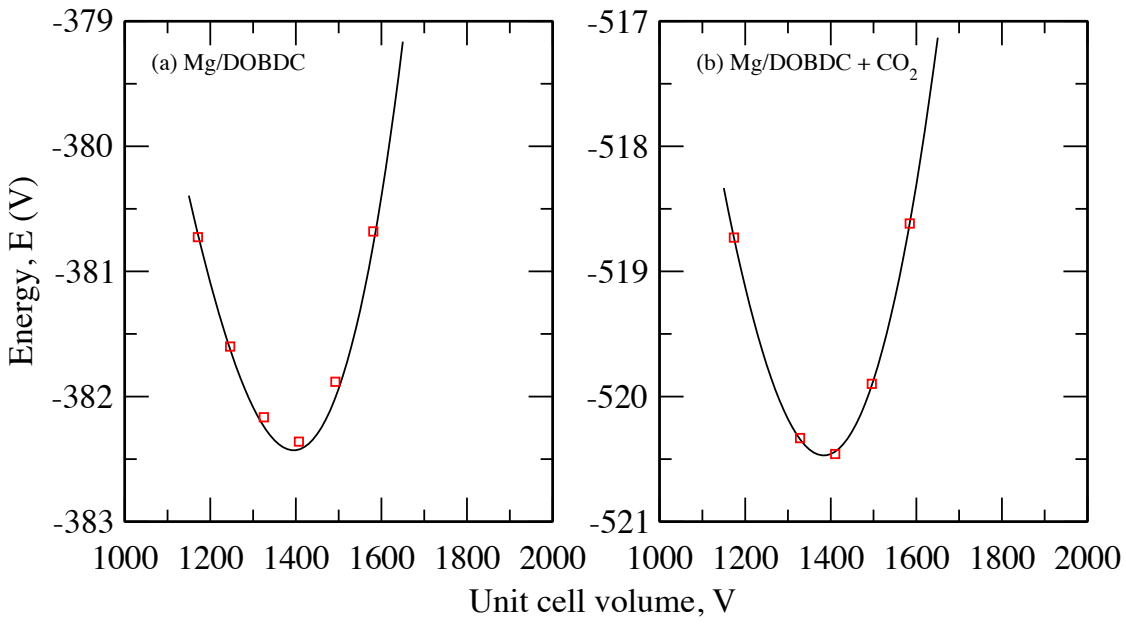

Figure 0.1 Variation of total energy (eV) with respect to unit cell volume ($Å^3$) for Mg/DOBODC with and without CO_2, fitted to Muraghan equation. The left (a) and right (b) panels are for MOF and MOF with adsorbed CO_2, respectively.

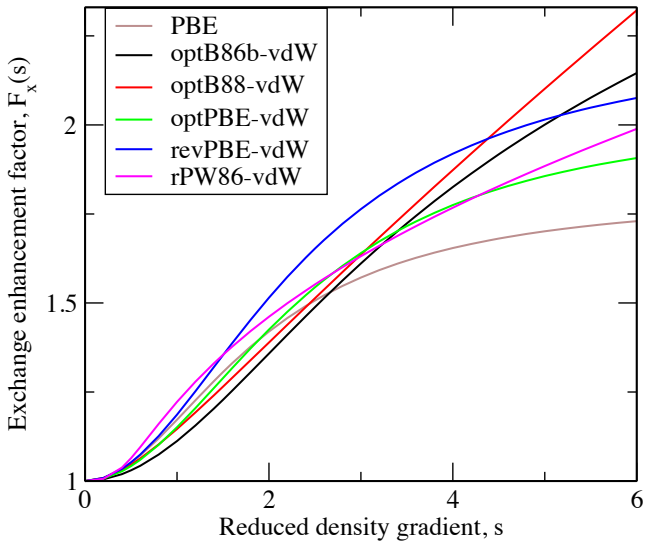

Figure 0.2 Plot of enhancement factors of exchange GGA fuctionals used in vdW-DF, including PBE, as a function of the reduced density gradient (s)

Appendix B. Supporting Information for Metal Substituted M-MOF-74 and M-HKUST-1 for Carbon Capture

Table 0.1 Calculated cell parameters and cell volumes for M-DOBDC and M-HKUST-1

MOF	Metal	a (Å)	c (Å)	V (Å^3)	Experiment		
					a (Å)	c (Å)	V (Å^3)
DOBDC	Be	26.29	6.32	3780.72			
	Mg	26.12	6.93	4097.08	26.02[60]	6.72[60]	3940.75[60]
	Ca	26.54	7.69	4690.18			
	Sr	26.13	8.08	4779.14			
	Sc	26.11	7.25	4280.02			
	Ti	26.39	6.99	4212.88			
	V	26.07	6.97	4104.92			
	Cr	26.00	6.94	4064.92			
	Mn	26.35	7.15	4297.38	26.23[67]	7.04[67]	
	Fe	26.36	6.88	4142.66	26.10[66]	6.85[66]	4041.30[66]
	Co	26.16	6.89	3967.10	26.11[148]	6.72[148]	
	Ni	25.89	6.79	3898.34	25.79[147]	6.77[147]	3898.34[147]
	Cu	25.60	6.70	3806.73			
	Zn	26.17	6.92	4102.34	25.93[65]	6.83[65]	
	Mo	26.22	7.00	4168.57			
	Sn	26.62	7.19	4411.11			
	W	26.98	6.29	3964.40			
	Pb	26.65	8.05	4948.50			
HKUST-1	Be	25.42		16428.72			
	Mg	26.62		18853.14			
	Ca	27.36		20480.62			
	Sr	27.72		21309.72			
	Sc	26.62		18867.43			
	Ti	26.68		18992.96			
	V	26.73		19091.71			
	Cr	26.70		19028.93	26.67[112]		18959.88[112]
	Mn	26.38		18352.21			
	Fe	26.35		18303.91			
	Co	26.21		18025.33			
	Ni	26.31		18219.00	26.59[71]		18808.57[71]
	Cu	26.48		18572.70	26.34[69]		18280.00[69]
	Zn	26.82		19286.58	26.52[72]		18651.79[72]
	Mo	27.30		20337.12	27.13[74]		19966.47[74]
	Sn	27.03		19741.74			
	W	27.19		20096.96			
	Pb	27.64		21106.10			

Table 0.2 Average calculated metal-oxygen bond lengths (in Å) within M-DOBDC. In all cases the metal ion adopts either a tetragonal or square pyramidal coordination to oxygen; a missing value for d(M-05) indicates that the structure adopts a tetrahedral geometry.

MOFs	Metal	d(M-O1)	d(M-O2)	d(M-O3)	d(M-O4)	d(M-O5)
DOBDC	Be	1.54	1.622	1.681	1.756	
	Mg	2.032	2.032	2.045	2.048	2.087
	Ca	2.284	2.304	2.326	2.352	2.375
	Sr	2.436	2.468	2.535	2.536	2.549
	Sc	2.105	2.221	2.03	2.109	2.205
	Ti	2.059	2.061	2.013	2.081	1.963
	V	2.033	2.059	2.102	2.025	2.07
	Cr	2.002	2.033	2.038	2.079	
	Mn	2.088	2.103	2.107	2.145	2.264
	Fe	2.045	2.072	2.074	2.128	2.156
	Co	2.003	2.026	2.065	2.074	2.123
	Ni	1.986	2.023	2.023	2.102	2.108
	Cu	1.974	1.988	1.999	2.056	
	Zn	2.033	2.045	2.052	2.101	2.195
	Mo	2.073	2.106	2.169	2.179	2.187
	W	2.047	2.05	2.175	2.216	2.217
	Sn	2.291	2.313	2.328	2.34	
	Pb	2.328	2.388	2.554	2.611	2.696

Table 0.3 Average calculated metal-oxygen and metal-metal bond lengths (in Å) for M-HKUST-1. The SBUs in M-HKUST-1s exhibit paddle wheel geometry, with 4 metal-oxygen bonds and one metal-metal bond.

MOFs	Metal	d(M-O1)	d(M-O2)	d(M-O3)	d(M-O4)	d(M-M)
HKUST-1	Be	1.738	1.738	1.73	1.73	2.469
	Mg	2.008	2.008	2.008	2.008	2.937
	Ca	2.254	2.254	2.254	2.254	3.61
	Sr	2.41	2.41	2.41	2.41	3.895
	Sc	2.079	2.079	2.079	2.079	3.151
	Ti	1.973	1.973	1.973	1.973	2.872
	V	2.037	2.037	2.037	2.037	1.97
	Cr	1.99	1.99	1.99	1.99	2.086
	Mn	1.936	1.936	1.936	1.936	2.578
	Fe	1.925	1.925	1.925	1.925	2.201
	Co	1.908	1.908	1.908	1.908	2.235
	Ni	1.938	1.938	1.938	1.938	2.351
	Cu	1.975	1.975	1.975	1.975	2.521
	Zn	2.032	2.032	2.032	2.032	2.644
	Mo	2.1	2.1	2.101	2.101	2.136
	W	2.077	2.077	2.077	2.077	2.214
	Sn	2.265	2.265	2.293	2.293	4.199
	Pb	2.38	2.38	2.379	2.379	4.212

Table 0.4 Tabulated ionic radii of +2 metal ions[210] and electronegativity of the metal atoms[211]. Low spin configurations refer to metals in M-DOBDC; high spin cases refer to M-HKUST-1.

	Radii (Å)		Electro-
Metal	Low spin	High spin	negativity
Be	0.45		1.57
Mg	0.72		1.31
Ca	1.00		1
Sr	1.18		0.95
Sc			1.36
Ti	0.86		1.54
V	0.79		1.63
Cr	0.73	0.80	1.66
Mn	0.67	0.83	1.55
Fe	0.61	0.78	1.83
Co	0.65	0.745	1.88
Ni	0.69		1.91
Cu	0.73		1.9
Zn	0.74		1.65
Mo			2.16
W			2.36
Sn	0.93[212]		1.96
Pb	1.19		2.33

Table 0.5 Calculated bond lengths (Å) and bond angles (°) involving the MOF metal site (M) and adsorbed CO_2. d(M-O) refers to the distance between the metal and the nearest oxygen in CO_2; d(MO-CO) is the length of the O-C bond (within CO_2) closest to the metal; d(C-O) is the length of the O-C bond (within CO_2) farthest from the metal;<M-O-C is the angle formed by the metal and the nearest O and C in CO_2; <O-C-O is bending angle within the CO_2 molecule.

MOF	Metal	d(M-O)	d(MO-CO)	d(C-O)	<M-O-C	<O-C-O
M/DOBDC	Be	3.858	1.181	1.179	84.261	180.000
	Mg	2.392	1.184	1.174	130.950	178.350
	Ca	2.623	1.182	1.174	148.845	178.599
	Sr	2.842	1.181	1.176	160.263	178.472
	Sc	2.445	1.187	1.172	135.160	176.462
	Ti	2.444	1.186	1.173	131.538	177.235
	V	2.340	1.185	1.173	133.553	177.738
	Cr	3.286	1.182	1.179	110.796	180.000
	Mn	2.695	1.183	1.176	125.079	180.000
	Fe	2.717	1.183	1.177	119.707	179.141
	Co	2.812	1.183	1.177	115.950	179.053
	Ni	2.617	1.183	1.176	120.292	179.016
	Cu	3.228	1.181	1.179	109.914	180.000
	Zn	2.867	1.183	1.177	115.937	178.883
	Mo	2.528	1.185	1.174	128.753	178.437
	W	2.450	1.187	1.173	132.420	178.262
	Sn	4.007	1.180	1.180	84.521	180.000
	Pb	3.402	1.182	1.178	131.434	180.000
M/HKUST-1	Be	1.945	1.190	1.169	118.703	177.382
	Mg	2.221	1.191	1.168	117.588	177.245
	Ca	2.624	1.188	1.170	111.801	177.425
	Sr	2.861	1.187	1.172	108.801	177.576
	Sc	2.096	1.290	1.204	88.769	140.807
	Ti	2.686	1.189	1.172	111.964	180.000
	V	2.772	1.186	1.174	110.961	180.000
	Cr	3.149	1.182	1.177	101.390	180.000
	Mn	3.106	1.182	1.177	100.034	180.000
	Fe	3.282	1.180	1.179	96.000	180.000
	Co	2.584	1.185	1.175	112.243	180.000
	Ni	2.731	1.184	1.176	107.581	180.000
	Cu	2.769	1.184	1.176	106.633	180.000
	Zn	2.384	1.188	1.171	116.371	178.106
	Mo	3.340	1.182	1.178	100.457	180.000
	W	3.127	1.184	1.176	105.326	180.000
	Sn	3.811	1.177	1.181	79.773	180.000
	Pb	3.840	1.182	1.178	73.975	180.000

Table B.6 Calculated binding energies (ΔE) at 0K, zero point energies (ZPE), thermal energy contributions (TE) at 300K, and adsorption enthalpies (ΔH) at 300K for M-DOBDC and M-HKUST-1 within the LDA, PBE-GGA, DFT-D2 and revPBE-vdW methods. All energies are given in kJ/mol CO_2. rPBE-vdW is shorthand for revPBE-vdW

		ΔE (kJ/mol)				ZPE (kJ/mol)		TE (kJ/mol)		ΔH (kJ/mol)		Exp
		LDA	PBE	DFT-D2	rPBE-vdW	DFT-D2	rPBE-vdW	DFT-D2	rPBE-vdW	DFT-D2	rPBE-vdW	
M-DOBDC	Be	-20.62	-9.71	-19.49	-34.01	2.88	1.38	1.04	0.82	-15.57	-31.81	
	Mg	-52.30	-27.06	-42.31	-50.89	2.36	2.15	1.40	1.53	-38.55	-47.20	-44.2±4.6
	Ca	-48.28	-28.67	-39.87	-50.21	2.30	2.03	1.44	1.93	-36.13	-46.26	
	Sr	-41.67	-25.50	-34.36	-46.88	2.64	1.35	1.35	0.91	-30.37	-44.63	
	Sc		-21.03	-43.85	-53.92	0.24	0.84	1.82	1.53	-41.79	-51.54	
	Ti	-69.16	-26.02	-51.23	-56.15	2.40	2.25	0.98	1.22	-47.85	-52.69	
	V	-52.61	-29.63	-54.13	-57.49	2.88	2.92	-0.94	1.11	-52.18	-53.46	
	Cr	-36.41	-10.94	-19.14	-36.68	1.73	1.53	-0.02	2.30	-17.43	-32.85	
	Mn	-37.06	-16.55	-28.56	-39.12	0.56	1.27	-0.91	0.59	-28.91	-37.25	
	Fe	-35.23	-9.54	-25.19	-33.67	2.55	1.27	-0.94	-0.01	-23.58	-32.40	
	Co	-39.38	-14.68	-29.88	-39.32	1.67	1.56	-0.73	0.52	-28.95	-37.24	-35.7±1.9
	Ni		-17.05	-33.62	-41.22	3.81	1.68	0.47	1.82	-29.35	-37.72	-39.6±1.5
	Cu	-30.70	-9.10	-19.14	-27.17	3.37	2.07	0.12	-0.04	-15.65	-25.14	
	Zn	-40.87	-16.51	-30.53	-40.99	1.16	1.52	-0.10	2.89	-29.47	-36.59	30.5+0.5
	Mo	-72.22	-29.32	-48.78	-50.05	1.27	3.05	0.24	1.08	-47.27	-45.93	
	W	-72.37	-31.11	-44.68	-48.92	1.71	2.95	1.40	0.85	-41.58	-45.12	
	Sn	-26.23	-7.52	-17.56	-26.95	3.82	1.43	-0.44	0.46	-14.18	-25.06	
	Pb	-26.09	-7.33	-13.14	-28.17	2.44	1.77	1.31	0.78	-9.39	-25.62	
M-HKUST-1	Be	-61.63	-29.04	-43.68	-48.09	2.34	3.12	0.04	-2.54	-41.30	-47.51	
	Mg	-59.50	-35.37	-52.27	-57.12	3.84	2.29	1.46	-1.32	-46.96	-56.14	
	Ca	-48.79	-25.15	-50.58	-51.41	2.71	1.80	-2.18	-1.69	-50.06	-51.30	
	Sr	-45.26	-20.85	-52.65	-51.78	2.88	7.70	3.92	-0.98	-45.85	-45.06	
	Sc	-57.40	-31.91	-42.91	-47.81	1.31	0.85	-2.02	2.16	-43.62	-44.80	
	Ti	-42.32	-13.59	-27.87	-29.90	0.33	1.61	-3.36	-2.33	-30.90	-30.62	
	V	-29.98	-2.81	-17.83	-18.72	0.08	1.22	-5.67	-0.40	-23.42	-17.89	
	Cr	-27.13	-7.59	-21.32	-24.85	2.39	2.01	-1.52	0.76	-20.44	-22.08	-26.7
	Mn	-26.10	-5.80	-21.14	-25.68	4.49	1.21	-4.22	-1.93	-20.87	-26.40	
	Fe	-30.47	-4.93	-19.95	-25.76	6.51	0.68	1.47	-1.44	-11.97	-26.52	
	Co	-43.66	-11.92	-26.37	-30.36	1.73	2.17	2.46	-0.72	-22.19	-28.91	
	Ni	-20.46	-9.59	-23.50	-28.45	0.90	1.09	-1.05	-4.95	-23.65	-32.31	-36.8
	Cu	-31.49	-8.93	-22.56	-27.32	4.81	0.94	-0.08	-4.09	-17.83	-30.47	-23.7±8.2
	Zn	-55.56	-25.37	-38.67	-41.08	2.64	3.58	1.65	0.94	-34.38	-36.56	
	Mo	-25.96	-6.40	-22.03	-25.55	1.88	1.35	2.65	-2.21	-17.50	-26.41	-25.6
	W	-26.32	-5.94	-21.48	-22.40	9.45	0.85	-3.90	2.16	-15.93	-19.39	
	Sn	-20.94	1.69	-9.04	-21.01	-2.33	1.61	-2.69	-2.33	-14.06	-21.74	
	Pb	-3.72	4.44	-7.31	-10.15	4.09	1.22	-1.86	-0.40	-5.07	-9.33	

Table B.7 Change in the metal atom's (Δq_M) and CO_2 molecule's partial charge (Δq_{CO2}) upon CO_2 adsorption. $\Delta q < 0$ indicates a reduction in positive charge.

Metal	DOBDC		HKUST-1	
	Δq_M	Δq_{CO2}	Δq_M	Δq_{CO2}
Sc	0.160	0.007	0.221	-0.314
Ti	-0.398	0.039	0.141	-0.002
V	-0.204	0.031	0.422	0.002
Cr	0.057	-0.037	0.055	0.001
Mn	0.171	-0.015	0.095	-0.001
Fe	-0.042	-0.019	0.062	0.000
Co	0.042	-0.021	-0.035	0.010
Ni	-0.035	-0.003	0.021	0.006
Cu	0.044	-0.016	0.117	0.006
Zn	0.072	-0.024	-0.140	0.051
Mo	-0.264	0.044	0.059	-0.006
W	-0.075	0.056	0.083	-0.003

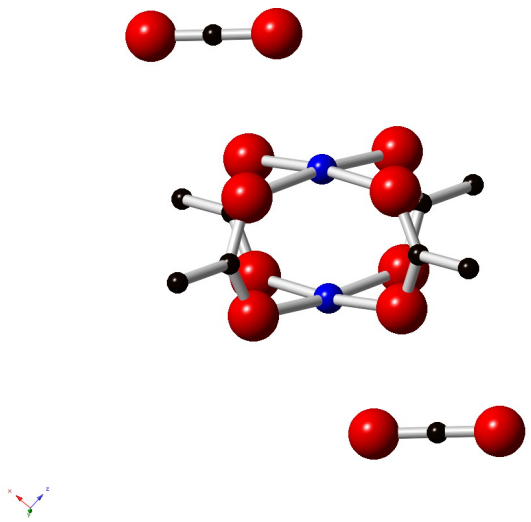

Figure B.1 *tran*-configuration of CO_2 molecules in Cu-HKUST-1. (red = Oxygen, black = Carbon, blue = copper)

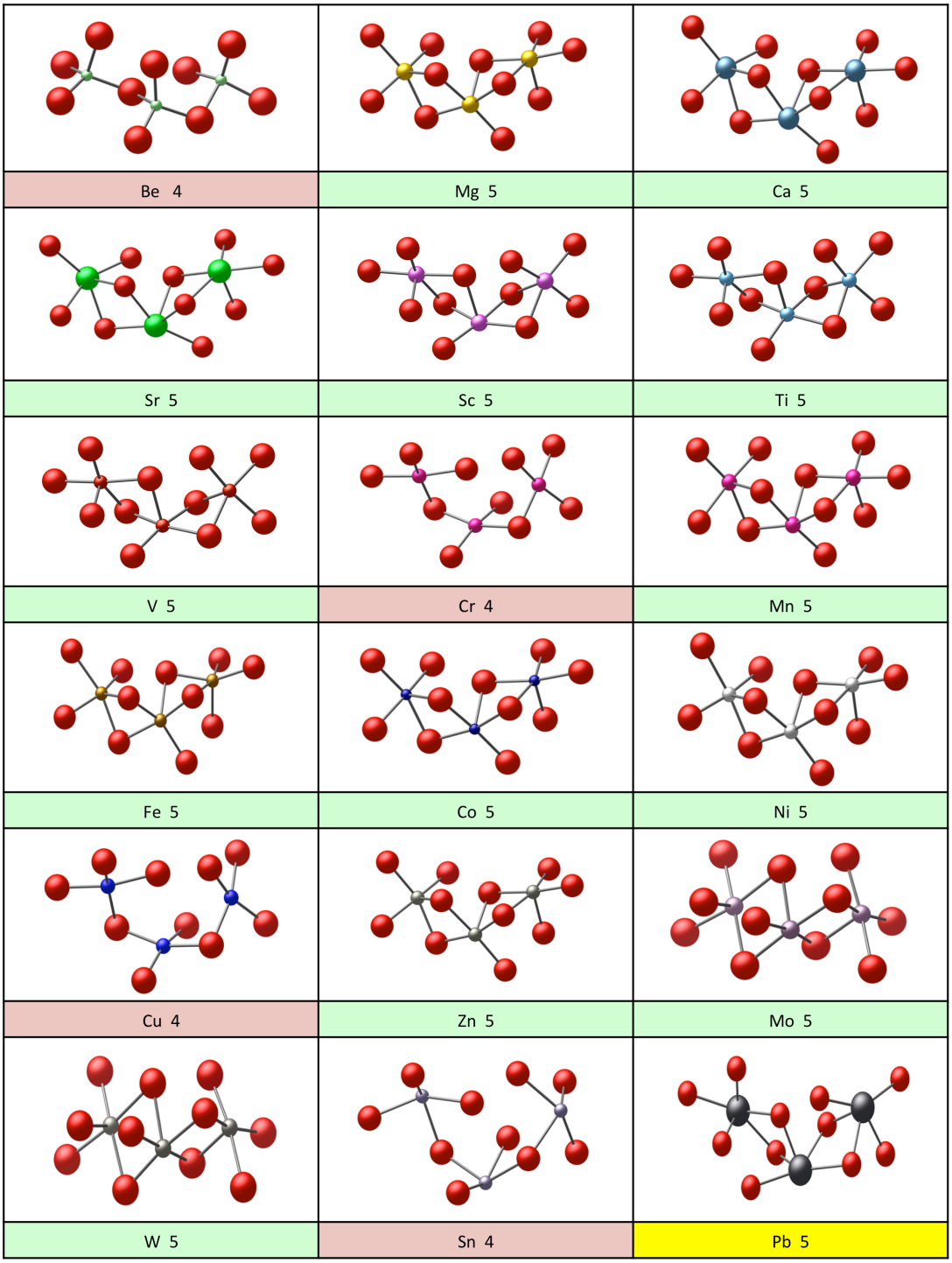

Figure B.2 Calculated local geometries for the M-DOBDC SBU; for clarity, only a portion of the infinite SBU chain is included. Oxygen atoms are red, other colors represent metals. Numbers following the element name indicate the coordination of the metal site. Clusters highlighted in red (Be, Cr, Cu, Sn) exhibit tetrahedral bonding of the metal ions; yellow highlighting (Pb) indicates the presence of other significant structural distortions.

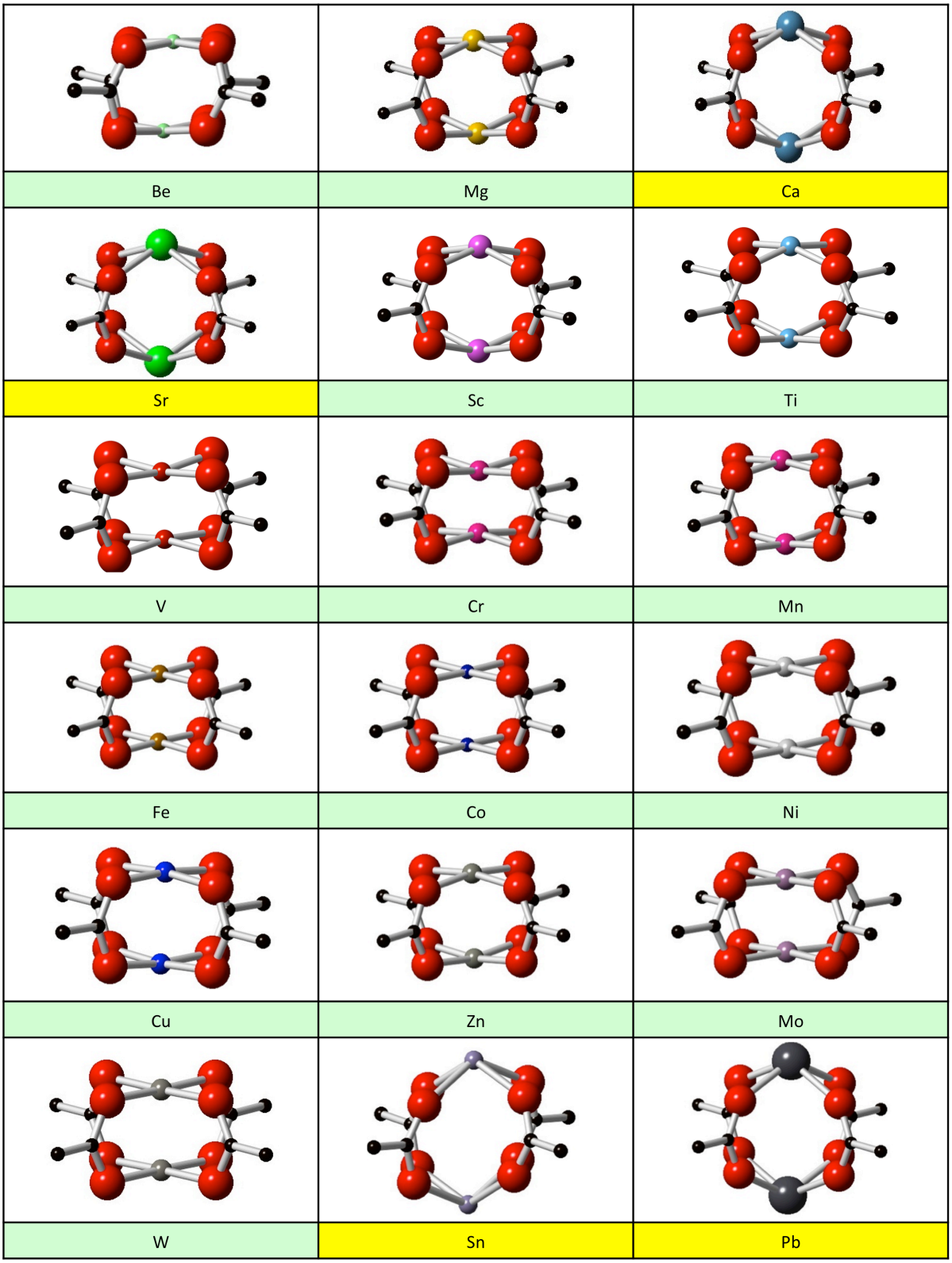

Figure B.3 Calculated local geometries for the M-HKUST-1 SBU. Oxygen atoms are red, carbon is black, and other colors represent metals. Clusters highlighted in yellow (Ca, Sr, Sn, Pb) exhibit large distortions to the paddle-wheel structure.

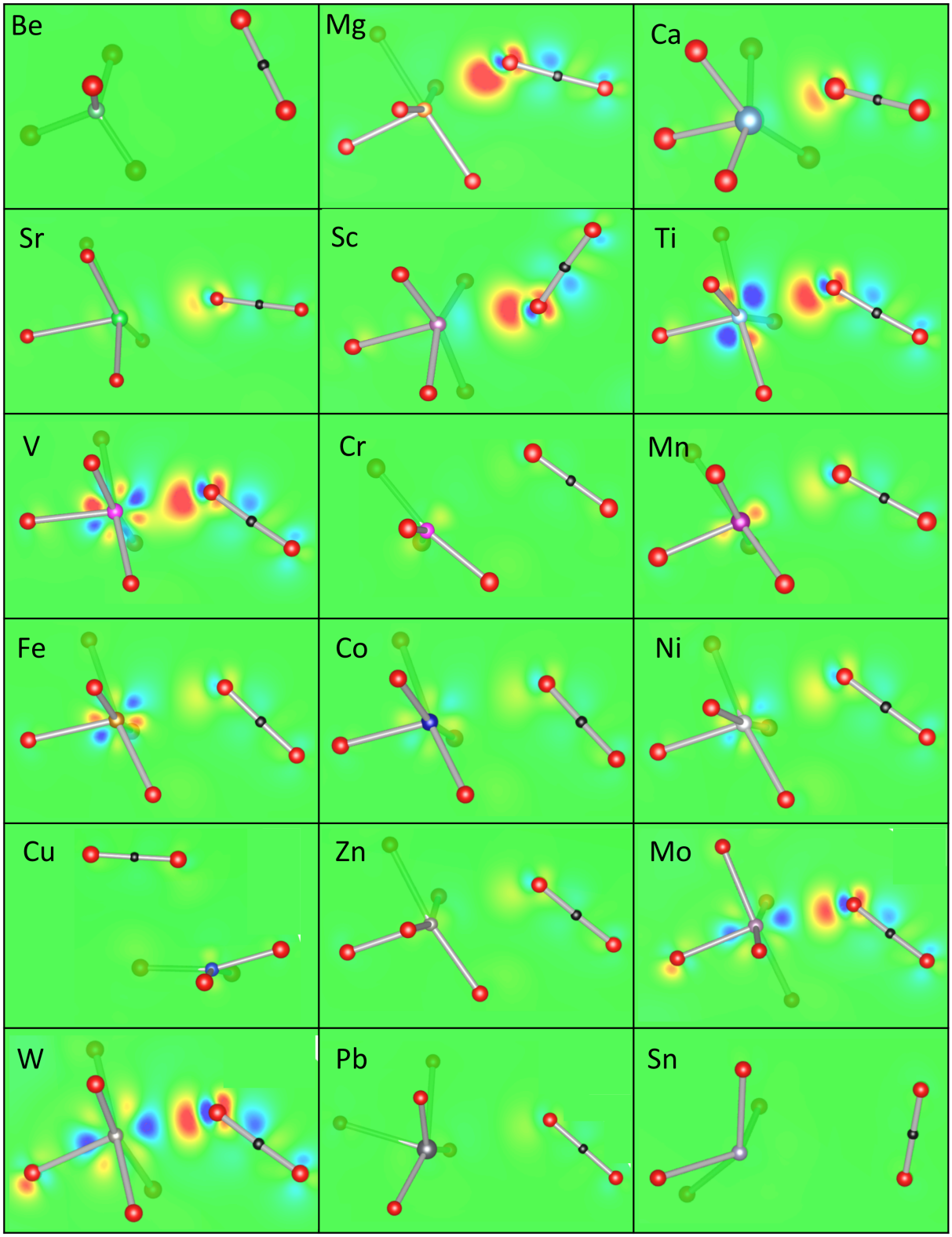

Figure B.4 Charge density difference plots for M-DOBDC. Red and yellow indicate charge accumulation; blue indicates charge depletion. For clarity, only the CO_2 molecule, the metal, and the metal's nearest-neighbor oxygen atoms are illustrated.

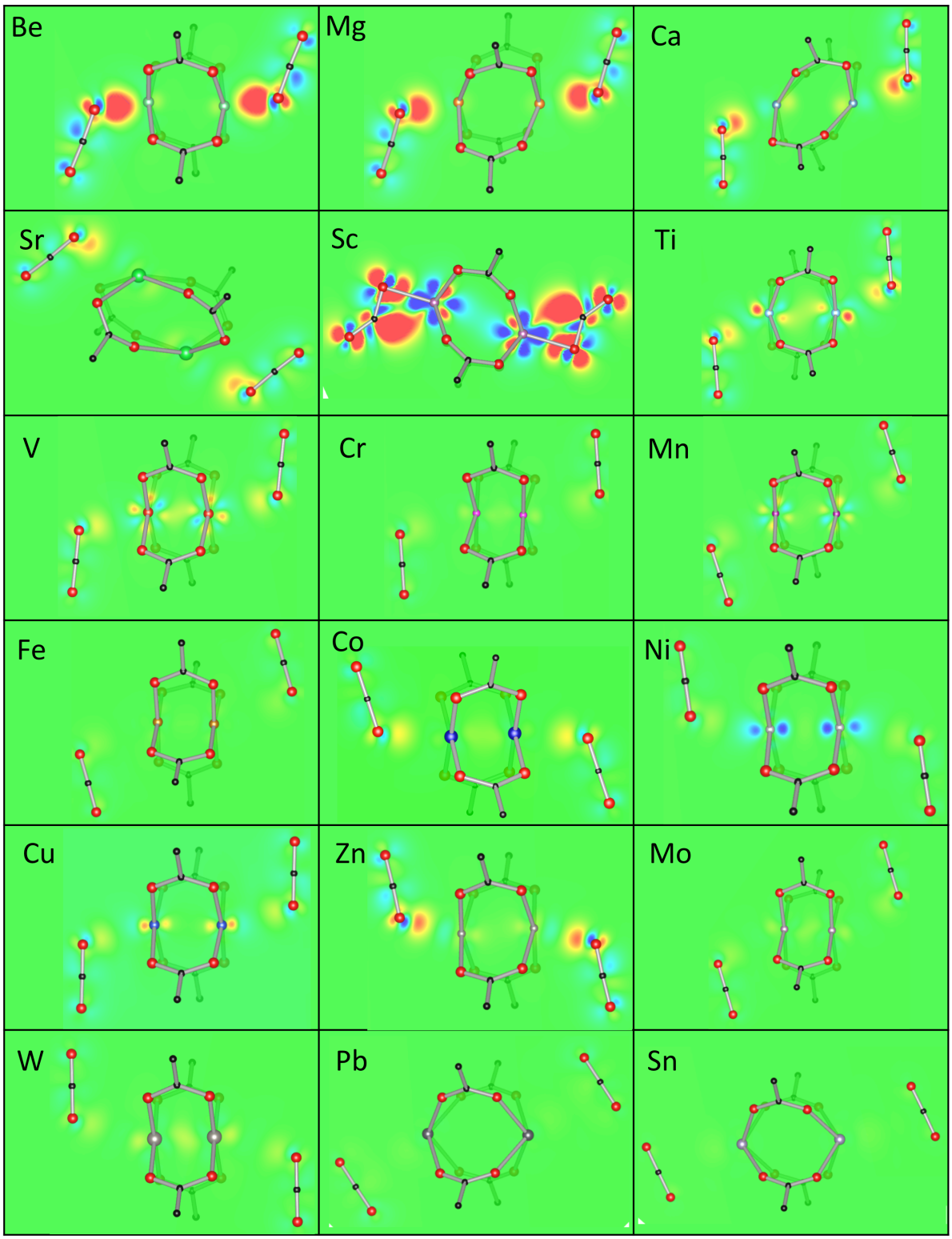

Figure B.5 Charge density difference plots for M-HKUST-1. Red and yellow indicate charge accumulation; blue indicates charge depletion. For clarity, only the CO_2 molecules and atoms from the paddle-wheel SBU are illustrated.

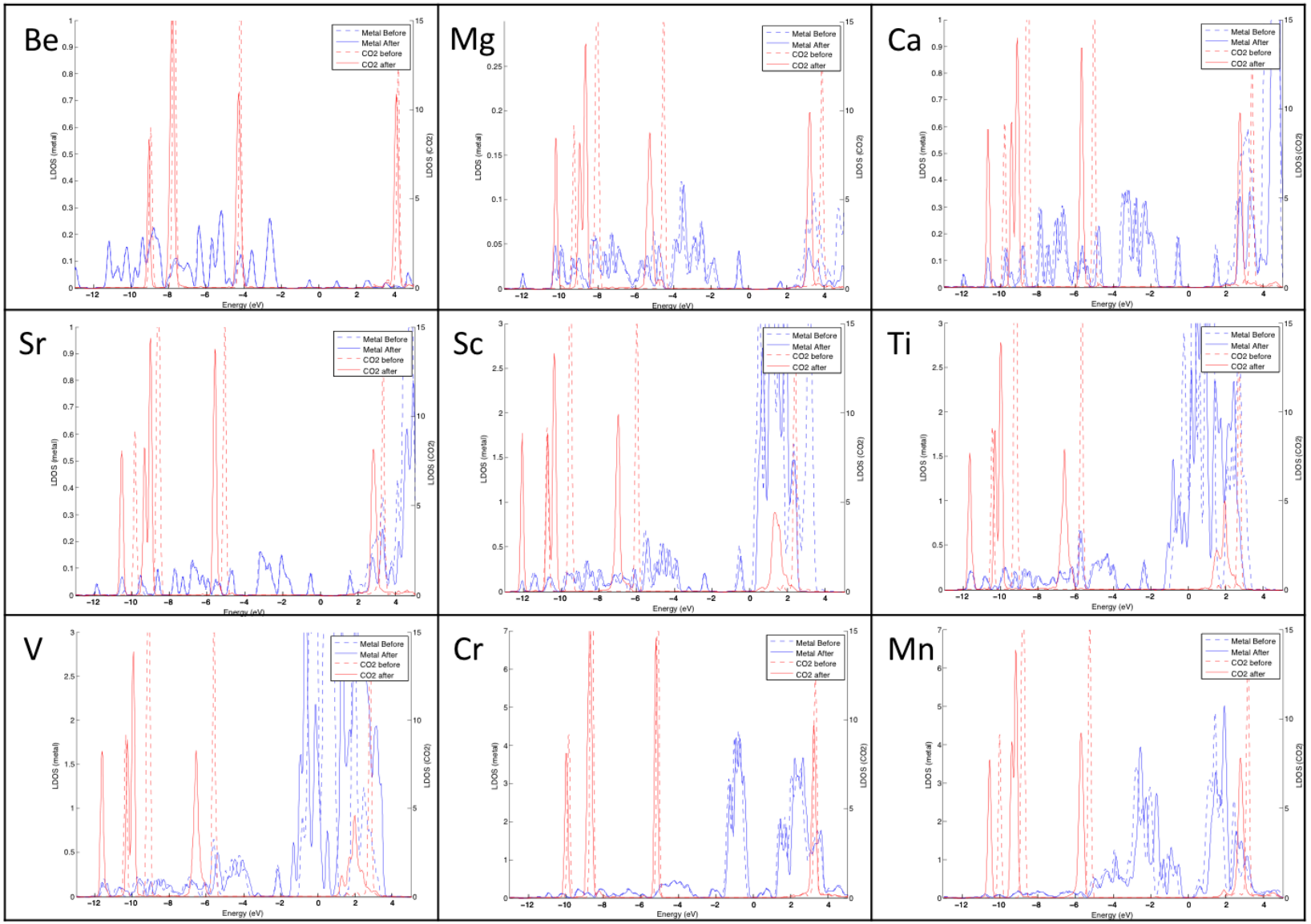

Figure B.6 CO_2 and metal LDOS for M-DOBDC. (Be, Mg, Ca, Sr, Sc, Ti, V, Cr, and Mn)

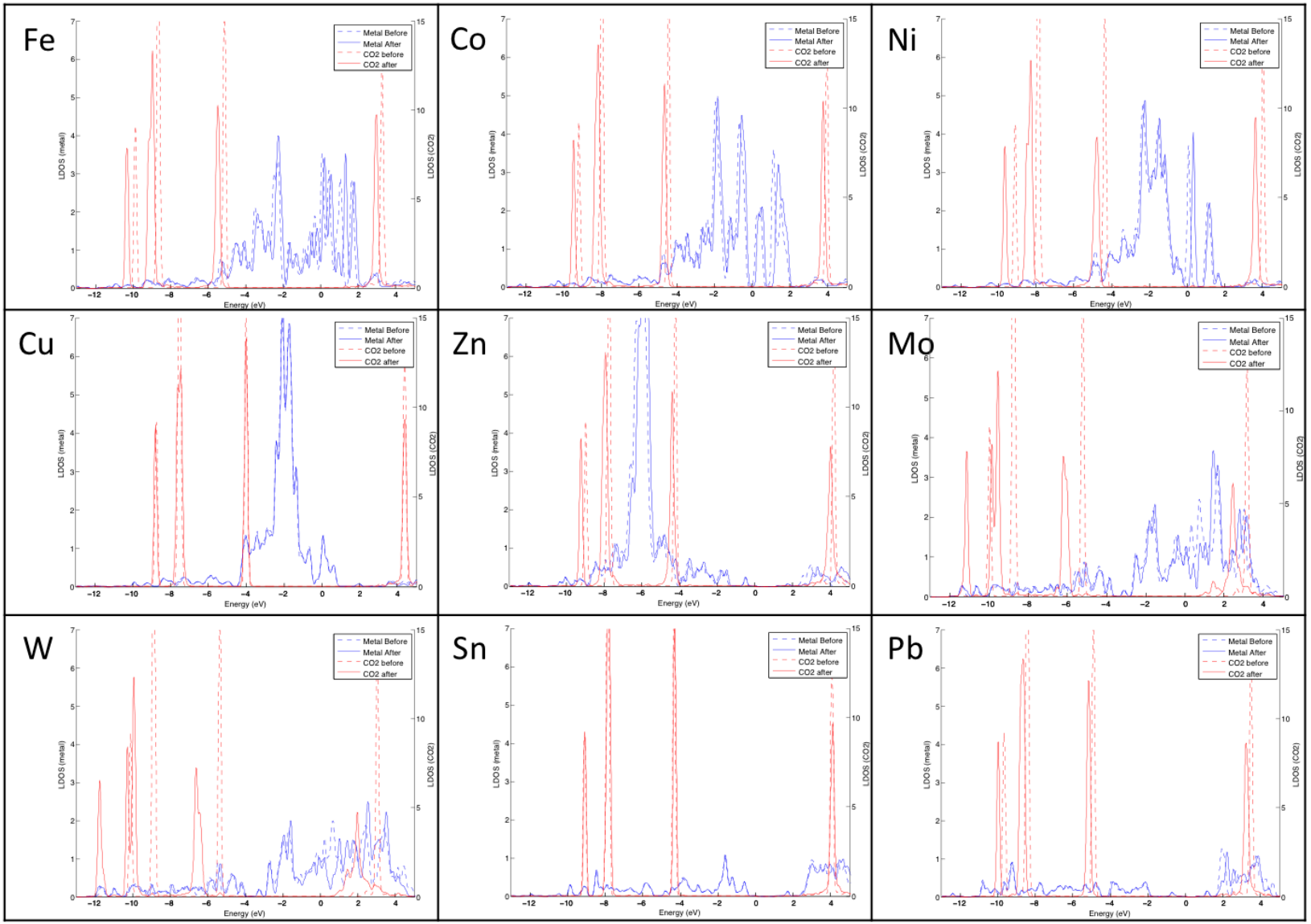

Figure B.7 CO_2 and metal LDOS for M-DOBDC. (Fe, Co, Ni, Cu, Zn, Mo, W, Sn, and Pb)

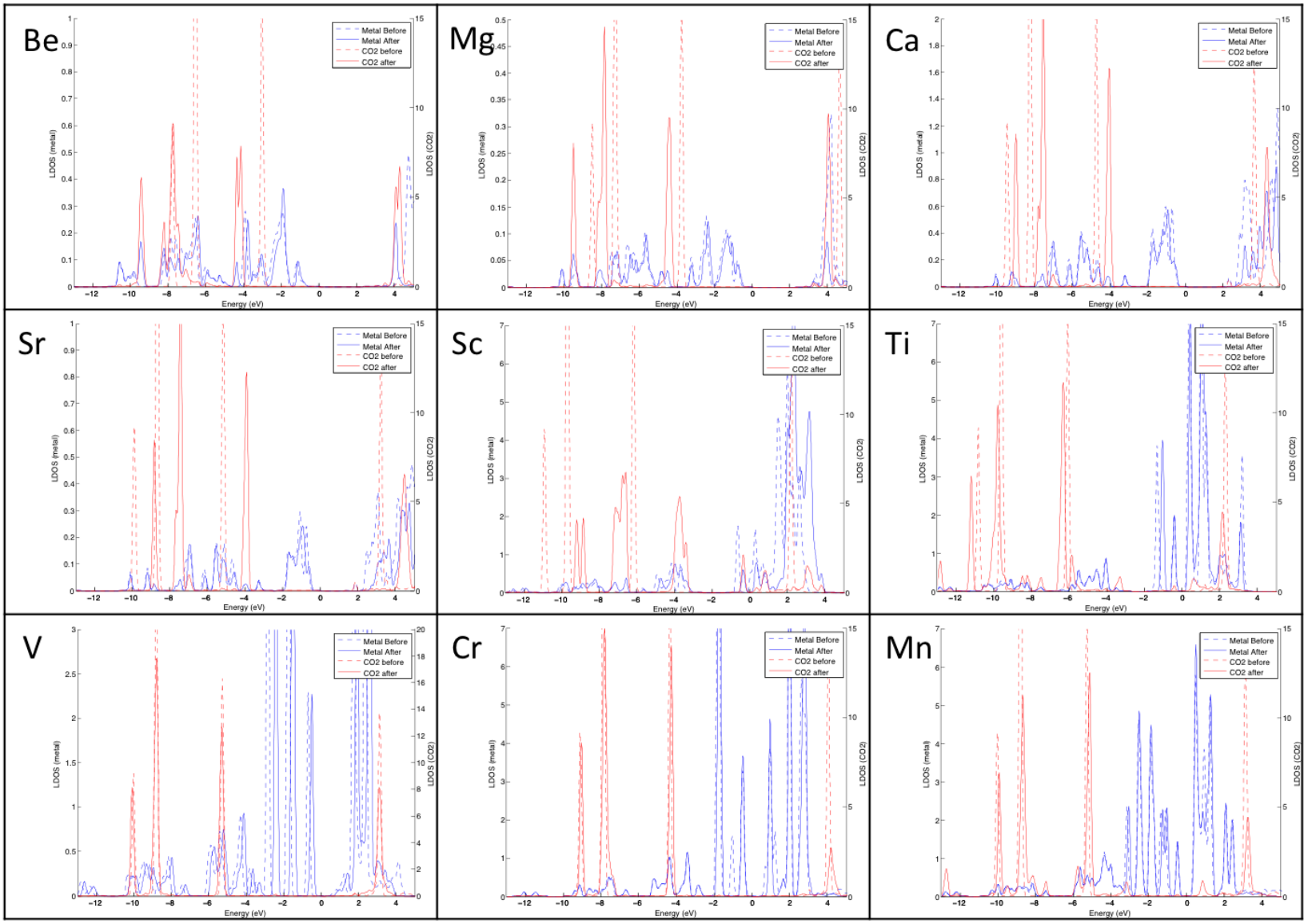

Figure B.8 CO_2 and metal LDOS for M-HKSUT-1. (Be, Mg, Ca, Sr, Sc, Ti, V, Cr, and Mn)

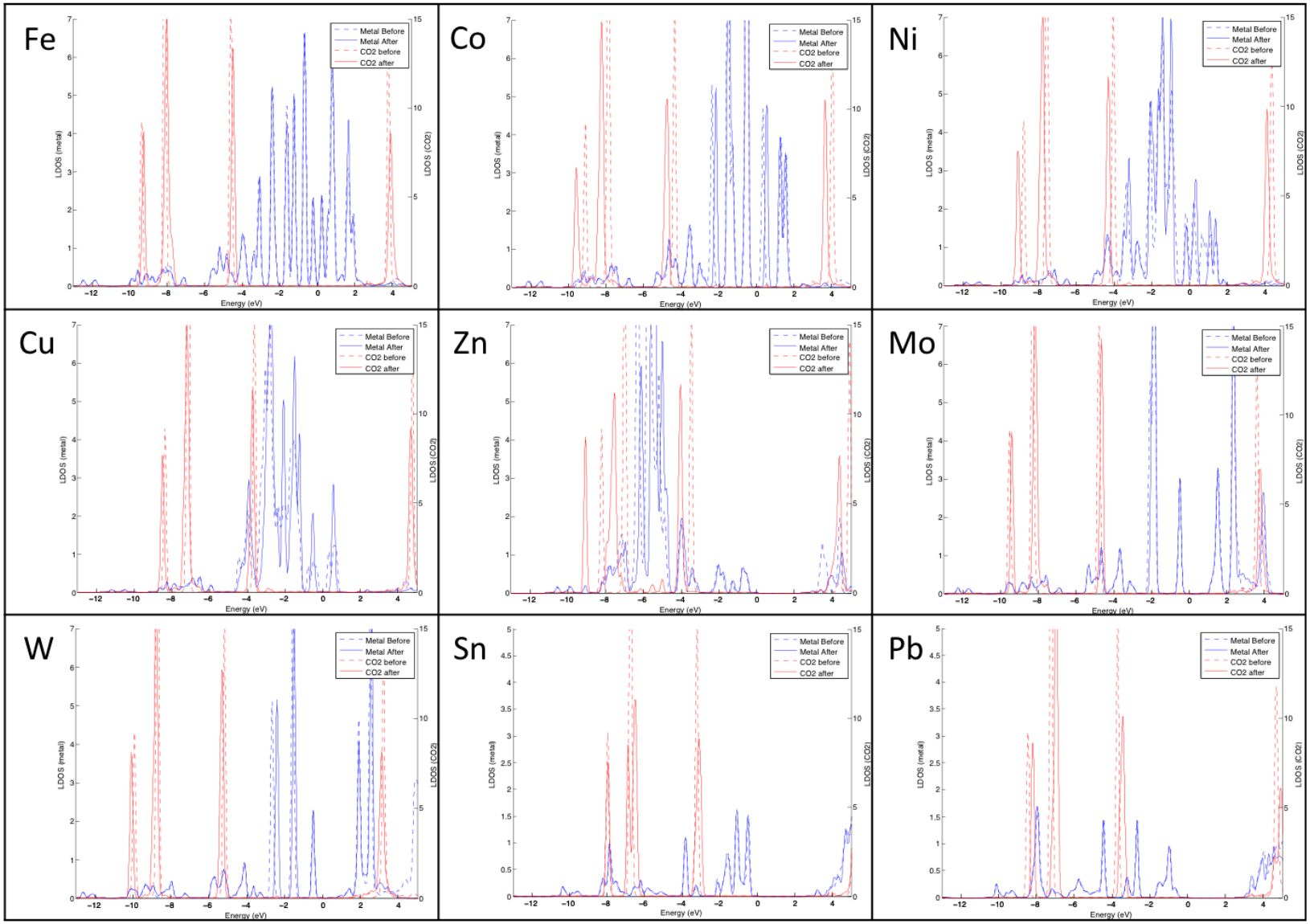

Figure B.9 CO_2 and metal LDOS for M-HKSUT-1. (Fe, Co, Ni, Cu, Zn, Mo, W, Sn, and Pb)

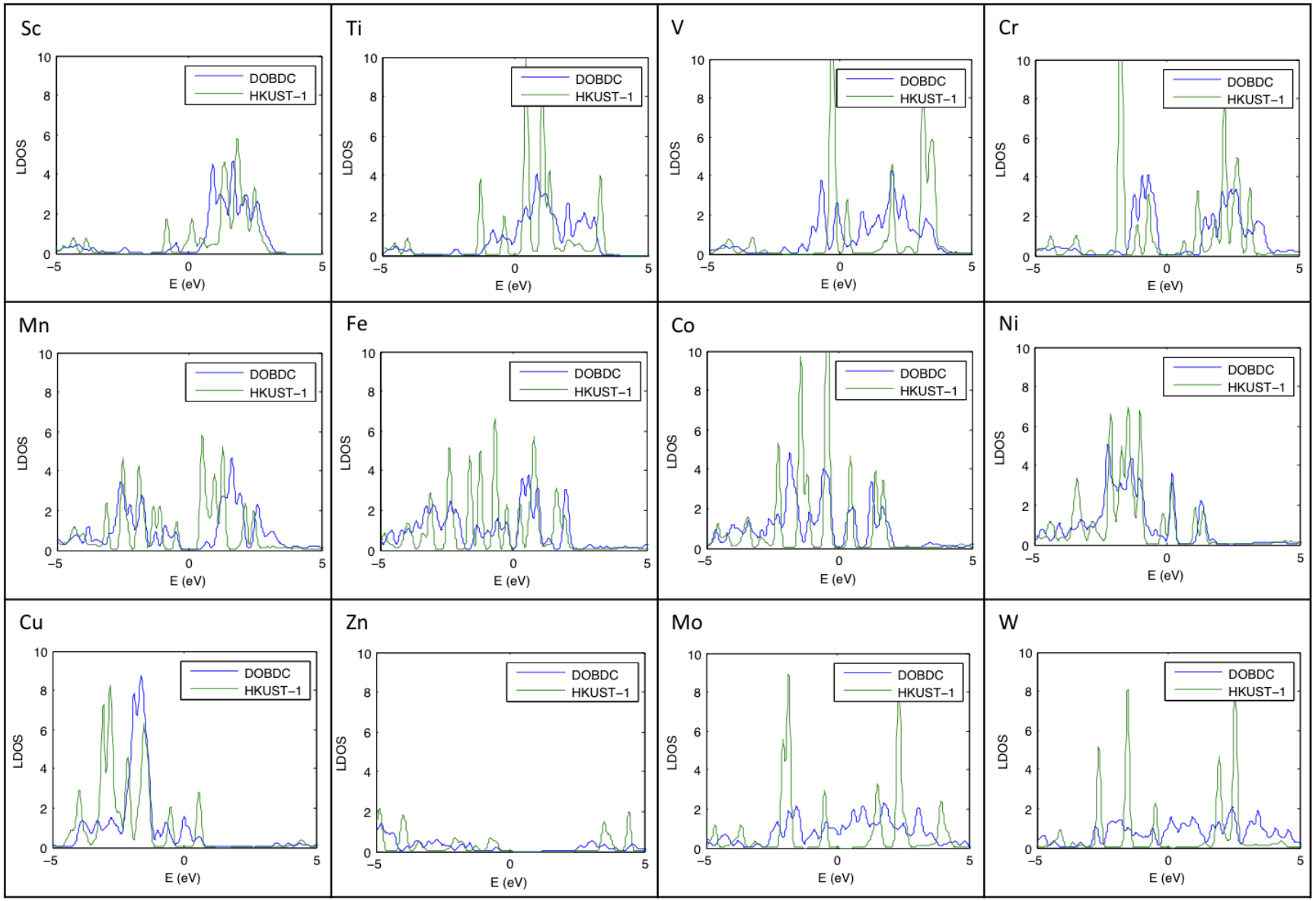

Figure B.10 DOS projected to the metal site for transition metals in M-DOBDC and M-HKUST-1

Comment regarding the geometries and energetics for M = Sn and Pb

Sn protrudes from Sn-DOBDC and Sn-HKUST-1 in a similar fashion; consequently the binding energies of these MOFs are similar. The smaller protrusion of Sn in Sn-DOBDC allows CO_2 to simultaneously interact with the ligand (carboxyl group) to give stronger binding than Sn-HKUST-1. Moreover, larger protrusion of Sn from the MOF framework results in a slight change to the CO_2 binding mode incorporating multiple-site ligand-CO_2 interactions or CO_2-CO_2 interactions. In Sn-DOBDC, CO_2 is closer to the carboxyl group and is complexed through its O atom to the C (carboxyl), with a C (carboxyl)-O_{CO2} distance of 3.562 Å. This is smaller than the Sn-O_{CO2} distance of 4.007 Å (table S5). In Sn-HKUST-1, the CO_2-CO_2 interaction influences the adsorption process. This is suggested by the shorter C_{CO2}-O_{CO2} distance, 3.177 Å, compared to the metal-CO_2 distances. This results in a change to the CO_2 orientation where C_{CO2} rather than O_{CO2} is closer to the metal. The Sn-C_{CO2} and Sn-O_{CO2} distances are, respectively, 3.783 and 3.811 Å. Thus the four-fold CUS site in Sn-DOBDC and Sn-HKUST-1influences CO_2 adsorption somewhat differently than in other metals. Behavior similar to the Sn-based compounds is found for Pb-DOBDC and Pb-HKUST-1.

Appendix C. Supporting Information for Methane Adsorption in M-DOBDC

Table 0.1 Summary of the various force field parameters used in GCMC simulations of CH_4 uptake in MOFs. D_o (kcal/mol) and R_o (Å) are the energy and distance parameters for the 12-6 LJ pair potential form, $E\,(LJ) = D_o[\left(\frac{R_o}{r}\right)^{12} - 2\left(\frac{R_o}{r}\right)^{6}]$.

Molecule	Force field		Ro	Do	Charge	C-H length
	Model	Interaction site				
CH_4	TraPPE[129]	Fictitious	4.19	0.2939		
	Five-site[187]	C	3.82	0.1094	-0.66	1.09
		H	2.97	0.0157	0.165	
	AA (all atom)[188]	C	3.76	0.1017		1.1
		H	3.16	0.0171		
	TraPPE-EH[186]	H (C-H center)	3.72	0.0304		1.09
		C	3.72	0.0000		
MOF	UFF[128]	Metal				
	DREIDING[127]	C, H, O				
	UFF	C, H, O				

Table 0.2 Comparison of calculated CH_4 adsorption energies (in kJ/mol CH_4) in Mg- and Ni-DOBDC using various density functional methods to experimental data from Ref. 68 ΔE is the 0 K static binding energy, while ΔE_{ZPE} and ΔE_{TE} represent, respectively, the zero point energy and thermal energy contributions to the adsorption enthalpy (ΔH) at 300 K.

MOF	Method	ΔE	ΔE_{ZPE}	ΔE_{TE}	ΔH
Mg-DOBDC	Experiment[68]				-21.2
	PBE	-6.3	1.7	-1.4	-6.0
	DFT-D2	-33.1	4.3	1.1	-27.7
	revPBE-vdW	-30.6	1.5	0.5	-28.6
	optB86b-vdW	-35.4	2.5	0.7	-32.2
	optB88-vdW	-34.0	2.7	-0.8	-32.0
	optPBE-vdW	-36.6	2.1	-1.4	-35.9
	rPW86-vdW	-26.6	1.6	-1.3	-26.3
Ni-DOBDC	Experiment[68]				-22.9
	PBE	-3.2	2.1	-0.5	-1.6
	DFT-D2	-46.8	4.2	-0.4	-43.0
	revPBE-vdW	-28.3	1.1	-1.2	-28.4
	optB86b-vdW	-33.7	2.1	-0.3	-31.9
	optB88-vdW	-32.4	2.7	0.4	-29.3
	optPBE-vdW	-34.3	2.2	-1.0	-33.1
	rPW86-vdW	-23.9	1.6	-3.0	-25.3

Table 0.3 Calculated energetics for CH_4 adsorption in M-DOBDC: ΔE at 0 K, zero point energy (ZPE), thermal energy contributions (TE) at 300K, and adsorption enthalpies (ΔH) at 300 K. Energies are calculated using the PBE-GGA, revPBE and rPW86 based vdW-DF methods. All energies are in kJ/mol CH_4.

M-DOBDC	PBE-GGA	revPBE-vdW (vdW-DF1)				rPW86-vdW (vdW-DF2)				Exper-iments[68]
	ΔE	ΔE	ΔE_{ZPE}	ΔE_{TE}	ΔH	ΔE	ΔE_{ZPE}	ΔE_{TE}	ΔH	ΔH
Be	-1.5	-26.7	1.7	2.8	-22.2	-21.3	1.7	1.5	-18.1	
Mg	-6.3	-30.6	1.5	1.7	-27.3	-26.6	1.6	-1.3	-26.3	-21.2
Ca	-9.0	-32.1	2.3	2.4	-27.4	-28.9	2.6	0.5	-25.8	
Sr	-6.7	-30.9	2.4	1.4	-27.0	-27.1	2.2	-1.3	-26.2	
Sc	-1.7	-27.8	0.6	-5.1	-32.3	-27.4	1.1	-0.7	-27.1	
Ti	-7.6	-29.1	1.0	-4.4	-32.5	-27.3	0.6	-6.6	-33.3	
V	-11	-23.3	3.1	-1.2	-21.4	-29.7	2.5	-2.6	-29.7	
Cr	-2.2	-25.3	1.9	2.2	-21.2	-19.4	1.9	1.1	-16.4	
Mn	-2.4	-28.3	1.2	0.9	-26.2	-23.9	1.4	0.0	-22.5	-21.8
Fe	-2.4	-26.6	2.3	2.7	-21.6	-20.9	1.8	-0.8	-19.9	
Co	-3.1	-28.5	1.4	1.9	-25.2	-24.1	0.6	-2.6	-26.0	-22.3
Ni	-3.2	-28.3	1.1	0.1	-27.1	-23.9	1.6	-3.0	-25.3	-22.9
Cu	-1.7	-26.3	1.7	1.2	-23.5	-20.8	1.0	-2.5	-22.3	
Zn	-3.8	-29.9	1.8	3.6	-24.5	-26.0	1.4	-0.7	-25.4	-21.0
Mo	-7.7	-29.3	2.9	1.5	-24.9	-29.6	3.6	-0.5	-26.4	
W	-10.2	-27.9	3.5	-0.3	-24.7	-25.5	3.6	-0.8	-22.8	
Sn	-9.8	-36.1	2.2	0.3	-33.6	-33.0	1.9	-0.9	-32.0	
Pb	-1.5	-28.1	1.9	3.2	-23.0	-24.1	2.2	1.1	-20.9	

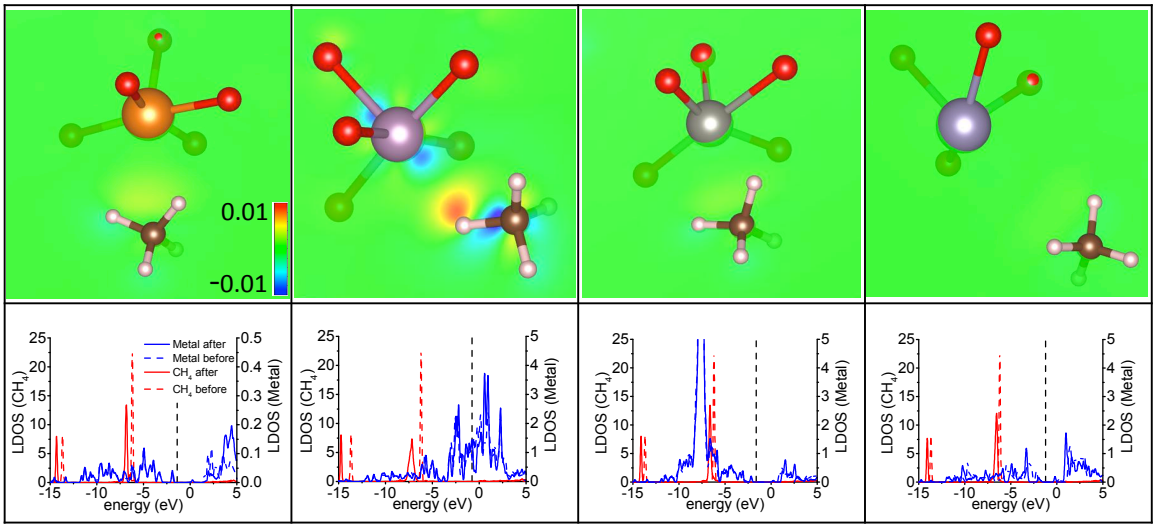

Figure 0.1 Charge density difference (top) and local density of states (LDOS, bottom) for CH_4 adsorption on four representative MOFs: Mg, Mo, Zn, and Sn-DOBDC. For simplicity, in the charge density plots only the CUS metal and its nearest neighbor oxygens are shown. Red represents charge accumulation and blue is charge depletion. The dashed and solid lines in the LDOS refer, respectively, to states before and after CH_4 adsorption. The black dotted line indicates the position of the Fermi level for the MOF+CH_4 (adsorbed) system.

Table 0.4 Non-local dispersion (ΔE_{vdW}) to the static binding energy and adsorption enthalpy from vdW-DF2 calculations. All energies are in kJ/mol CH_4. Tabulated data also include the ionic radius (Å) of the MOF metal ion, partial charge of the metal ion as calculated by the REPEAT method, and the tabulated electronegativity of the metal ion

Metal	ΔE_{vdW}	ΔE	Ionic Radius	Charge	Electro-negativity	ΔH (vdW-DF2)
Be	-28.6	-21.3	0.45	1.278	1.57	-18.1
Mg	-32.1	-26.6	0.72	1.541	1.31	-26.3
Ca	-30.9	-28.9	1	1.480	1	-25.8
Sr	-30.3	-27.1	1.18	1.450	0.95	-26.2
Sc	-31.0	-27.4		1.540	1.36	-27.1
Ti	-35.7	-27.3	0.86	1.682	1.54	-33.3
V	-37.1	-29.7	0.79	1.503	1.63	-29.7
Cr	-24.8	-19.4	0.73	1.066	1.66	-16.4
Mn	-30.9	-23.9	0.67	1.156	1.55	-22.5
Fe	-30.6	-20.9	0.61	1.288	1.83	-19.9
Co	-31.0	-24.1	0.65	1.068	1.88	-26
Ni	-32.3	-23.9	0.69	1.132	1.91	-25.3
Cu	-26.4	-20.8	0.73	0.847	1.9	-22.3
Zn	-31.9	-26	0.74	1.183	1.65	-25.4
Mo	-37.2	-29.6		1.352	2.16	-26.4
W	-37.7	-25.5		1.168	2.36	-22.8
Sn	-22.2	-33	0.93	0.206	1.96	-32
Pb	-31.9	-24.1	1.19	0.774	2.33	-20.9

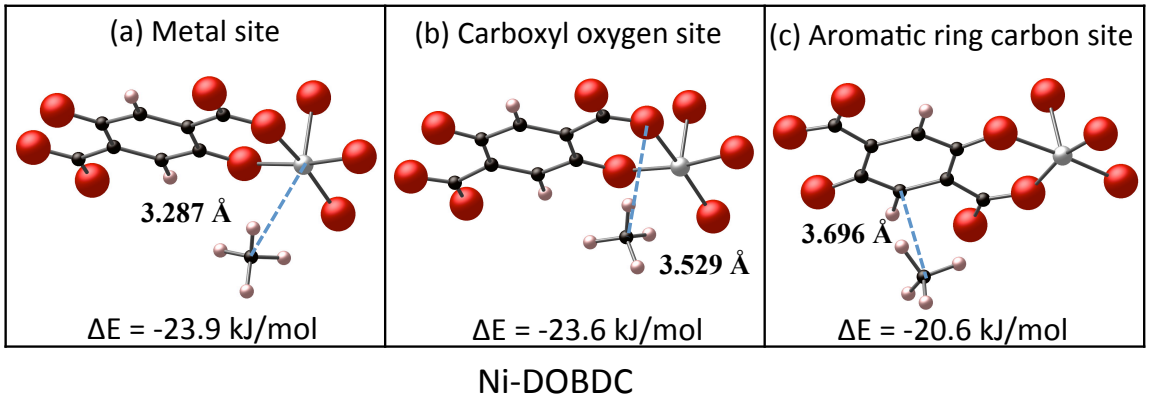

Figure 0.2 Adsorption geometry for CH_4 in Ni-DOBDC at (a) the metal site, (b) the carboxyl oxygen site, and (c) the aromatic ring carbon site

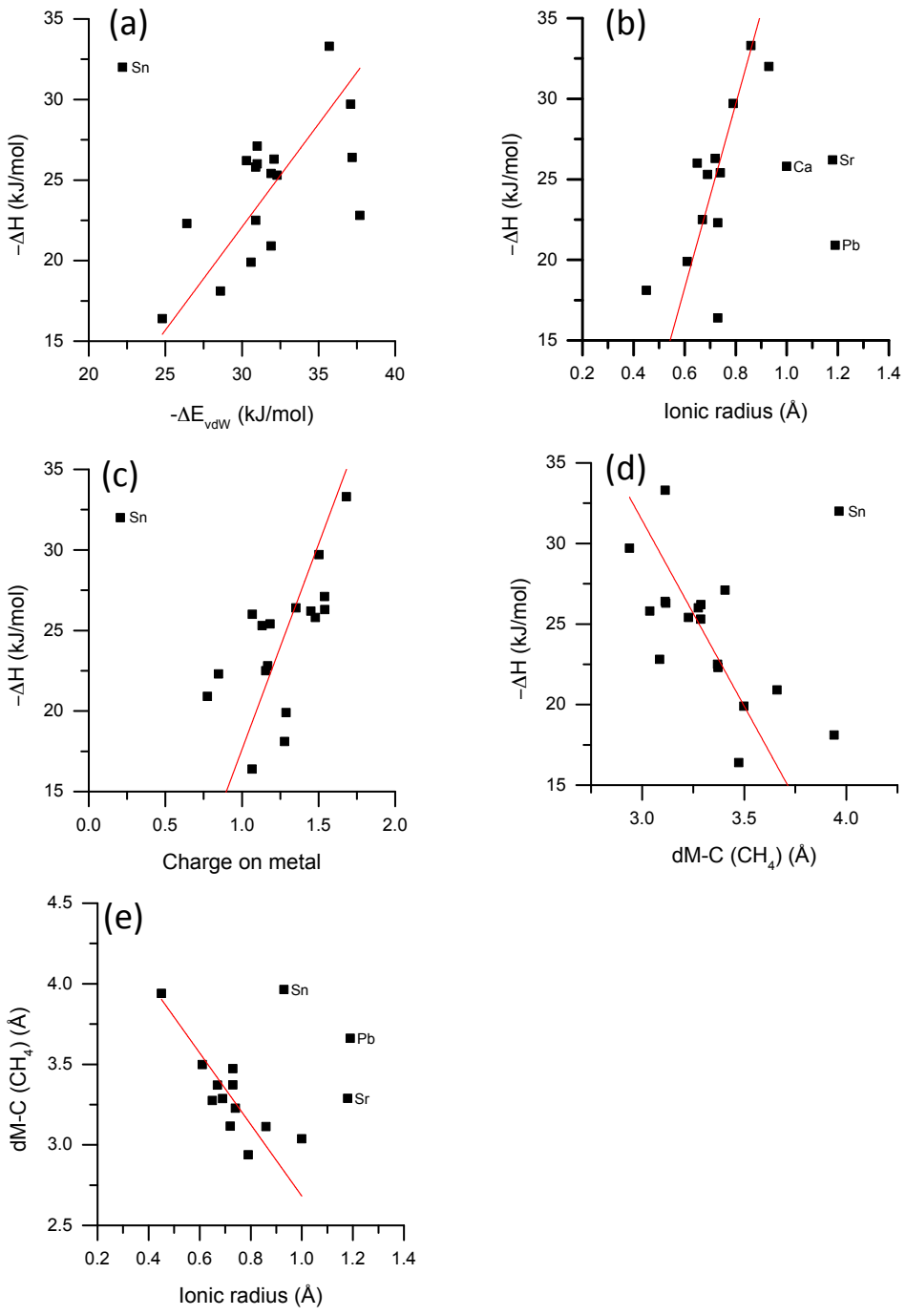

Figure 0.3 Relationships between calculated vdW-DF2 CH_4 adsorption enthalpy in M-DOBDC with: (a) dispersion energy, ΔE_{vdW}, (b) ionic radius of the MOF metal ion, (c) charge on metal, and (d) the distance between metal in MOF and C in CH_4. Panel (e) depicts the correlation between metal ionic radius and the bond distance between the MOF metal and C in CH_4. The red line is a linear regression to the data, which excludes the outlying (named) data points.

Table 0.5 Geometric/structural properties of adsorbed CH_4 in M-DOBDC calculated using vdW-DF2. M-C and O-C refer, respectively, to distances between C in CH_4 from the MOF metal site and the nearest carboxyl MOF O. Distances involving H refer to the H atom in CH_4 closest to the metal, and either: carboxyl MOF O (O-H), carboxyl MOF C (C-H), or MOF metal (M-H). All distances are in Å.

Metal	M-C	M-H	O-C	O-H	C-H	ΔH (kJ/mol)
Be	3.94	3.405	3.718	3.224	3.08	-18.1
Mg	3.116	2.742	3.627	2.722	3.129	-26.3
Ca	3.038	2.85	3.621	2.798	3.092	-25.8
Sr	3.288	3.01	3.605	2.677	3.226	-26.2
Sc	3.406	3.071	3.406	2.876	3.108	-27.1
Ti	3.113	2.676	3.518	2.667	3.107	-33.3
V	2.938	2.47	3.496	2.546	2.965	-29.7
Cr	3.473	3.152	3.797	3.096	3.366	-16.4
Mn	3.37	2.876	3.879	3.182	3.165	-22.5
Fe	3.498	3.066	3.546	2.81	3.219	-19.9
Co	3.275	2.833	3.713	2.779	3.213	-26
Ni	3.287	2.784	3.653	2.783	3.249	-25.3
Cu	3.372	3.072	3.665	2.865	3.405	-22.3
Zn	3.227	2.84	3.74	2.921	3.16	-25.4
Mo	3.113	2.363	3.27	2.768	3.095	-26.4
W	3.086	2.312	3.29	2.88	3.012	-22.8
Sn	3.964	3.414	4.118	3.169	3.01	-32
Pb	3.661	3.411	3.995	3.169	3.12	-20.9

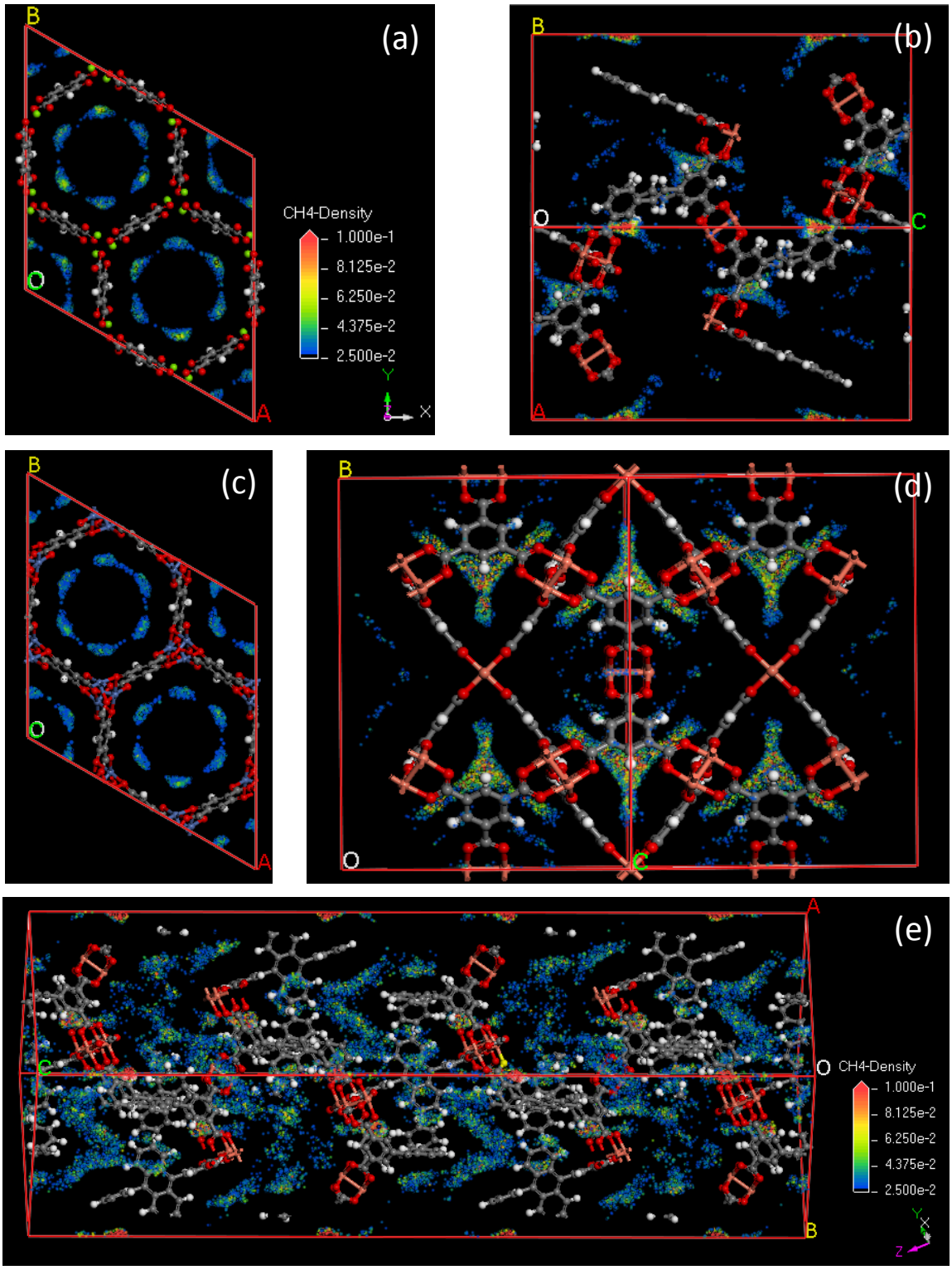

Figure 0.4 Methane density distribution at 5 bar and 298 K for (a) Mg-DOBDC, (b) PCN-11, (c) Ni-DOBDC, (d) HKUST-1, and (e) PCN-14.

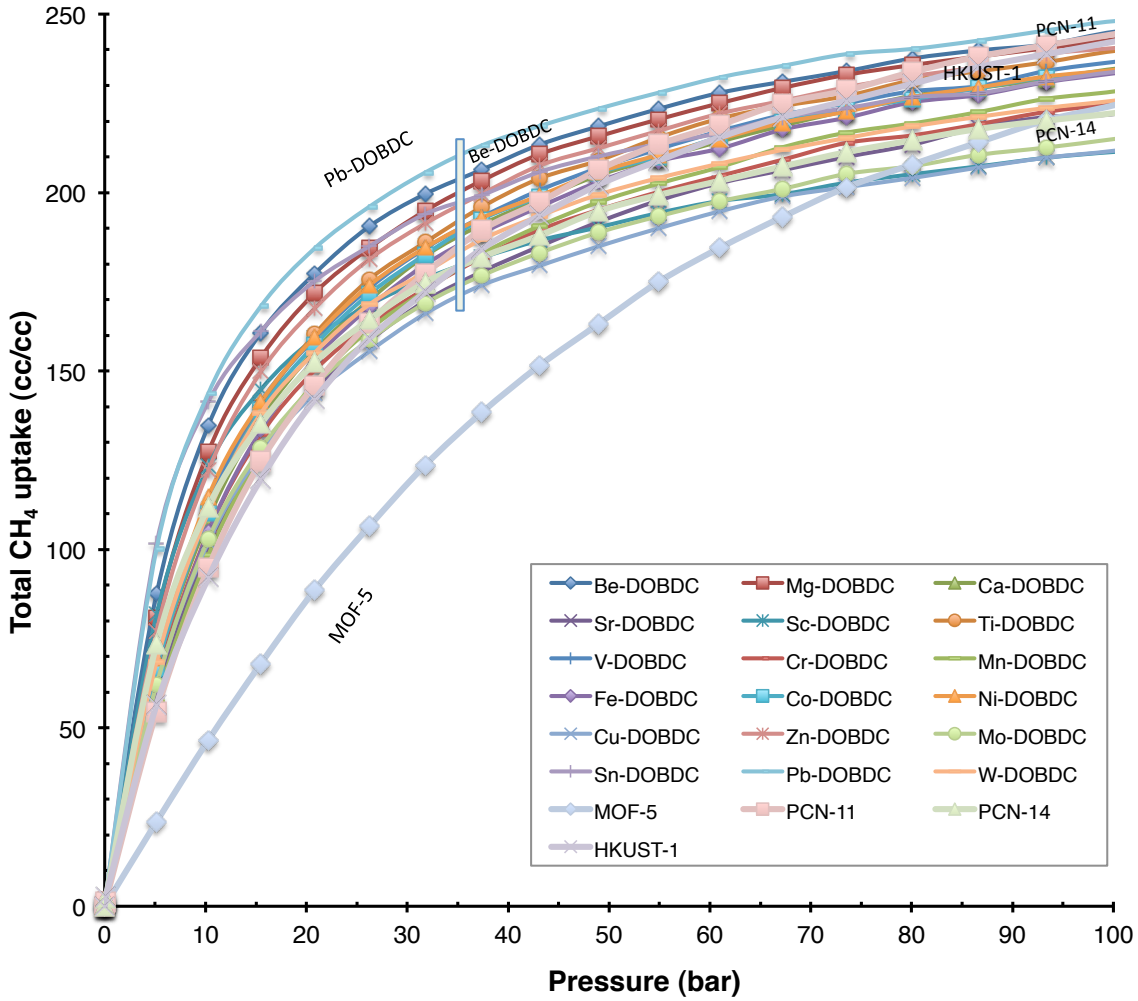

Figure 0.5 Calculated total CH_4 adsorption isotherms (at 298 K) for 18 metal substituted M-DOBDC variants and for MOF-5, PCN-11, PCN-14 and Cu-HKUST-1 using the D-U+TraPPE interatomic potentials. The vertical bar indicates the storage capacities at 35 bar.

Table 0.6 Density of coordinatively unsaturated metal sites in the MOFs examined in this study. * Here MOF-5 is not a CUS MOF

MOF	No. of Metals per Unit Cell	CUS Density (# CUS/nm^3)
Be-DOBDC	18	4.746
Mg-DOBDC	18	4.393
Ca-DOBDC	18	3.838
Sr-DOBDC	18	3.766
Sc-DOBDC	18	4.980
Ti-DOBDC	18	4.272
V-DOBDC	18	4.412
Cr-DOBDC	18	4.527
Mn-DOBDC	18	4.189
Fe-DOBDC	18	4.345
Co-DOBDC	18	4.408
Ni-DOBDC	18	4.564
Cu-DOBDC	18	4.814
Zn-DOBDC	18	4.388
Mo-DOBDC	18	4.688
W-DOBDC	18	4.567
Sn-DOBDC	18	4.190
Pb-DOBDC	18	3.620
MOF-5*	32	1.800
PCN-11	18	1.816
PCN-14	36	1.520
Cu-HKUST-1	48	2.584

Table 0.7 Usable gravimetric density (g CH_4/g MOF) of stored CH_4 as a function of operating scenario and maximum working pressure, P_{max}: 35, 65 and 100 bar. For each P_{max} the usable capacity under two operating scenarios are reported: (i) isothermal (298 K) pressure swing (PS) to 5 bar, and (ii) pressure + temperature swing (TPS) from P_{max} and 298 K to 5 bar and 358 K.

MOF	Usable CH_4 for P_{max} = 35 bar		Usable CH_4 for P_{max} = 65 bar		Usable CH_4 for P_{max} = 100 bar	
	298 K (PS)	358 K (TPS)	298 K (PS)	358 K (TPS)	298 K (PS)	358 K (TPS)
Be-DOBDC	0.10	0.15	0.12	0.17	0.14	0.18
Mg-DOBDC	0.10	0.14	0.12	0.16	0.13	0.17
Ca-DOBDC	0.10	0.13	0.13	0.16	0.14	0.17
Sr-DOBDC	0.07	0.09	0.09	0.11	0.10	0.12
Sc-DOBDC	0.06	0.09	0.07	0.10	0.08	0.11
Ti-DOBDC	0.09	0.11	0.11	0.14	0.12	0.15
V-DOBDC	0.08	0.11	0.10	0.13	0.11	0.14
Cr-DOBDC	0.07	0.10	0.09	0.12	0.10	0.13
Mn-DOBDC	0.08	0.10	0.10	0.13	0.12	0.14
Fe-DOBDC	0.08	0.10	0.10	0.12	0.11	0.14
Co-DOBDC	0.08	0.10	0.10	0.12	0.11	0.13
Ni-DOBDC	0.07	0.10	0.09	0.11	0.10	0.13
Cu-DOBDC	0.06	0.08	0.08	0.10	0.08	0.10
Zn-DOBDC	0.07	0.10	0.09	0.12	0.10	0.13
Mo-DOBDC	0.05	0.07	0.07	0.08	0.07	0.09
W-DOBDC	0.04	0.05	0.05	0.06	0.05	0.07
Sn-DOBDC	0.05	0.08	0.06	0.09	0.06	0.09
Pb-DOBDC	0.04	0.07	0.05	0.08	0.06	0.08
MOF-5	0.14	0.15	0.21	0.22	0.25	0.27
PCN-11	0.13	0.16	0.17	0.20	0.19	0.22
PCN-14	0.10	0.13	0.12	0.16	0.14	0.17
Cu-HKUST-1	0.10	0.13	0.14	0.16	0.16	0.18

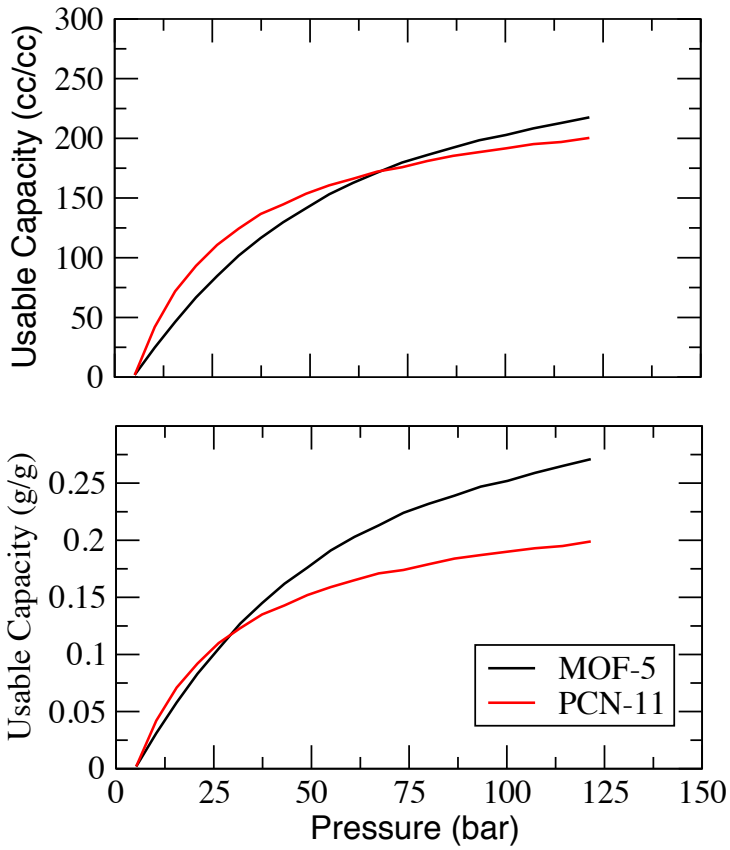

Figure 0.6 Usable volumetric (top panel) and gravimetric (bottom panel) CH_4 capacity in MOF-5 and PCN-11 as a function of maximum operating pressure, P_{max}.

Table 0.8 Summary of structural, thermodynamic, and volumetric CH_4 storage capacity of M-DOBDC. Data include: calculated cell volume ($Å^3$), pore volume ($Å^3$), surface area (m^2/g) for M-DOBDC, and isosteric heats of adsorption (Q_{st}) at 0.1 bar from GCMC (kJ/mol). Total CH_4 uptake capacities are given for three different pressures 0.1, 5, 35, and 100 bar at 298 K. The uptake capacities at 358 K and 5 bar are also given. Isosteric heats (Q_{st}) were calculated based on fluctuation theory within the grand canonical ensemble [D. Nicholson and N. Parsonage, "Computer Simulation and the Statistical Mechanics of Adsorption (1982)", Academic Press, London.]

$$Q_{st} = RT - \left(\frac{\partial U_N}{\partial N}\right)_{V,T} = RT - \frac{<NU_N> - <N><U_N>}{<N^2><N^2>}$$

Here, R and T are the universal gas constant and temperature, N is the number of adsorbed CH_4 molecules, and U_N is the potential energy of the adsorbed phase

M-DOBDC or MOF	Unit cell volume ($Å^3$)	Pore volume (cc/g)	Surface area (m^2/g)	-ΔH (vdW-DF2)	Q_{st} (GCMC)	Total volumetric CH_4 capacity (cc/cc)				
						0.1 bar	5 bar		35 bar	100 bar
							298 K	358 K		
M = Be	3793	0.721	2064	18.1	16.6	2.1	85.4	34.4	203.6	245.1
Mg	4097	0.681	1972	26.3	15.9	1.8	78.0	31.8	200.0	243.0
Ca	4690	0.711	1994	25.8	14.9	1.5	64.4	26.6	187.3	234.7
Sr	4779	0.520	1526	26.2	14.6	1.3	58.6	24.6	175.0	222.0
Sc	3615	0.459	1545	27.1	16.4	1.9	79.1	32.0	179.4	211.4
Ti	4213	0.585	1683	33.3	14.7	1.4	63.9	26.8	191.5	239.7
V	4080	0.549	1595	29.7	15.0	1.5	65.4	27.1	188.9	236.6
Cr	3976	0.509	1517	16.4	14.8	1.4	60.7	25.5	177.8	224.8
Mn	4297	0.563	1648	22.5	14.2	1.2	55.5	23.5	178.4	228.4
Fe	4143	0.540	1537	19.9	14.4	1.3	58.6	25.0	185.2	233.4
Co	4083	0.523	1531	26.0	14.9	1.4	63.9	26.5	188.3	234.2
Ni	3944	0.487	1454	25.3	15.2	1.5	67.5	27.9	189.4	234.4
Cu	3739	0.446	1310	22.3	14.8	1.4	60.0	25.2	170.5	211.7
Zn	4102	0.493	1489	25.4	15.8	1.7	75.0	30.4	196.2	240.5
Mo	3840	0.372	1126	26.4	15.1	1.4	59.0	24.7	173.6	215.0
W	3942	0.271	791	22.8	15.3	1.5	65.4	27.3	183.1	225.8
Sn	4296	0.353	1147	32.0	18.2	2.6	99.0	40.1	197.3	233.8
Pb	4972	0.314	1098	20.9	17.8	2.7	96.4	40.5	209.8	248.1
MOF-5	17778	1.336	3795		10.0	0.5	21.8	11.8	131.6	225
PCN-11	9911	0.985	3434		13.8	1.3	52.8	23.7	183.1	244
PCN-14	23692	0.799	2947		17.2	2.2	70.7	30.0	178.4	222
HKUST-1	18573	0.798	2742		15.7	2.5	53.9	26.7	178.4	241.9

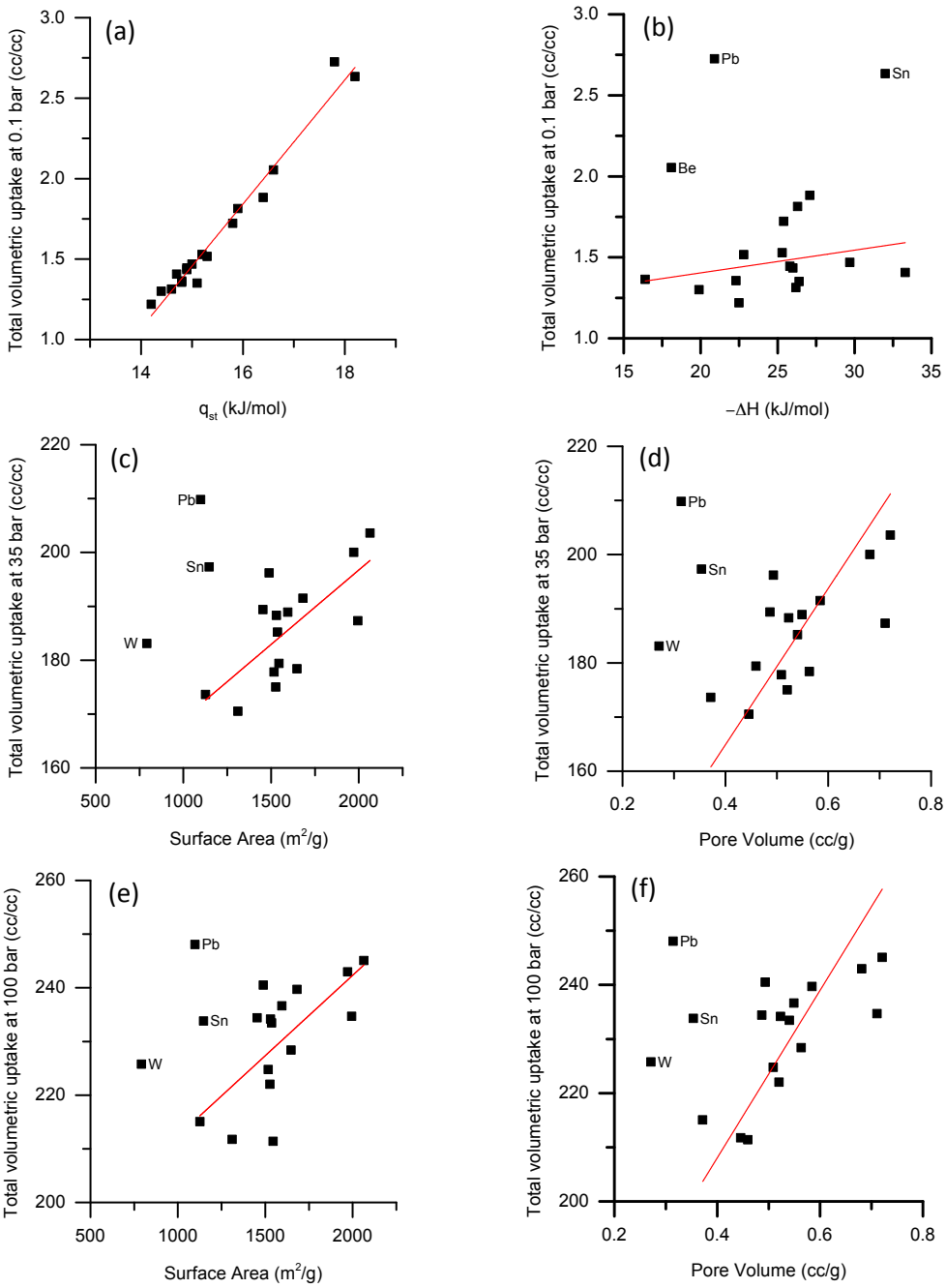

Figure 0.7 Relationship between total CH_4 uptake in the M-DOBDC series of MOFs at pressures of 0.1, 35, and 100 bar with various thermodynamic and structural properties. (a) uptake at 0.1 bar vs. heat of adsorption (Q_{st}) from GCMC calculations; (b) uptake at 0.1 bar vs. adsorption enthalpy (ΔH) from vdW-DF2 calculations, (c) uptake at 35 bar vs. surface area; (d) uptake at 35 bar vs. pore volume; (e) uptake at 100 bar vs. surface area; (f) uptake at 100 bar vs pore volume.

Table 0.9 Volumetric density of gaseous methane as a function of pressure (units of cm^3/cm^3). Total density is reported at 298 K, and usable density refers to either an isothermal pressure swing to a minimum pressure of 5 bar ("Usable – 298 K), or a pressure + temperature swing to 5 bar and 358 K ("Usable – 358 K").

35 bar			65 bar			100 bar			250 bar		
Total	Usable		Total	Usable		Total	Usable		Total	Usable	
	298 K	358 K		298 K	358 K		298 K	358 K		298 K	358 K
34	29	30	66	61	62	106	101	102	263	258	259

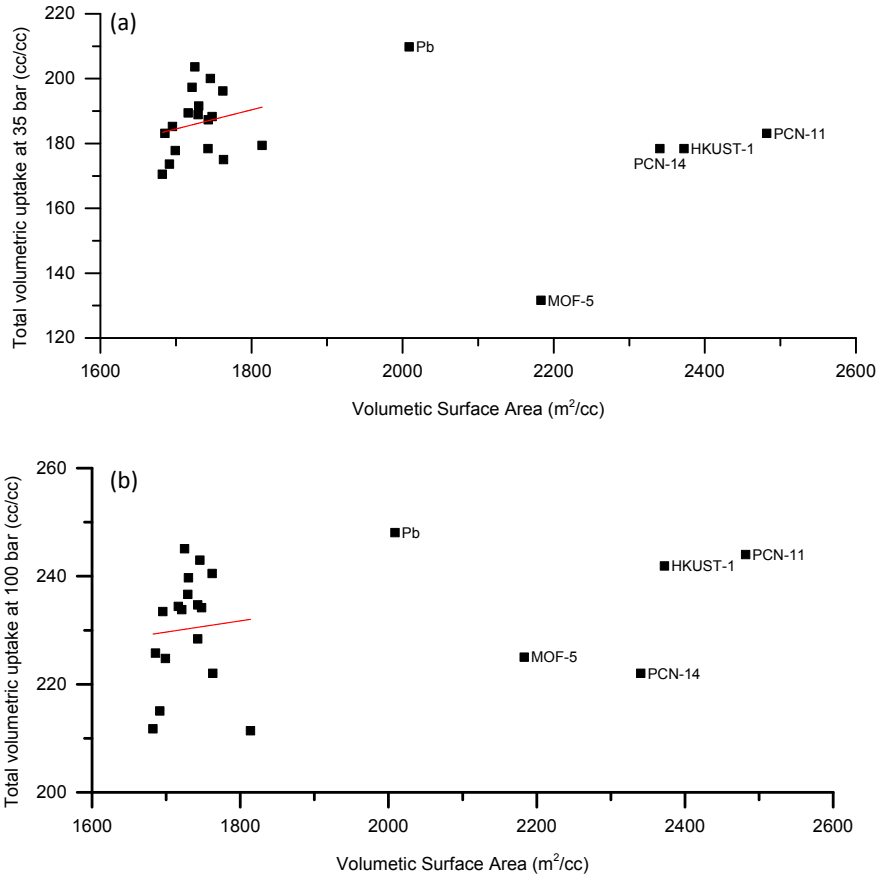

Figure 0.8 Relationship between total volumetric CH_4 uptake at (a) 35 bar and (b) 100 bar and MOF volumetric surface area.

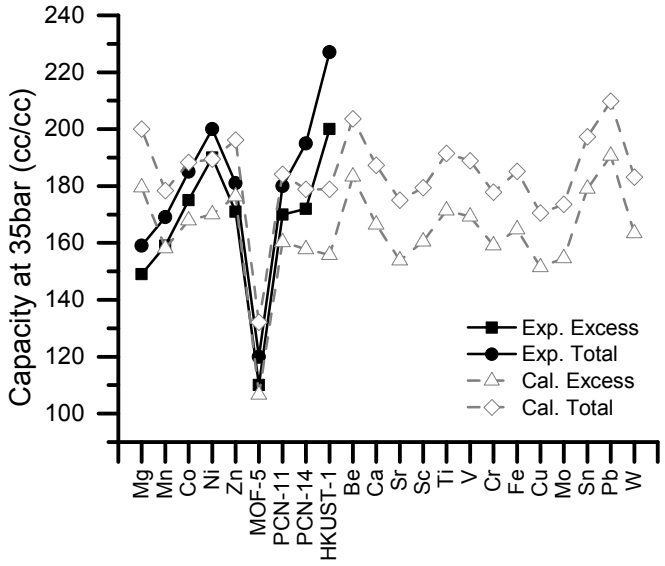

Figure 0.9 Calculated total CH_4 uptake at 35 bar and 298 K for M-DOBDC variants using the D-U+TarPPE force field. The corresponding experimental data[27,68,177,189] are represented using solid lines.

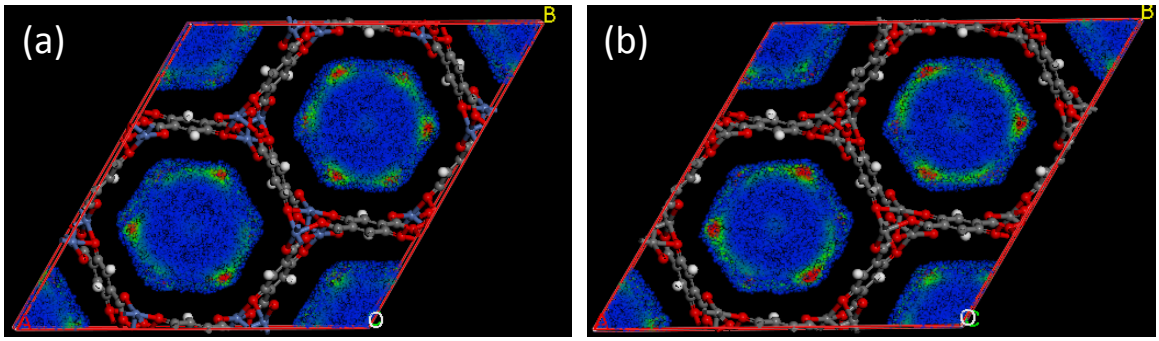

Figure 0.10 Methane density distributions at 30 bar and 298 K. (a) Ni-DOBDC, (b) a fictitious "C-DOBDC" system in which the Ni CUS has been substituted with C.

Appendix D. Supporting Information for CH_4 Adsorption and Applied on M-HKUST-1

Table 0.1 Methane binding energy (ΔE) at Cu CUS as a function of spin state

	Spin polarized	Non spin polarized
ΔE (kJ/mol)	15.6	15.8

Table 0.2 Force field parameters for Cu-HKUST-1 / CH_4 interactions. C-CH_4, H-CH_4, and O-CH_4 parameters correspond to a Lennard-Jones interaction after application of the Lorenz mixing rule. The parameters for MOF atoms are from the Universal Force Field,[128] and CH_4 parameters are from the single site TraPPE model.[129] Parameters for the Cu-CH_4 interaction apply to a Morse potential form, as described in the manuscript

	D_0 (kcal/mol)	R_0 (Å)	α
C-CH4	0.176	4.02	
H-CH4	0.114	3.51	
O-CH4	0.133	3.84	
Cu-CH4	1.190	3.15	1.72

Table 0.3 Tuned Metal – CH_4 force field parameters for the 18 M-HKUST-1 variants. The parameters apply to a Morse potential form.

	D_0 (kcal/mol)	R_0 (Å)	α
Be	1.883	2.63	1.677
Ca	2.662	3.07	1.769
Co	1.524	3.03	1.535
Cr	0.774	3.47	1.522
Cu	1.190	3.15	1.724
Fe	1.554	3.05	1.683
Mg	3.585	2.70	1.744
Mn	1.521	3.05	1.601
Mo	0.848	3.61	1.588
Ni	0.486	3.49	1.678
Pb	0.392	4.12	1.719
Sc	0.372	3.83	1.217
Sn	0.393	4.26	1.731
Sr	2.160	3.29	1.823
Ti	0.567	3.57	1.454
V	0.438	3.74	1.477
W	0.864	3.65	1.582
Zn	3.084	2.81	1.683

Table 0.4 Total and usable methane capacities at 100 bar, and isosteric heats (q_{st}) evaluated at 5 bar.

		100 bar					
		Total		Usable (5bar)			
	q_{st}	298 K		PS (298 K)		TPS (298 K)	
	kJ/mol	cc/cc	g/g	cc/cc	g/g	cc/cc	g/g
Be	17.9	280	0.28	183	0.18	212	0.21
Ca	19.4	312	0.32	197	0.20	231	0.24
Co	18.0	296	0.24	191	0.16	224	0.18
Cr	17.0	281	0.25	199	0.18	224	0.20
Cu	16.9	281	0.23	197	0.16	223	0.18
Fe	17.3	290	0.25	198	0.17	227	0.19
Mg	21.1	305	0.32	164	0.17	207	0.22
Mn	17.7	295	0.25	193	0.16	225	0.19
Mo	16.8	278	0.22	197	0.15	223	0.17
Ni	16.6	265	0.22	191	0.16	213	0.18
Pb	16.5	234	0.13	173	0.10	191	0.11
Sc	17.1	268	0.26	187	0.18	211	0.20
Sn	17.5	233	0.16	166	0.11	186	0.13
Sr	17.8	299	0.25	204	0.17	235	0.20
Ti	17.1	274	0.25	189	0.17	215	0.20
V	16.6	266	0.25	195	0.18	216	0.20
W	17.1	281	0.16	195	0.11	221	0.12
Zn	20.5	305	0.26	164	0.14	209	0.18

Table 0.5 Calculated adsorption energies (vdW-DF2 functional) for various adsorption sites in Cu-HKUST-1. The adsorption site names are the same as those used in Getzschmann *et al*.[63]

Site	ΔE (kJ/mol)
A	-23.2
B	-16.8
C (CUS site)	-13.8
D	-13.0
E	-25.5
F	-8.2
G	-18.0

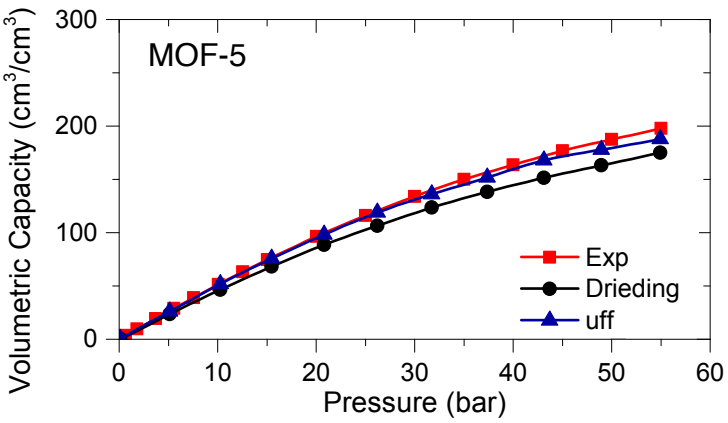

Figure 0.1 Comparison of the experimental CH_4 isotherms[200] in MOF-5 at 298 K (red curves) with isotherms calculated using either the Dreiding Force Field[127] (black curve) or the Universal Force Field[128] (blue curve).

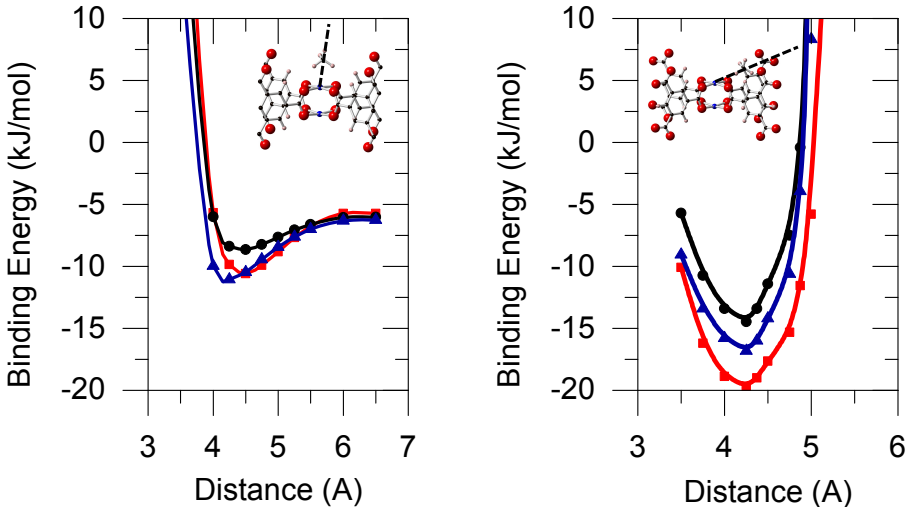

Figure 0.2 Comparison of binding energy (BE) curves obtained from the fitting of inter-atomic parameters for MOF—CH_4 interactions (blue) with the reference data from vdW-DF2 calculations (red) and a general potential based on the Universal Force Field (black.) The insets depict the paths used to obtain BE plots.

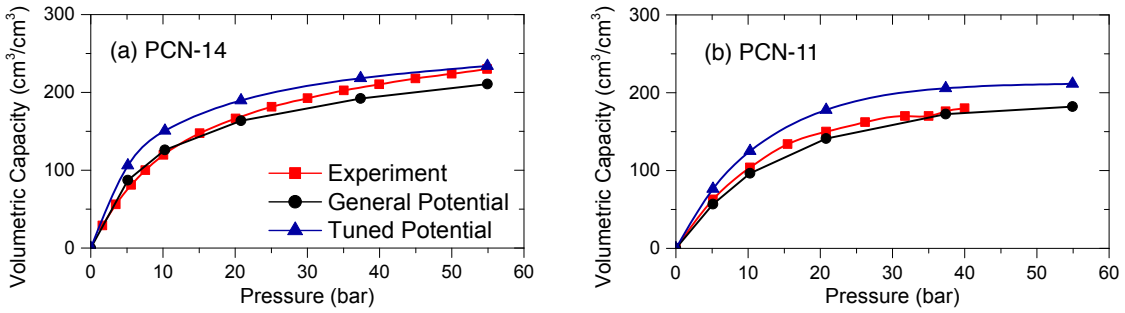

Figure 0.3 Comparison of calculated adsorption isotherms for PCN-14 and PCN-11 with experimental data[177,28] at 298K. The colors of the isotherms use the same convention as in Figure S2. The slight overestimate of the tuned potential's isotherm for PCN-11 relative to the measured isotherm is attributed to the use of data from an early experimental measurement dating to 2008.[177] As with HKUST-1 and PCN-14,[28] we anticipate that a reassessment of the isotherm for a carefully activated version of this system would result in higher uptake, bringing the computed and measured isotherms into even closer agreement.

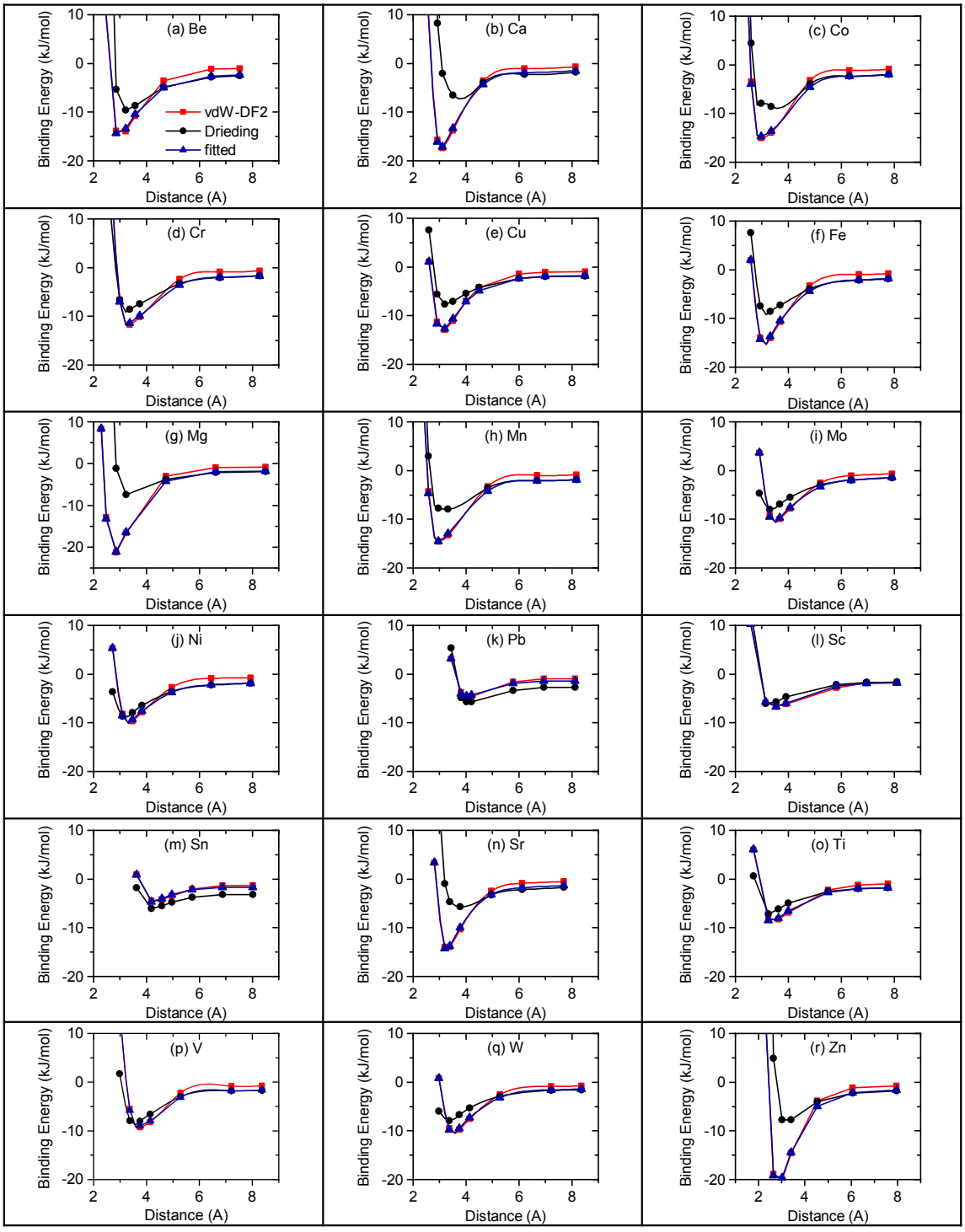

Figure 0.4 Binding energy curves for M-HKUST-1 systems obtained from first-principles calculations (vdW-DF2), a general potential based on Universial FF + TraPPE, and the tuned potentials.

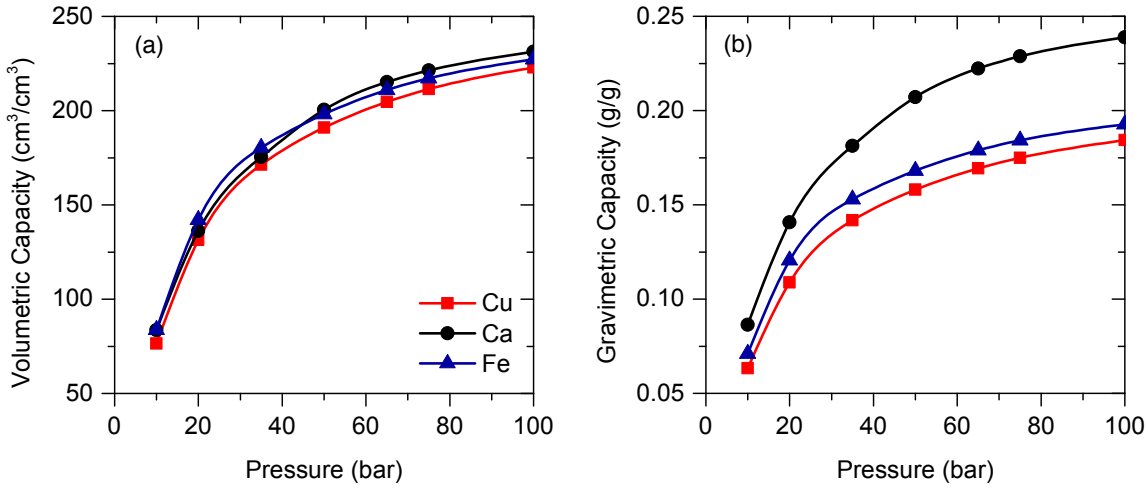

Figure 0.5 Volumetric and gravimetric usable methane capacity vs. pressure for Cu-HKUST-1 (red), Ca-HKUST-1 (black), and Fe-HKUST-1 (blue).

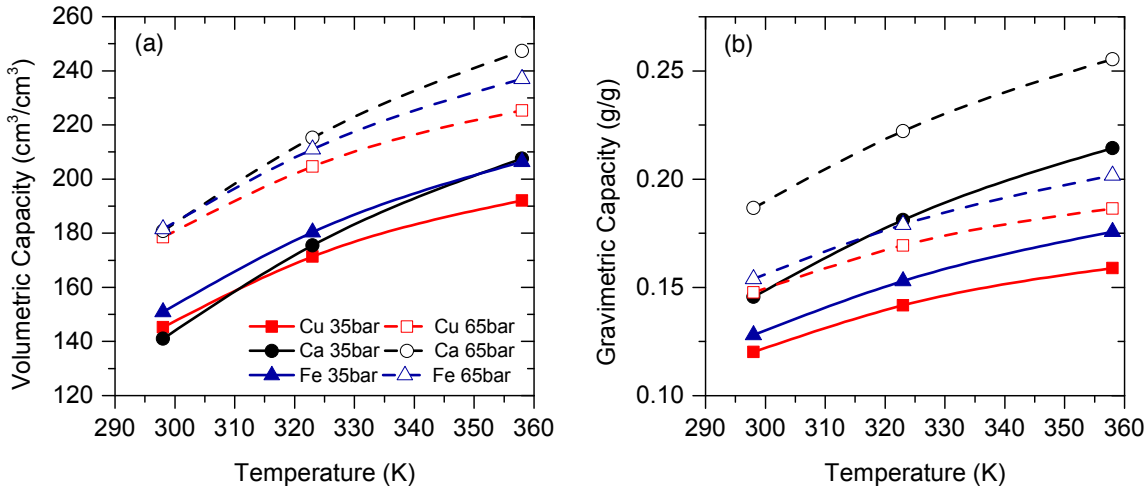

Figure 0.6 Volumetric and gravimetric usable methane capacity vs. desorption temperature at 35 bar (Solid lines, filled symbols), and 65 bar (dashed lines, open symbols). Red corresponds to Cu-HKUST-1; blue to Fe-HKUST-1; black to Ca-HKUST-1.

Bibliography

(1) Intergovernmental Panel on Climate Change. *Climate Change 2013: The Physical Sicience Basic*, 2013.

(2) Tans, P.;Keeling R. ESRL Global Monitoring Division, http://www.esrl.noaa.gov/gmd/ccgg/trends/ (accessed at Aug 26, 2014)

(3) Intergovernmental Panel on Climate Change. *Climate Change 2014: Impacts, Adaptation and Vulnerability*, 2014.

(4) Intergovernmental Panel on Climate Change. *Climate Change 2014: Mitigation of Climate Change*, 2014.

(5) U. S. Environmental Protection Agency. *Inventory of U.S. Green House Gas Emission and Sink: 1990-2012*, 2014.

(6) U.S Energy Information Administration. Annual Energy Outlook 2014. 2014.

(7) Figueroa, J. D.; Fout, T.; Plasynski, S.; McIlvried, H.; Srivastava, R. D. *Int. J. Greenhouse Gas Control* **2008**, *2*, 9.

(8) Aaron, D.; Tsouris, C. *Sep. Sci. Technol.* **2005**, *40*, 321.

(9) Freeman, B. *Assessment of Post-Combustion Carbon Capture Technology Developments*, 2007.

(10) Kim, I.; Svendsen, H. F. *Ind. Eng. Chem. Res.* **2007**, *46*, 5803.

(11) Yong, Z.; Mata, V.; Rodrigues, A. E. *Sep. Purif. Technol.* **2002**, *26*, 195.

(12) Klara, J. M. *Cost and Performance Baseline for Fossile Energy Plant*, National Energy Technology Laboratory, 2007.

(13) Versteeg, P.; Rubin, E. S. *International Journal of Greenhouse Gas Control* **2011**, *5*, 1596.

(14) Department of Energy. Carbon Capture R&D, http://energy.gov/fe/science-innovation/carbon-capture-and-storage-research/carbon-capture-rd (accessed Aug 26,2014).

(15) American Physical Society. *Direct Air Capture of CO2 with Chemicals*, 2011.

(16) Granite, E. J.; Pennline, H. W. *Industrial & Engineering Chemistry Research* **2002**, *41*, 5470.

(17)Kizzie, A. C.; Wong-Foy, A. G.; Matzger, A. J. *Langmuir* **2011**, *27*, 6368.

(18) Ding, L.; Yazaydin, A. Ö. *J. Phys. Chem. C* **2012**, *116*, 22987.

(19) U.S. Energy Information Administration. International Energy Statistics. http://www.eia.gov/cfapps/ipdbproject/IEDIndex3.cfm?tid=3&pid=26&aid=1 (accessed Aug 26, 2014)

(20) Foss, M. M. *Introduction to LNG: An overview on liquefied natural gas (LNG), its properties, organization of the LNG industry and safety considerations*, 2007.

(21) Celzard, A.; Fierro, V. *Energy & Fuels* **2005**, *19*, 573.

(22) Lozano-Castelló, D.; Alcañiz-Monge, J.; de la Casa-Lillo, M. A.; Cazorla-Amorós, D.; Linares-Solano, A. *Fuel* **2002**, *81*, 1777.

(23) Blazek, C. F. G., J.; Freman, P.; Bailey, B. K.;Colucci, C. *Prepr. Pap. - Am. Chem. Div. Fuel Chem.* **1994**, *39*, 476.

(24) Brandt, A. R.; Heath, G. A.; Kort, E. A.; O'Sullivan, F.; Pétron, G.; Jordaan, S. M.; Tans, P.; Wilcox, J.; Gopstein, A. M.; Arent, D.; Wofsy, S.; Brown, N. J.; Bradley, R.; Stucky, G. D.; Eardley, D.; Harriss, R. *Science* **2014**, *343*, 733.

(25) Lane, B. *Life Cycle Assessment of Vehicle Fuels and Technologies*, 2006.

(26) Menon, V. C.; Komarneni, S. *J. Porous Mater.* **1998**, *5*, 43.

(27) Peng, Y.; Krungleviciute, V.; Eryazici, I.; Hupp, J. T.; Farha, O. K.; Yildirim, T. *J. Am. Chem. Soc.* **2013**, *135*, 11887.

(28) Mason, J. A.; Veenstra, M.; Long, J. R. *Chem. Sci.* **2014**, *5*, 32.

(29) Yeh, S. *Energy Policy* **2007**, *35*, 5865.

(30) Whyatt, G. A. *Issues Affecting Adoption of Natural Gas Fuel in Light- and Heavy-Duty Vehicles*, 2010.

(31) National Renewable Energy Laboratory, *Cost of Adding E85 Fueling Capability to Exsiting Gasoline Stations*, 2008.

(32) Lemmon, E. W. H., M.L.;Mclinden,M.O. *NIST Standard Reference Database 23: Reference Fluid Thermodynamic and Transport Properties-REFPROP*; National Institute of Standards and Technology, 2007.

(33) Breck, D. W. *Zeolite Molecular Sieves*; J. Wiley & Sons: New York, 1974.

(34) Quinn, D. F. M., J. A.;Sosin, K. *Prepr. Pap. - Am. Chem. Div. Fuel Chem.* **1994**, *39*, 451.

(35) Wegrzyn, J.; Gurevich, M. *Applied Energy* **1996**, *55*, 71.

(36) Department of Energy. ARPA-E, https://arpa-e-foa.energy.gov/

(37) Burchell, T. D. *Carbon Materials for Advanced Technologies*; Pergamon, 1999.

(38) Matranga, K. R.; Myers, A. L.; Glandt, E. D. *Chem. Eng. Sci.* **1992**, *47*, 1569.

(39) Ferey, G. *Chem. Soc. Rev.* **2008**, *37*, 191.

(40) Rowsell, J. L. C.; Yaghi, O. M. *Microporous Mesoporous Mater.* **2004**, *73*, 3.

(41) Batten, S. R.; Neville, S. M.; Turner, D. R. *Coordination Polymers: Design, Synthesis, and Application*, 2009.

(42) Hong, M. C.; Chen, L. *Design and Construction of Coordination Polymers*, 2009.

(43) Long, J. R.; Yaghi, O. M. *Chem. Soc. Rev.* **2009**, *38*, 1213.

(44) Keskin, S.; van Heest, T. M.; Sholl, D. S. *ChemSusChem* **2010**, *3*, 879.

(45) Bae, Y.-S.; Snurr, R. Q. *Angew. Chem. Int. Ed.* **2011**, *50*, 11586.

(46) Makal, T. A.; Li, J.-R.; Lu, W.; Zhou, H.-C. *Chem. Soc. Rev.* **2012**, *41*, 7761.

(47) He, Y.; Zhou, W.; Qian, G.; Chen, B. *Chem. Soc. Rev.* **2014**, *43*, 5657.

(48) Yang, R. T. *Adsorbents: Fundamentals and Applications*, 2003.

(49) Choi, S. J.; Drese, H.; Jones, C. W. *ChemSusChem* **2009**, *2*, 796.

(50) Tranchemontagne, D. J.; Mendoza-Cortes, J. L.; O'Keeffe, M.; Yaghi, O. M. *Chem. Soc. Rev.* **2009**, *38*, 1257.

(51) Wilmer, C. E.; Leaf, M.; Lee, C. Y.; Farha, O. K.; Hauser, B. G.; Hupp, J. T.; Snurr, R. Q. *Nat Chem* **2012**, *4*, 83.

(52) Ma, S.; Zhou, H.-C. *Chem. Commun.* **2010**, *46*, 44.

(53) Park, T.-H.; Cychosz, K. A.; Wong-Foy, A. G.; Dailly, A.; Matzger, A. J. *Chem. Commun.* **2011**, *47*, 1452.

(54) Ockwig, N. W.; Delgado-Friedrichs, O.; O'Keeffe, M.; Yaghi, O. M. *Acc. Chem. Res.* **2005**, *38*, 176.

(55) Goldsmith, J.; Wong-Foy, A. G.; Cafarella, M. J.; Siegel, D. J. *Chem. Mater.* **2013**, *25*, 3373.

(56) Farha, O. K.; Eryazici, I.; Jeong, N. C.; Hauser, B. G.; Wilmer, C. E.; Sarjeant, A. A.; Snurr, R. Q.; Nguyen, S. T.; Yazaydın, A. Ö.; Hupp, J. T. *J. Am. Chem. Soc.* **2012**, *134*, 15016.

(57) Farha, O. K.; Özgür Yazaydın, A.; Eryazici, I.; Malliakas, C. D.; Hauser, B. G.; Kanatzidis, M. G.; Nguyen, S. T.; Snurr, R. Q.; Hupp, J. T. *Nat Chem* **2010**, *2*, 944.

(58) Koh, K.; Wong-Foy, A. G.; Matzger, A. J. *J. Am. Chem. Soc.* **2009**, *131*, 4184.

(59) Panella, B.; Hirscher, M.; Roth, S. *Carbon* **2005**, *43*, 2209.

(60) Caskey, S. R.; Wong-Foy, A. G.; Matzger, A. J. *J. Am. Chem. Soc.* **2008**, *130*, 10870.

(61) Wu, H.; Simmons, J. M.; Srinivas, G.; Zhou, W.; Yildirim, T. *J. Phys. Chem. Lett.* **2010**, *1*, 1946.

(62) Wu, H.; Simmons, J. M.; Liu, Y.; Brown, C. M.; Wang, X.-S.; Ma, S.; Peterson, V. K.; Southon, P. D.; Kepert, C. J.; Zhou, H.-C.; Yildirim, T.; Zhou, W. *Chemistry – A European Journal* **2010**, *16*, 5205.

(63) Getzschmann, J.; Senkovska, I.; Wallacher, D.; Tovar, M.; Fairen-Jimenez, D.; Düren, T.; van Baten, J. M.; Krishna, R.; Kaskel, S. *Microporous Mesoporous Mater.* **2010**, *136*, 50.

(64) Park, J.; Kim, H.; Han, S. S.; Jung, Y. *J. Phys. Chem. Lett.* **2012**, *3*, 826.

(65) Rosi, N. L.; Kim, J.; Eddaoudi, M.; Chen, B.; O'Keeffe, M.; Yaghi, O. M. *J. Am. Chem. Soc.* **2005**, *127*, 1504.

(66) Bloch, E. D.; Murray, L. J.; Queen, W. L.; Chavan, S.; Maximoff, S. N.; Bigi, J. P.; Krishna, R.; Peterson, V. K.; Grandjean, F.; Long, G. J.; Smit, B.; Bordiga, S.; Brown, C. M.; Long, J. R. *J. Am. Chem. Soc.* **2011**, *133*, 14814.

(67) Zhou, W.; Wu, H.; Yildirim, T. *J. Am. Chem. Soc.* **2008**, *130*, 15268.

(68) Wu, H.; Zhou, W.; Yildirim, T. *J. Am. Chem. Soc.* **2009**, *131*, 4995.

(69) Chui, S. S.-Y.; Lo, S. M.-F.; Charmant, J. P. H.; Orpen, A. G.; Williams, I. D. *Science* **1999**, *283*, 1148.

(70) Murray, L. J.; Dinca, M.; Yano, J.; Chavan, S.; Bordiga, S.; Brown, C. M.; Long, J. R. *J. Am. Chem. Soc.* **2010**, *132*, 7856.

(71) Maniam, P.; Stock, N. *Inorg. Chem.* **2011**, *50*, 5085.

(72) Feldblyum, J. I.; Liu, M.; Gidley, D. W.; Matzger, A. J. *J. Am. Chem. Soc.* **2011**, *133*, 18257.

(73) Kozachuk, O.; Yusenko, K.; Noei, H.; Wang, Y.; Walleck, S.; Glaser, T.; Fischer, R. A. *Chem. Commun.* **2011**, *47*, 8509.

(74) Kramer, M.; Schwarz, U.; Kaskel, S. *J. Mater. Chem.* **2006**, *16*, 2245.

(75) Wade, C. R.; Dinca, M. *Dalton Transactions* **2012**, *41*, 7931.

(76) Curtarolo, S.; Hart, G. L. W.; Nardelli, M. B.; Mingo, N.; Sanvito, S.; Levy, O. *Nat Mater* **2013**, *12*, 191.

(77) Lin, L.-C.; Berger, A. H.; Martin, R. L.; Kim, J.; Swisher, J. A.; Jariwala, K.; Rycroft, C. H.; Bhown, A. S.; Deem, M. W.; Haranczyk, M.; Smit, B. *Nat Mater* **2012**, *11*, 633.

(78) Haldoupis, E.; Nair, S.; Sholl, D. S. *J. Am. Chem. Soc.* **2010**, *132*, 7528.

(79) Watanabe, T.; Sholl, D. S. *Langmuir* **2012**, *28*, 14114.

(80) Martin, R. L.; Simon, C. M.; Smit, B.; Haranczyk, M. *J. Am. Chem. Soc.* **2014**, *136*, 5006.

(81) Canepa, P.; Arter, C. A.; Conwill, E. M.; Johnson, D. H.; Shoemaker, B. A.; Soliman, K. Z.; Thonhauser, T. *J. Mater. Chem. A* **2013**, *1*, 13597.

(82) Greeley, J.; Jaramillo, T. F.; Bonde, J.; Chorkendorff, I.; Norskov, J. K. *Nat Mater* **2006**, *5*, 909.

(83) Studt, F.; Abild-Pedersen, F.; Bligaard, T.; Sørensen, R. Z.; Christensen, C. H.; Nørskov, J. K. *Science* **2008**, *320*, 1320.

(84) Yu, L.; Zunger, A. *Phys. Rev. Lett.* **2012**, *108*, 068701.

(85) Allen, F. H. *Acta Crystallogr. Sect. B: Struct. Sci.* **2002**, *58*, 380.

(86) Hohenberg, P.; Kohn, W. *Physical Review* **1964**, *136*, B864.

(87) Kohn, W.; Sham, L. J. *Physical Review* **1965**, *140*, A1133.

(88) Born, M.; Oppenheimer, R. *Annalen der Physik* **1927**, *389*, 457.

(89) Perdew, J. P.; Burke, K.; Ernzerhof, M. *Phys. Rev. Lett.* **1996**, *77*, 3865.

(90) Sun, Y. Y.; Kim, Y.-H.; Lee, K.; Zhang, S. B. *J. Chem. Phys.* **2008**, *129*, 154102.

(91) Chakarova-Käck, S. D.; Schröder, E.; Lundqvist, B. I.; Langreth, D. C. *Phys. Rev. Lett.* **2006**, *96*, 146107.

(92) Jeziorski, B.; Moszynski, R.; Szalewicz, K. *Chem. Rev.* **1994**, *94*, 1887.

(93) Heelmann, A.; Jansen, G. *Phys. Chem. Chem. Phys.* **2003**, *5*, 5010.

(94) Misquitta, A. J.; Jeziorski, B.; Szalewicz, K. *Phys. Rev. Lett.* **2003**, *91*, 033201.

(95) Osinga, V. P.; van Gisbergen, S. J. A.; Snijders, J. G.; Baerends, E. J. *J. Chem. Phys.* **1997**, *106*, 5091.

(96) Tkatchenko, A.; DiStasio, R. A.; Car, R.; Scheffler, M. *Phys. Rev. Lett.* **2012**, *108*, 236402.

(97) Tkatchenko, A.; Schefer, M. *Phys. Rev. Lett.* **2009**, *102*, 073005.

(98) Bludský, O.; Rubens, M.; Soldán, P.; Nachtigall, P. *J. Chem. Phys.* **2008**, *128*, 114102.

(99) Grimme, S. *J. Comput. Chem.* **2004**, *25*, 1463.

(100) Grimme, S. *J. Comput. Chem.* **2006**, *27*, 1787.

(101) Grimme, S.; Antony, J.; Ehrlich, S.; Krieg, H. *J. Chem. Phys.* **2010**, *132*, 154104.

(102) Dion, M.; Rydberg, H.; Schröder, E.; Langreth, D. C.; Lundqvist, B. I. *Phys. Rev. Lett.* **2004**, *92*, 246401.

(103) Bučko, T.; Hafner, J.; Lebègue, S.; Ángyán, J. G. *J. Phys. Chem. A* **2010**, *114*, 11814.

(104) Atodiresei, N.; Caciuc, V.; Franke, J. H.; Blügel, S. *Phys. Rev. B* **2008**, *78*, 045411.

(105) Kerber, T.; Sierka, M.; Sauer, J. *J. Comput. Chem.* **2008**, *29*, 2088.

(106) Román-Pérez, G.; Soler, J. M. *Phys. Rev. Lett.* **2009**, *103*, 096102.

(107) Jennes, G. R.; Karalti, O.; Al-Saiadi, W. A.; Jordan, K. D. *J. Phys. Chem. A* **2011**, *115*, 5955.

(108) Adamo, C.; Barone, V. *J. Chem. Phys.* **1999**, *110*, 6158.

(109) Bohm, D.; Pines, D. *Phys. Rev.* **1953**, *92*, 609.

(110) Klimeš, J.; Bowler, D. R.; Michaelides, A. *Phys. Rev. B* **2011**, *83*, 195131.

(111) Klimeš, J.; David, R. B.; Angelos, M. *J. Phys.: Condens. Matter* **2010**, *22*, 022201.

(112) Lee, K.; Murray, É. D.; Kong, L.; Lundqvist, B. I.; Langreth, D. C. *Phys. Rev. B* **2010**, *82*, 081101.

(113) Kresse, G.; Furthmüller, J. *Phys. Rev. B* **1996**, *54*, 11169.

(114) Blöchl, P. E. *Phys. Rev. B* **1994**, *50*, 17953.

(115) Murray, C. W.; Racine, S. C.; Davidson, E. R. *Journal of Computational Physics* **1992**, *103*, 382.

(116) Pulay, P. *Chem. Phys. Lett.* **1980**, *73*, 393.

(117) Monkhorst, H. J.; Pack, J. D. *Phys. Rev. B* **1976**, *13*, 5188.

(118) Press, W. H. T., S.A.;Vetterling,W.R;Flannery,B.P *Numerical Recipes in Fortran 90: The Art of parallel Scientific Computing*; 2nd ed.; Cambridge University Press, 1996.

(119) Wallace, D. C. *Thermodynamics of Crystals*, 1972.

(120) Rickman, J. M.; LeSar, R. *Annu. Rev. Mater. Res.* **2002**, *32*, 195.

(121) Wei, S.; Chou, M. Y. *Phys. Rev. Lett.* **1992**, *69*, 2799.

(122) Voter, A. In *Radiation Effects in Solids*; Sickafus, K., Kotomin, E., Uberuaga, B., Eds.; Springer Netherlands: 2007; Vol. 235, p 1.

(123) Frenkel, D.; Smit, B. *Understanding Molecular Simulation*; Academic Press, Inc., 2001.

(124) Dubbeldam, D.; Torres-Knoop, A.; Walton, K. S. *Mol. Simul.* **2013**, *39*, 1253.

(125) Metropolis, N.; Rosenbluth, A. W.; Rosenbluth, M. N.; Teller, A. H.; Teller, E. *J. Chem. Phys.* **1953**, *21*, 1087.

(126) Nicholson, D.; Parsonage, N. G. *Computer simulation and the statistical mechanics of adsorption*; Academic Press, 1982.

(127) Mayo, S. L.; Olafson, B. D.; Goddard, W. A. *J. Phys. Chem.* **1990**, *94*, 8897.

(128) Rappe, A. K.; Casewit, C. J.; Colwell, K. S.; Goddard, W. A.; Skiff, W. M. *J. Am. Chem. Soc.* **1992**, *114*, 10024.

(129) Martin, M. G.; Siepmann, J. I. *J. Phys. Chem. B* **1998**, *102*, 2569.

(130) Akkermans, R. L. C.; Spenley, N. A.; Robertson, S. H. *Mol. Simul.* **2013**, 1.

(131) Spek, A. *J. Appl. Crystallogr.* **2003**, *36*, 7.

(132) Wu, X.; Vargas, M. C.; Nayak, S.; Lotrich, V.; Scoles, G. *J. Chem. Phys.* **2001**, *115*, 8748.

(133) Wu, Q.; Yang, W. *J. Chem. Phys.* **2002**, *116*, 515.

(134) Sun, X.; Yamauchi, Y. *J. Appl. Phys.* **2011**, *110*, 103701.

(135) Cooper, V. R.; Kong, L.; Langreth, D. C. *Phys. Procedia* **2010**, *3*, 1417.

(136) Ziambaras, E.; Kleis, J.; Schröder, E.; Hyldgaard, P. *Phys. Rev. B* **2007**, *76*, 155425.

(137) Grimme, S.; Mück-Lichtenfeld, C.; Antony, J. *J. Phys. Chem. C* **2007**, *111*, 11199.

(138) Jurečka, P.; Šponer, J.; Černý, J.; Hobza, P. *Phys. Chem. Chem. Phys.* **2006**, *8*, 1985.

(139) Valenzano, L.; Civalleri, B.; Sillar, K.; Sauer, J. *J. Phys. Chem. C* **2011**, *115*, 21777.

(140) Puzder, A.; Dion, M.; Langreth, D. C. *J. Chem. Phys.* **2006**, *124*, 164105.

(141) Li, S.; Cooper, V. R.; Thonhauser, T.; Puzder, A.; Langreth, D. C. *J. Phys. Chem. A* **2008**, *112*, 9031.

(142) Cooper, V. R.; Thonhauser, T.; Puzder, A.; Schröder, E.; Lundqvist, B. I.; Langreth, D. C. *J. Am. Chem. Soc.* **2008**, *130*, 1304.

(143) Cooper, V. R.; Thonhauserb, T.; Langreth, D. C. *J. Chem. Phys.* **2008**, *128*, 204102.

(144) Londero, E.; Schröder, E. *Physical Review B* **2010**, *82*, 054116.

(145) Lee, K.; Kelkkanen, A. K.; Berland, K.; Andersson, S.; Langreth, D. C.; Schröder, E.; Lundqvist, B. I.; Hyldgaard, P. *Physical Review B* **2011**, *84*, 193408.

(146) Kong, L.; Cooper, V. R.; Nijem, N.; Li, K.; Li, J.; Chabal, Y. J.; Langreth, D. C. *Phys. Rev. B* **2009**, *79*, 081407.

(147) Dietzel, P. D. C.; Panella, B.; Hirscher, M.; Blom, R.; Fjellvag, H. *Chem. Commun.* **2006**, 959.

(148) Dietzel, P. D. C.; Morita, Y.; Blom, R.; Fjellvåg, H. *Angew. Chem. Int. Ed.* **2005**, *44*, 6354.

(149) Dietzel, P. D. C.; Blom, R.; Fjellvag, H. *Eur. J. Inorg. Chem.* **2008**, 3624.

(150) Valenzano, L.; Civalleri, B.; Chavan, S.; Palomino, G. T.; Areán, C. O.; Bordiga, S. *J. Phys. Chem. C* **2010**, *114*, 11185.

(151) Britt, D.; Furukawa, H.; Wang, B.; Glover, T. G.; Yaghi, O. M. *Proceedings of the National Academy of Sciences* **2009**, *106*, 20637.

(152) Dietzel, P. D. C.; Besikiotis, V.; Blom, R. *J. Mater. Chem.* **2009**, *19*, 7362.

(153) Bao, Z.; Yu, L.; Ren, Q.; Lu, X.; Deng, S. *J. Colloid Interface Sci.* **2011**, *353*, 549.

(154) Liu, J., Vanderbilt University, 2011.

(155) Dietzel, P. D. C.; Johnsen, R. E.; Fjellvag, H.; Bordiga, S.; Groppo, E.; Chavan, S.; Blom, R. *Chem. Commun.* **2008**, 5125.

(156) Wang, Q. M.; Shen, D.; Bülow, M.; Lau, M. L.; Deng, S.; Fitch, F. R.; Lemcof, N. O.; Semanscin, J. *Microporous Mesoporous Mater.* **2002**, *55*, 217.

(157) Liang, Z.; Marshall, M.; Chaffee, A. L. *Energy & Fuels* **2009**, *23*, 2785.

(158) Farrusseng, D.; Daniel, C. c.; Gaudillère, C.; Ravon, U.; Schuurman, Y.; Mirodatos, C.; Dubbeldam, D.; Frost, H.; Snurr, R. Q. *Langmuir* **2009**, *25*, 7383.

(159) Poloni, R.; Smit, B.; Neaton, J. B. *J. Phys. Chem. A* **2012**, *116*, 4957.

(160) Vosko, S. H.; Wilk, L.; Nusair, M. *Can. J. Phys.* **1980**, *58*, 1200.

(161) Hertzberg, G. *Infrared and Raman Spectra*, 1945.

(162) Queen, W. L.; Brown, C. M.; Britt, D. K.; Zajdel, P.; Hudson, M. R.; Yaghi, O. M. *J. Phys. Chem. C* **2011**, *115*, 24915.

(163) Aprea, P.; Caputo, D.; Gargiulo, N.; Iucolano, F.; Pepe, F. *J. Chem. Eng. Data* **2010**, *55*, 3655.

(164) Moellmer, J.; Moeller, A.; Dreisbach, F.; Glaeser, R.; Staudt, R. *Microporous Mesoporous Mater.* **2011**, *138*, 140.

(165) Grajciar, L.; Wiersum, A. D.; Llewellyn, P. L.; Chang, J. S.; Nachtigall, P. *J. Phys. Chem. C* **2011**, *115*, 17925.

(166) Byrd, E. F. C.; Scuseria, G. E.; Chabalowski, C. F. *J. Phys. Chem. B* **2004**, *108*, 13100.

(167) Byrd, E. F. C.; Rice, B. M. *J. Phys. Chem. C* **2007**, *111*, 2787.

(168) Qiu, L.; Xiao, H. M.; Zhu, W. H.; Xiao, J. J.; Zhu, W. *J. Phys. Chem. B* **2006**, *110*, 10651.

(169) Conroy, M. W.; Oleynik, I. I.; Zybin, S. V.; White, C. T. *Phys. Rev. B* **2008**, *77*, 094107.

(170) Zhang, X. X.; Chui, S. S. Y.; Williams, I. D. *J. Appl. Phys.* **2000**, *87*, 6007.

(171) Campañá, C.; Mussard, B.; Woo, T. K. *J. Chem. Theo. Compu.* **2009**, *5*, 2866.

(172) Simmons, J. M.; Wu, H.; Zhou, W.; Yildirim, T. *Energy & Environmental Science* **2011**, *4*, 2177.

(173) Min Wang, Q.; Shen, D.; Bülow, M.; Ling Lau, M.; Deng, S.; Fitch, F. R.; Lemcoff, N. O.; Semanscin, J. *Microporous Mesoporous Mater.* **2002**, *55*, 217.

(174) Rana, M. K.; Koh, H. S.; Hwang, J.; Siegel, D. J. *J. Phys. Chem. C* **2012**, *116*, 16957.

(175) Fernandez, M.; Woo, T. K.; Wilmer, C. E.; Snurr, R. Q. *J. Phys. Chem. C* **2013**, *117*, 7681.

(176) He, Y.; Zhou, W.; Yildirim, T.; Chen, B. *Energy & Environmental Science* **2013**.

(177) Wang, X.-S.; Ma, S.; Rauch, K.; Simmons, J. M.; Yuan, D.; Wang, X.; Yildirim, T.; Cole, W. C.; López, J. J.; Meijere, A. d.; Zhou, H.-C. *Chem. Mater.* **2008**, *20*, 3145.

(178) Ma, S.; Sun, D.; Simmons, J. M.; Collier, C. D.; Yuan, D.; Zhou, H.-C. *J. Am. Chem. Soc.* **2007**, *130*, 1012.

(179) Chen, L.; Morrison, C. A.; Düren, T. *J. Phys. Chem. C* **2012**, *116*, 18899.

(180) Zhou, W. *The Chemical Record* **2010**, *10*, 200.

(181) Yang, Q.; Zhong, C. *J. Phys. Chem. B* **2006**, *110*, 17776.

(182) Chen, L.; Grajciar, L.; Nachtigall, P.; Düren, T. *J. Phys. Chem. C* **2011**, *115*, 23074.

(183) Koh, H. S.; Rana, M. K.; Hwang, J.; Siegel, D. J. *PCCP* **2013**, *15*, 4573.

(184) Perdew, J. P.; Burke, K.; Ernzerhof, M. *Phys. Rev. Lett.* **1996**, *77*, 3865.

(185) Karra, J. R.; Walton, K. S. *Langmuir* **2008**, *24*, 8620.

(186) Chen, B.; Siepmann, J. I. *J. Phys. Chem. B* **1999**, *103*, 5370.

(187) Sun, Y.; Spellmeyer, D.; Pearlman, D. A.; Kollman, P. *J. Am. Chem. Soc.* **1992**, *114*, 6798.

(188) Lucena, S. M. P.; Frutuoso, L. F. A.; Silvino, P. F. G.; Azevedo, D. C. S.; Toso, J. P.; Zgrablich, G.; Cavalcante Jr, C. L. *Colloids and Surfaces A: Physicochemical and Engineering Aspects* **2010**, *357*, 53.

(189) Zhou, W.; Wu, H.; Hartman, M. R.; Yildirim, T. *J. Phys. Chem. C* **2007**, *111*, 16131.

(190) Gupta, A.; Chempath, S.; Sanborn, M. J.; Clark, L. A.; Snurr, R. Q. *Mol. Simul.* **2003**, *29*, 29.

(191) Sillar, K.; Sauer, J. *J. Am. Chem. Soc.* **2012**, *134*, 18354.

(192) Bloch, E. D.; Queen, W. L.; Krishna, R.; Zadrozny, J. M.; Brown, C. M.; Long, J. R. *Science* **2012**, *335*, 1606.

(193) Wang, S. *Energy & Fuels* **2007**, *21*, 953.

(194) Lucena, S. M. P.; Mileo, P. G. M.; Silvino, P. F. G.; Cavalcante, C. L. *J. Am. Chem. Soc.* **2011**, *133*, 19282.

(195) Senkovska, I.; Kaskel, S. *Microporous Mesoporous Mater.* **2008**, *112*, 108.

(196) Frost, H.; Düren, T.; Snurr, R. Q. *J. Phys. Chem. B* **2006**, *110*, 9565.

(197) Rouquerol, F.; Rouquerol, J.; Sing, K. In *Adsorption by Powders and Porous Solids*; Academic Press: London, 1999, p 1.

(198) Ma, L.; Jin, A.; Xie, Z.; Lin, W. *Angew. Chem. Int. Ed.* **2009**, *48*, 9905.

(199) Fang, H.; Demir, H.; Kamakoti, P.; Sholl, D. S. *J. Mater. Chem. A* **2014**, *2*, 274.

(200) Dubbeldam, D.; Walton, K. S.; Ellis, D. E.; Snurr, R. Q. *Angew. Chem. Int. Ed.* **2007**, *46*, 4496.

(201) Rana, M. K.; Koh, H. S.; Zuberi, H.; Siegel, D. J. *J. Phys. Chem. C* **2014**, *118*, 2929.

(202) Dzubak, A. L.; Lin, L.-C.; Kim, J.; Swisher, J. A.; Poloni, R.; Maximoff, S. N.; Smit, B.; Gagliardi, L. *Nat Chem* **2012**, *4*, 810.

(203) Lin, L.-C.; Lee, K.; Gagliardi, L.; Neaton, J. B.; Smit, B. *J. Chem. Theo. Compu.* **2014**, *10*, 1477.

(204) Borycz, J.; Lin, L.-C.; Bloch, E. D.; Kim, J.; Dzubak, A. L.; Maurice, R.; Semrouni, D.; Lee, K.; Smit, B.; Gagliardi, L. *J. Phys. Chem. C* **2014**, *118*, 12230.

(205) Gale, J. D.; Rohl, A. L. *Mol. Simul.* **2003**, *29*, 291.

(206) Purewal, J.; Liu, D.; Sudik, A.; Veenstra, M.; Yang, J.; Maurer, S.; Müller, U.; Siegel, D. J. *J. Phys. Chem. C* **2012**, *116*, 20199.

(207) Purewal, J. J.; Liu, D.; Yang, J.; Sudik, A.; Siegel, D. J.; Maurer, S.; Müller, U. *Int. J. Hydrogen Energy* **2012**, *37*, 2723.

(208) Xie, L.; Liu, S.; Gao, C.; Cao, R.; Cao, J.; Sun, C.; Su, Z. *Inorg. Chem.* **2007**, *46*, 7782.

(209) Liu, B.; Wong-Foy, A. G.; Matzger, A. J. *Chem. Commun.* **2013**, *49*, 1419.

(210) Shannon, R. D. *Acta Crystallogr. Sect. A: Found. Crystallogr.* **1976**, *32*, 751.

(211) Pauling, L. *The Nature of the Chemical Bond: An Introduction to Modern Structural Chemistry*; Cornell Univ, 1960.

(212) Ahrens, L. H. *Geochim. Cosmochim. Acta* **1952**, *2*, 155.